DISSERTATION

TUNING THE INTERACTION OF DROPLETS WITH LIQUID-REPELLENT SURFACES:

FUNDAMENTALS AND APPLICATIONS

Submitted by

Sanli Movafaghi

Department of Mechanical Engineering

In partial fulfillment of the requirements

For the Degree of Doctor of Philosophy

Colorado State University

Fort Collins, Colorado

Fall 2018

Doctoral Committee:

Advisor: Arun K. Kota

Susan P. James
Charles S. Henry
Ketul C. Popat

ABSTRACT

TUNING THE INTERACTION OF DROPLETS WITH LIQUID-REPELLENT

SURFACES: FUNDAMENTALS AND APPLICATIONS

Liquid-repellent surfaces can be broadly classified as non-textured surfaces (e.g., smooth slippery surfaces on which droplets can slide easily) and textured surfaces (e.g., super-repellent surfaces on which liquid droplets can bead up and roll off easily). The liquid repellency of smooth slippery surfaces can be adjusted by tuning the surface chemistry. The liquid repellency of super-repellent surfaces can be adjusted by tuning the surface chemistry and surface texture. In this work, by systematically tuning the surface chemistry and surface texture and consequently the surface wettability of solid surfaces, the interaction of droplets of various liquids on liquid-repellent surfaces has been investigated. Based on this understanding, the following phenomena/applications have been investigated/developed:

(i) *New methodology to sort liquid droplets based on their surface tension:* By tuning the surface chemistry and surface texture of solid surfaces, we tuned the mobility of liquids with different surface tension on super-repellent surfaces. Utilizing this, we fabricated a simple device with precisely tailored domains of surface chemistry that can sort droplets by surface tension.

(ii) *New approach to detect the quality of fuel blends:* By tuning the surface chemistry of solid surfaces, we investigated the interaction of fuel blends with liquid-repellent surfaces. Based on the understanding gained, we fabricated a simple, field-

deployable, low-cost device to rapidly detect the quality of fuel blends by sensing their surface tension with significantly improved resolution.

(iii)   *Novel materials with improved hemocompatibility:* By systematically tuning the surface chemistry and surface texture and consequently the surface wettability of solid surfaces, we investigated the interaction of blood with super-repellent surfaces. Based on the understanding gained, we fabricated super-repellent surfaces with enhanced hemocompatibility.

(iv)   *Advanced understanding of droplet splitting upon impacting a macroscopic ridge:* By systematically tuning the ridge geometry, we investigated the interaction of impacting water droplets with super-repellent ridges. Based on the understanding gained, we demonstrated the scaling law for predicting the height from which water droplets should fall under gravity onto a super-repellent ridge for them to split into two smaller droplets.

ACKNOWLEDGEMENTS

It is a great pleasure to convey my gratitude to many people that without their participation and assistance the completion of this dissertation could not have been possible.

The foremost among those people is my supervisor, Dr. Arun K. Kota and I would like to express my sincere appreciation to him for his unwavering support, helpful and insightful criticism and understanding spirit throughout my PhD program. With his determined, experienced and enthusiastic nature, he has been a mentor for me both academically and non-academically.

I would also like to thank my outstanding committee members, Dr. Susan P. James, Dr. Charles S. Henry and Dr. Ketul C. Popat, for their encouragement, support and constructive comments.

I extend a warm thanks to my colleagues at our research group for their company, assistance, and friendship. I would like to thank all my teachers and professors for inspiring me to love learning.

Last in order but not of importance, I would like to deliver my love to my beloved husband and family for their patience, support and encouragement.

DEDICATION

To my beloved husband, Saman,

and

My sweet and loving mother, father, and sisters

For their unconditional love, wholehearted support, and day to day encouragement

TABLE OF CONTENTS

LIST OF TABLES

CHAPTER 1 – OVERVIEW

In recent years, extensive efforts have been devoted to the investigation of liquid-repellent surfaces, i.e., surfaces that display repellency to liquids. Liquid-repellent surfaces can be broadly classified as non-textured surfaces (e.g., smooth slippery surfaces on which droplets can slide easily) and textured surfaces (e.g., super-repellent surfaces on which liquid droplets can roll off easily). Smooth slippery surfaces with a homogeneous, non-polar surface chemistry with low surface energy typically provide high degree of mobility for liquid droplets. On the other hand, the extreme repellency of super-repellent surfaces arises from the combination of appropriate surface texture with a surface chemistry with low surface energy. In fact, the surface chemistry and surface texture are the two important governing parameters of surface wettability and the mobility of droplets on surfaces. Therefore, controlling the surface chemistry and surface texture leads to tunable surface wettability, resulting in tunable interaction between the surface and the contacting liquid droplets.

In this dissertation, the fundamental chemical and physical principles of designing liquid-repellent surfaces (with the emphasis on super-repellent surfaces) will be reviewed in chapter two. In addition, recent studies on super-repellent surfaces with tunable wettability and the motivation behind these studies will also be discussed. In chapter three, the systematic design of superomniphobic surfaces with tunable wettability to sort droplets by their surface tension will be presented. Subsequently, in chapter four, using the methodology of sorting droplets by surface tension described in chapter three, the systematic design of non-textured surfaces to quantify the fuel adulteration will be presented. Then, in chapter five, the interaction between blood droplets and super-repellent surfaces, as well as the design criteria for fabrication of hemocompatible

1

surfaces will be discussed. In chapter six, a systematic study of droplet splitting dynamics on super-repellent surfaces with a macroscopic ridge will be presented. Finally, in chapter seven, the contributions of this work to fundamental science and applied science will be summarized and the potential aspects of this work for future investigation will be presented.

So far, the following peer-reviewed journal publications have resulted from my PhD work at Colorado State University (in reverse chronological order):

- K. Bartlet, **S. Movafaghi**, L. P. Dasi, A. K. Kota, K. C. Popat " Antibacterial activity on superhydrophobic titania nanotube arrays," **Colloids and Surfaces B: Biointerfaces**, 166, p. 179 (2018).

- A. Pendurthi,* **S. Movafaghi**,* W. Wang, S. Shadman, A. P. Yalin, A. K. Kota "Fabrication of nanostructured omniphobic and superomniphobic surfaces with inexpensive CO_2 laser engraver," **ACS Applied Materials & Interfaces**, 9, p. 25656 (2017). *These authors contributed equally to the work.

- K. Bartlet, **S. Movafaghi**, A. K. Kota, K. C. Popat, "Superhemophobic titania nanotube array surfaces for blood contacting medical devices," **RSC Advances**, 7, p. 35466 (2017).

- **S. Movafaghi**, V. Leszczak, W. Wang, J. A. Sorkin, L. P. Dasi, K. C. Popat, A. K. Kota "Hemocompatibility of Superhemophobic Titania Surfaces," **Advanced Healthcare Materials**, accepted (2016).

- **S. Movafaghi**, W. Wang, A. Metzger, D. Williams, J. Williams, A. K. Kota, "Tunable Superomniphobic Surfaces for Sorting Droplets by Surface Tension," **Lab on a Chip**, 16, p. 3204 (2016).

- W. Wang, K. Lockwood, L. M. Boyd, M. D. Davidson, **S. Movafaghi**, H. Vahabi, S. R. Khetani, A. K. Kota, "Superhydrophobic Coatings with Edible Materials," **ACS Applied Materials & Interfaces**, 8, p. 18664 (2016).

- H. Vahabi, W. Wang, **S. Movafaghi**, A. K. Kota, "Free-Standing, Flexible, Superomniphobic Films," **ACS Applied Materials & Interfaces**, 8, p. 18664 (2016).

- D. L. Bark Jr, H. Vahabi, H. Bui, **S. Movafaghi**, B. Moore, A. K. Kota, K. Popat, and L. P. Dasi. "Hemodynamic Performance and Thrombogenic Properties of a Superhydrophobic Bileaflet Mechanical Heart Valve," **Annals of Biomedical Engineering**, p. 1 (2016).

CHAPTER 2 – BACKGROUND

2.1. Introduction

In the past two decades, inspired by biological surfaces with special wettabilities, liquid-repellent surfaces have received considerable attention because of their numerous applications such as anti-fouling,[1-2] self-cleaning,[3-7] liquid drag reduction,[8-10] chemical shielding,[11] icephobicity,[12-14] micro-robots,[15-16] anti-corrosion coatings,[17-18] enhanced dropwise condensation,[19-22] controlled manipulation of liquid droplets[23-26] and hemocompatible surfaces.[27-31] Liquid-repellent surfaces can be broadly classified as non-textured surfaces (e.g., smooth slippery surfaces on which droplets can slide easily)[32-35] and textured surfaces (e.g., super-repellent surfaces on which liquid droplets can bead up and roll off easily).[36-37] Super-repellency towards water was first observed in Lotus leaves and hence the term "Lotus effect" is commonly used to describe superhydrophobicity (i.e., the extreme repellency towards water; Figure 2.1a).[38-40] Detailed inspection of the Lotus leaves has established that appropriate surface chemistry and appropriate surface texture (and the associated physical principles) are the two important factors leading to superhydrophobicity.[40-42] In this chapter, the underlying chemical and physical principles of liquid-repellent surfaces (with the emphasis on super-repellent surfaces) are discussed and recent studies on tunable wettability (achieved by tuning the surface texture and surface chemistry) of super-repellent surfaces and their motivation will be presented.

2.2. Underlying Physics and Chemistry of Liquid-repellent Surfaces

The primary measure of wetting of a liquid on a non-textured (i.e., smooth) solid surface (Figure 2.1b) is the equilibrium (or Young's) contact angle θ, given by Young's equation:[43]

$$\cos\theta = \frac{\gamma_{sv} - \gamma_{sl}}{\gamma_{lv}} \qquad (2\text{-}1)$$

Here, γ_{sv}, γ_{sl} and γ_{lv} are the solid-vapor interfacial tension, the solid-liquid interfacial tension and the liquid-vapor interfacial tension, respectively. γ_{sv} and γ_{lv} are also known as the solid surface energy and the liquid surface tension, respectively. It is evident from the Young's relation (equation 2-1) that the solid surface energy γ_{sv} is inversely proportional to the contact angle θ. This implies that surfaces with very high surface energy tend to display lower contact angles, while surfaces with very low surface energy tend to display higher contact angles.[37] Therefore, surfaces with low surface energy are preferred for the design of super-repellent surfaces.

Hare *et al.*[44] reported that among various surface functional groups, the surface energy decreases in the order of $-CH_2 > -CH_3 > -CF_2 > -CF_2H > -CF_3$. Typically, low surface energy materials (i.e., $\gamma_{sv} < 35$ mNm^{-1} such as hydrocarbons with $\gamma_{sv} \approx 20\text{-}35$ mNm^{-1} and fluorocarbons with $\gamma_{sv} \approx 10\text{-}20$ mNm^{-1}) have become the logical choice of materials used for obtaining higher contact angles. Note that although the maximum contact angle of a water droplet reported on a non-textured surface is about 130°,[45-47] under certain conditions, textured surfaces can display much higher contact angles with a contacting liquid as described below.

When a liquid droplet contacts a textured (i.e., rough) solid surface, it displays an apparent contact angle θ^*, and it can adopt one of the following two configurations to minimize its overall free energy – the Wenzel[48] state or the Cassie-Baxter state.[49] In Wenzel state, the liquid can penetrate into the surface protrusions and fully wet the solid surface (Figure 2.1c). In this state, θ^* is calculated using the Wenzel relation:[48]

$$cos\,\theta^* = r\,cos\,\theta \qquad (2\text{-}2)$$

Here, r is the surface roughness and can be obtained from the ratio of the actual surface area to the projected surface area. As r is always greater than unity, roughness amplifies both the wetting and non-wetting behavior of surfaces in the Wenzel state. In other words, $\theta^* \ll 90°$ if $\theta < 90°$ and, $\theta^* \gg 90°$ if $\theta > 90°$. Typically, lower surface tension liquids (e.g., oils and alcohols) display Young's contact angle $\theta < 90°$. Consequently, such low surface tension liquids tend to display very low contact angles in the Wenzel state.
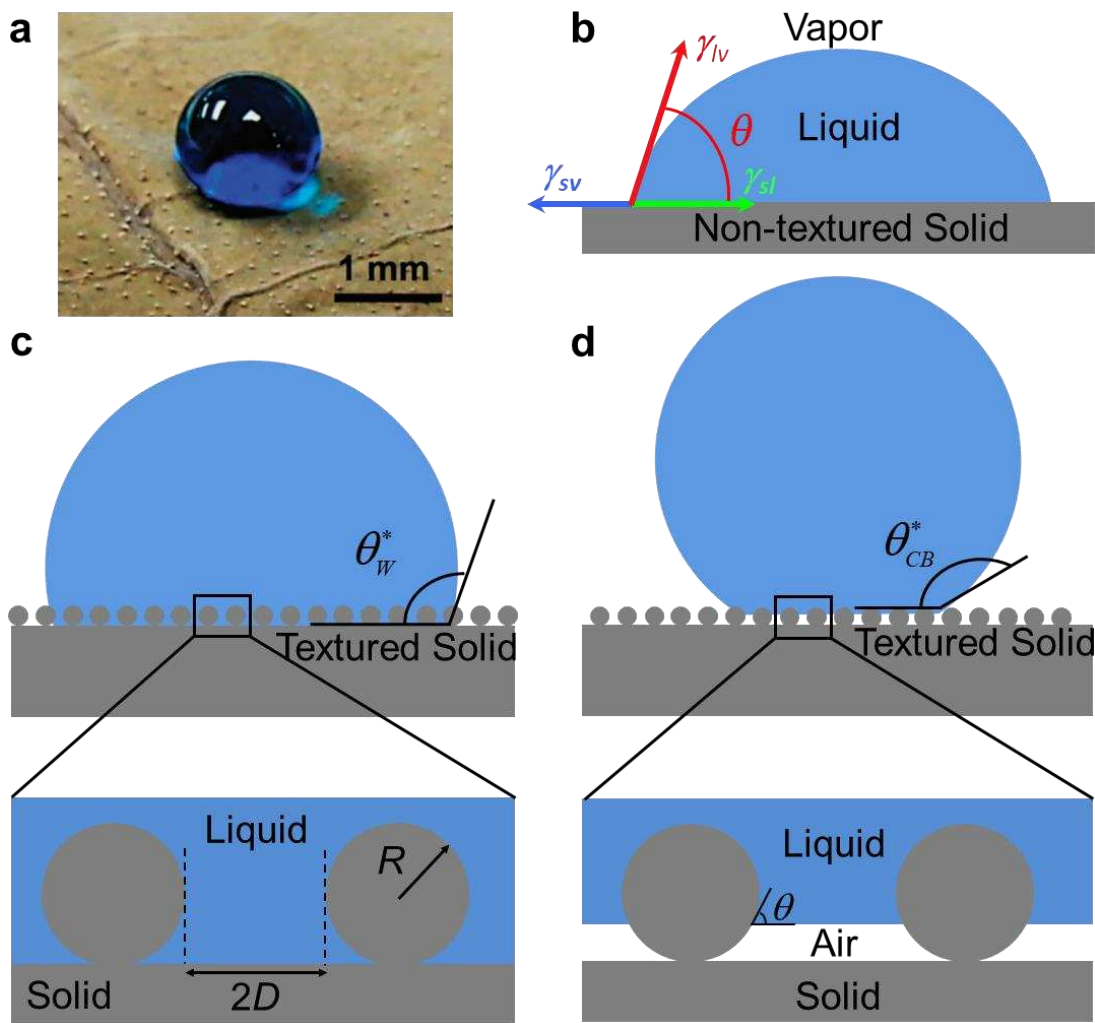
Figure 2.1. a) A droplet of water (dyed blue) beading up on a lotus leaf. Reproduced with permission.[37] © 2014 Nature Publishing Group. Schematic of a liquid droplet b) on a non-textured solid surface, c) in the Wenzel state, and d) in the Cassie-Baxter state on a textured solid surface. Note: θ^*, apparent contact angle; θ, contact angle; R, radius of the feature; D, half the inter-feature spacing.

In the Cassie-Baxter state, there are air pockets trapped between the solid (Figure 2.1d) and the liquid and θ^* is calculated using the Cassie-Baxter relation:[49]

$$cos\,\theta^* = f_{sl}\,cos\,\theta + f_{lv}\,cos\,\pi = f_{sl}\,cos\,\theta - f_{lv} \qquad (2\text{-}3)$$

Here, f_{sl} is the area fraction of the solid-liquid interface, which can be computed from the relation $f_{sl} = r_\phi\phi_s$; f_{lv} is the area fraction of the liquid-air interface underneath the liquid droplet on a uniformly textured surface. Note that r_ϕ is the roughness ratio of the wetted area and ϕ_s is the area fraction of the projected liquid-air interface occluded by the surface texture.[50] On surfaces with non-uniform roughness, f_{sl} and f_{lv} represent the local area fractions of the solid-liquid interface and the liquid-air interface, respectively, in the vicinity of the three-phase (solid-liquid-air) contact line.[51] It is evident from equation 2-3 that the Cassie-Baxter state can lead to apparent contact angle $\theta^* \gg 90°$ not only for $\theta > 90°$ but also for $\theta < 90°$, provided the solid-liquid area fraction f_{sl} is sufficiently low and the liquid-air area fraction f_{lv} is sufficiently high. In other words, in contrast to the Wenzel state, the formation of the Cassie-Baxter state can lead to very high contact angles even for low surface tension liquids (e.g., oils and alcohols). Further, the lower solid-liquid area fraction f_{sl} leads to a lower contact angle hysteresis $\Delta\theta^*$ (the difference between the advancing and receding contact angles; Figure 2.2a) for the Cassie-Baxter state when compared with the Wenzel state.[52-53] This results in a significantly lower solid-liquid interfacial area and so the lower solid-liquid interaction. The Cassie-Baxter state is preferred for designing super-repellent surfaces because it leads to high θ^* and low $\Delta\theta^*$.[52-53] Super-repellent surfaces can be broadly classified as superhydrophobic surfaces (i.e., surfaces that are extremely repellent to high surface tension liquids such as water) and superomniphobic surfaces (i.e., surfaces that are extremely repellent to both high surface tension liquids such as water and low

surface tension liquids such as oils and alcohols).[23-25,33] A surface is considered superhydrophobic if it displays $\theta^* > 150°$ and $\Delta\theta^* < 10°$ with water, and superoleophobic if it displays $\theta^* > 150°$ and $\Delta\theta^* < 10°$ with low surface tension liquids.[23-25,33] Therefore, superomniphobic surfaces (i.e., surfaces that are extremely repellent to virtually any liquid) are both superhydrophobic and superoleophobic.[23,24]

Contact angle hysteresis, the second important parameter for characterizing surface wettability, primarily arises from surface roughness and heterogeneity.[37, 54-55] It is related to the energy barriers that oppose the movement of a liquid droplet along a solid surface. In other words, contact angle hysteresis characterizes the resistance to droplet movement.[54-55] Consequently, low contact angle hysteresis achieved by Cassie-Baxter state facilitate the ease in mobility of the contacting liquid droplets and leads to low roll off angle ω of the liquid droplets on super-repellent surfaces. The roll off angle ω is defined as the minimum angle by which the surface must be tilted for the droplet to roll off from the surface (Figure 2.2b).
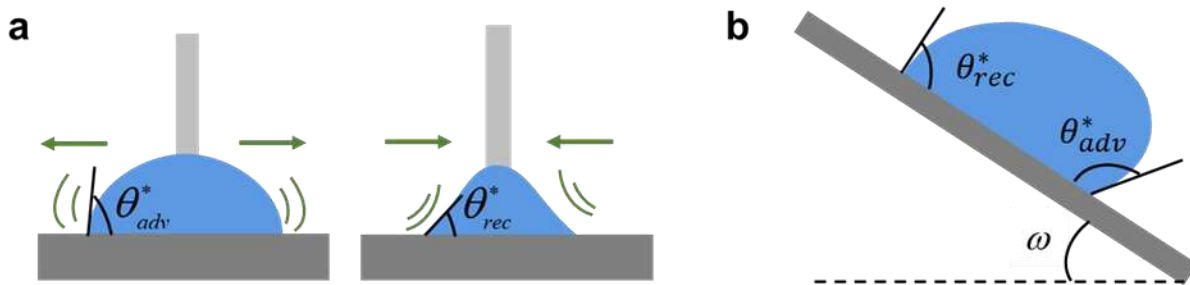
Figure 2.2. Schematic illustrating the a) advancing (the maximum) and receding (minimum) contact angles on a solid surface, b) a liquid droplet rolling off a tilted surface with the roll off angle of ω.

Moreover, employing hierarchically structured surfaces (i.e., surfaces possess more than one scale of texture; a finer length scale texture on an underlying coarser length scale texture) can lead to further decreasing of solid-liquid interfacial area and interaction (Figures 2.3a - 2.3c).[36-37] When a hierarchically structured surface supports a contacting liquid droplet in the Cassie-Baxter

state at all length scales, the liquid droplet displays higher apparent contact angles compared to surfaces that possess a single scale of texture. This is because of the air trapped at both the coarser length scale, as well as the finer length scale.
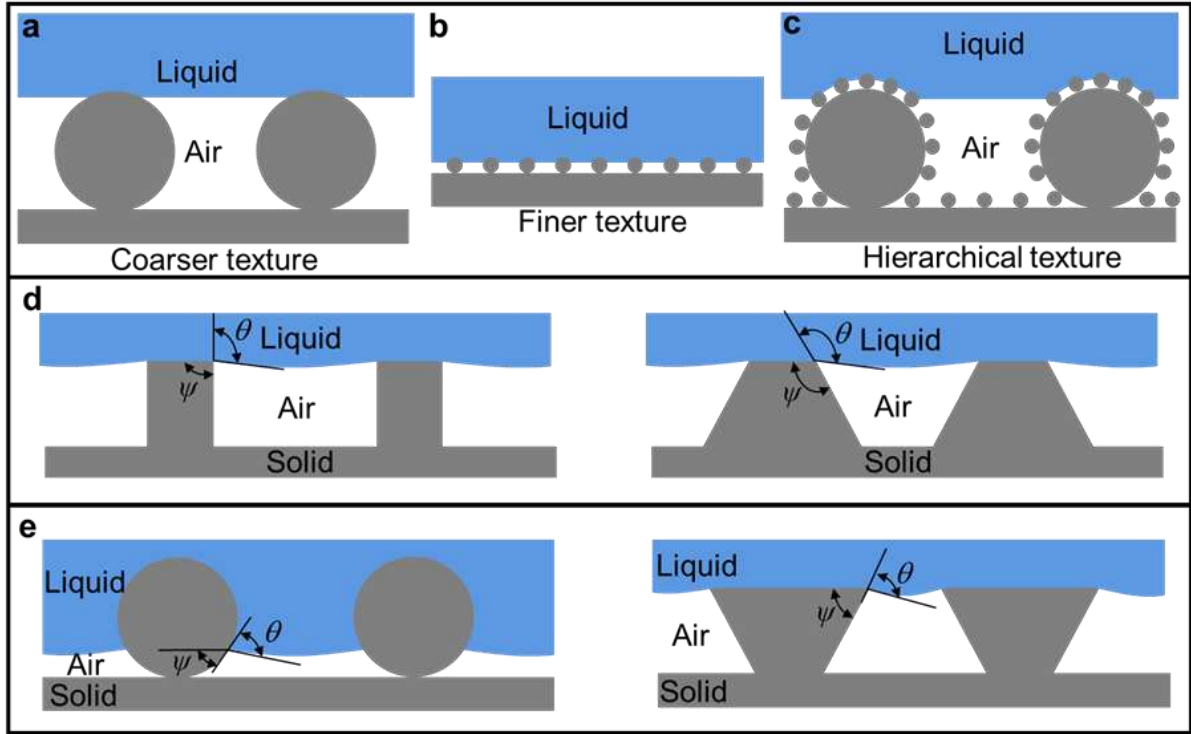
Figure 2.3. Schematics of a liquid droplet in the Cassie–Baxter state on a) a coarser textured surface, b) a finer textured surface, and c) a hierarchically textured surface, respectively. Schematics of a liquid droplet on d) concave textures with $\psi \geq 90°$ showing a liquid with $\theta > 90°$ in the Cassie-Baxter state, e) convex (re-entrant) textures with $\psi < 90°$ showing a liquid with $\theta < 90°$ in the Cassie-Baxter state. Note: ψ, local texture angle.

Although the formation of the Cassie-Baxter state is desirable in designing super-repellent surfaces, not all types of textures can lead to a Cassie-Baxter state for a contacting liquid. To illustrate this qualitatively, consider the two types of textures shown in Figures 2.3d and 2.3e, both having the same solid surface energy. The texture shown in Figure 2.3d is concave (texture angle $\psi > 90°$) and the texture shown in Figure 2.3e is convex ($\psi < 90°$) facing upwards. In both the cases, any liquid contacting the texture in the Cassie-Baxter state locally displays a contact angle equal to the Young's contact angle. A stable Cassie- Baxter state results only when $\theta \geq$

ψ.[11, 36-37, 56-58] This is because if $\theta < \psi$, the net traction on the liquid-vapor interface is downward due to the capillary force, which promotes imbibition of the liquid into the solid texture, leading to a fully wetted Wenzel state. When a liquid droplet comes in contact with a concave texture, Cassie-Baxter state is only possible with high surface tension liquids with high Young's contact angle ($\theta > 90°$).[58-59] Consequently, concave texture can only lead to superhydrophobic surfaces. On the other hand, when a liquid droplet comes in contact with a convex (or re-entrant) texture, Cassie-Baxter state is possible for both high and low surface tension liquids, so it can be superomniphobic.

Convex (or re-entrant) texture is necessary, but not sufficient for the formation of the Cassie-Baxter state for virtually all contacting liquids.[58, 60] Typically, the Cassie-Baxter state is a metastable state.[58, 60] When a sufficiently high pressure is applied on a liquid in the Cassie-Baxter state, regardless of the type of texture, the liquid will breakthrough (i.e., permeate and fully wet the protrusions), thereby transitioning to the Wenzel state. The breakthrough pressure $P_{breakthrough}$ is the minimum pressure that can force such a transition from the Cassie-Baxter state to the fully wetted Wenzel state. The breakthrough pressure $P_{breakthrough}$ can be determined from a force balance at the liquid-air interface. Typically, higher surface tension liquids and/or surface textures with smaller inter-feature spacings have higher $P_{breakthrough}$.[58, 60] Optimal super-repellent surfaces need to simultaneously display high $P_{breakthrough}$ and high apparent contact angles θ^* with the contacting liquid. High θ^* can be obtained from high liquid-air area fraction f_{lv}. One way of obtaining high f_{lv} is to design a texture with large inter-feature spacing. However, larger inter-feature spacings result in lower $P_{breakthrough}$. In order to obtain high $P_{breakthrough}$ without compromising high θ^*, it is essential to decrease the length scale of the texture. For example, consider a microstructure with $f_{lv,micro}$ and $P_{breakthrough,micro}$. Now, consider decreasing the length

scale of the texture to a nanostructure with $f_{lv,nano}$ and $P_{breakthrough,nano}$. If the nanostructure can be designed such that $f_{lv,micro} = f_{lv,nano}$, it will display a high θ^* similar to that obtained with the microstructure, but the nanostructure will have $P_{breakthrough,nano} \gg P_{breakthrough,micro}$ due to the smaller inter-feature spacing. In this manner, by designing textures on smaller length scales (e.g., nanostructure) with high liquid-air area fraction, one can obtain super-repellent surfaces that simultaneously display high breakthrough pressures and high apparent contact angles.

As discussed earlier, both the surface chemistry and the surface texture governs the surface wettability.[37, 61] Therefore, the wettability of super-repellent surfaces, i.e., the interaction of droplets with such surfaces can be tuned by changing the surface chemistry or surface texture. Super-repellent surfaces with tunable wettability and their tremendous applications have recently aroused great interest.

2.3. Tuning the Surface Texture

The primary studies on tuning the surface texture have been initiated by the evolution of superhydrophobic surfaces.[62-64] In order to investigate the dominant factors in superhydrophobicity, Shiu et al.[64] utilized lithography and oxygen plasma treatment to fabricate nano-textured surfaces with different liquid-solid contact area fractions. They showed that water contact angle can be adjusted from 132° to 170° on their fabricated surfaces (Figures 2.4a–2.4d). In another study, Acatay et al.[62] suggested that by increasing the viscosity of polymer solution, the surface texture of electrospun film can be altered from predominantly beads to only fibers. They discussed the significant role of surface texture in the final wetting behavior and concluded that the surfaces with beads are more hydrophobic than those consisting of only nanofibers.

Several studies have focused on the switching between different wettability states such as superhydrophobicity, hydrophobicity (i.e., contact angles > 90° with water), hydrophilicity (i.e.,

contact angles < 90° with water) and superhydrophilicity (i.e., contact angle < 10° with water). For example, Zhu *et al.*[65] altered the surface texture using silicon micromachining technology. In this manner, they adjusted the wettability of their silicon surfaces from hydrophobicity to superhydrophobicity. In another study, Zhang *et al.*[66] controlled the surface texture of an elastic polyamide film by cooperation of bi-axially extending and unloading the film. Their surfaces exhibited reversible wettability from superhydrophilicity upon extending to superhydrophobicity upon unloading. In a similar approach, polyester fabrics with switchable wettability via mechanical deformation were developed by Choi *et al.*[67] They utilized biaxial stretching of a fabric to create reversible wettability behavior of fabric surfaces between super-wetting and super-repellent with a wide range of liquids (Figures 2.4e–2.4h). Functional textiles, controllable drug release, and thermally responsive filters are among various applications, which may be aroused from such reversible surfaces.[68]
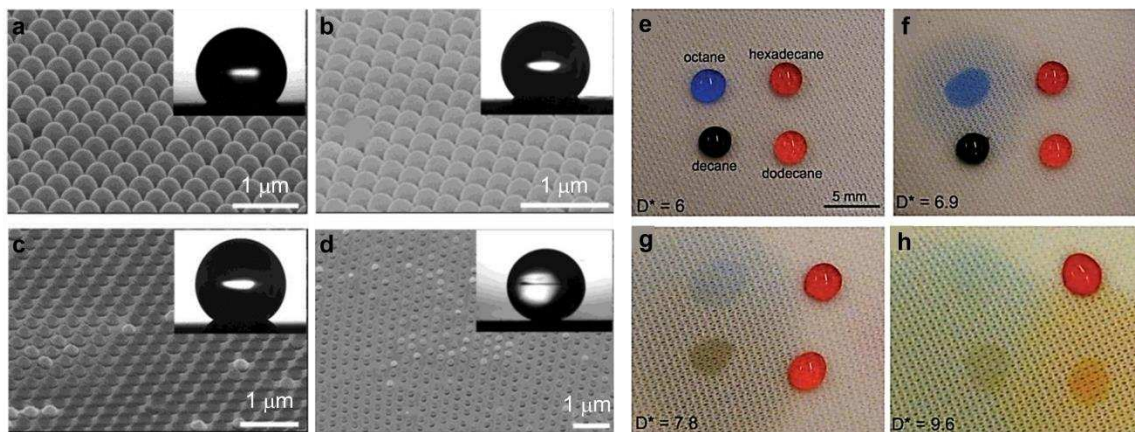
Figure 2.4. Scanning Electron Microscopy (SEM) images of the polystyrene beads. Insets indicate the water droplets on each surface. The diameters of polystyrene beads and water contact angles on these surfaces are, a) 400 nm, 135°, b) 360 nm, 144°, c) 330 nm, 152°, and d) 190 nm, 168°, respectively. Reproduced with permission.[64] © 2004 American Chemical Society. Sequential wetting of four alkane droplets on e) unstretched, f) 15% strained, g) 30% strained and h) 60% strained polyester fabric. Reproduced with permission.[67] 2009 Wiley.

2.4. Tuning the Surface Chemistry

Recently, much effort has been directed to tuning the surface chemistry of super-repellent surfaces using an external stimulus such as thermal treatment,[68] pH/solvent sensitivity,[69-71] chemical deposition,[72-73] light irradiation,[74-78] plasma treatment[79-80] and electric field[81-84] (see Figure 2.5). As an example, for thermal treatment stimulus, Sun *et al.*[68] studied the reversible switching of superhydrophobic surfaces induced by controlling the temperature. They showed that the wettability of poly (N-isopropylacrylamide)-modified surfaces can be dramatically changed from superhydrophilicity to superhydrophobicity by increasing the temperature by only 30° C. In order to fabricate a pH-responsive surface, Yu *et al.*[71] combined a fractal-like gold surface obtained via electrodeposition technique and a mixed thiol self-assembled monolayer to create an acid/base sensitive surface. They observed that their surface is superhydrophobic with acidic droplets and superhydrophilic with basic water droplets.

In another study, Minko *et al.*[70] studied controlling of a polymer surface wettability by exposing the surface to different solvents. The solvent sensitivity evoked the switchable wettability from superhydrophilic to superhydrophobic state. Kietzig *et al.*[73] created superhydrophilic surfaces with different metal alloys using femtosecond laser irradiation of different metal alloys. However, they observed that surfaces kept in air, became superhydrophobic after about 10 days and this change was attributed to the deposition of carbon on the laser-textured surface.

Several studies have investigated a variety of photo-responsive materials such as V_2O_5, ZnO, TiO_2, etc., for fabrication of super-repellent surfaces with controllable surface wettability.[85] Lim *et al.*[76] reported the fabrication of rose-like nanostructured V_2O_5 films that are photo-responsive. The wettability of textured V_2O_5 films was reversed from superhydrophobicity to

superhydrophilicity upon UV light irradiation. In another study, Huang *et al.*[75] prepared carbon nanotubes on silicon substrates using chemical vapor deposition followed by a ZnO layer deposition. The initially fabricated surfaces showed superhydrophobic behavior, however, surfaces turned to hydrophilic after UV light irradiation.
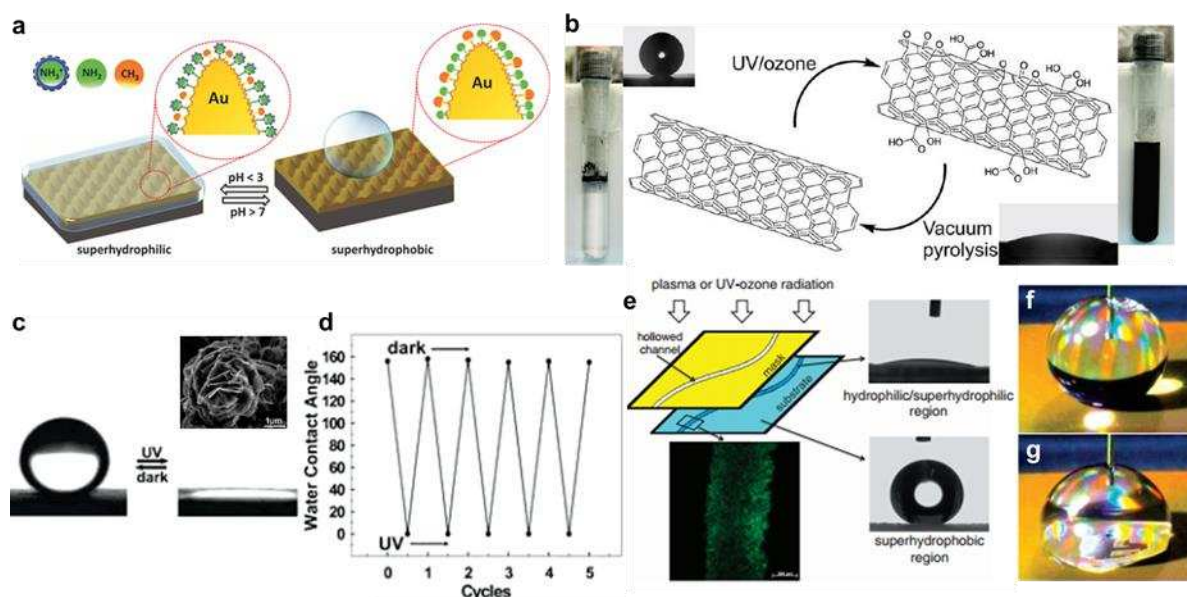
Figure 2.5. a) The transformation of surface wetting properties in response to different pH values after modification with a mixed self-assembled monolayer. Reproduced with permission.[69] © 2013 Wiley. b) Switchable wettability using UV/ozone and vacuum pyrolysis treatments. Oxygen adsorption occurs during UV/ozone treatment, and oxygen desorption occurs during vacuum pyrolysis treatment. Reproduced with permission.[74] © 2011 American Chemical Society. c) Reversible contact angles of water droplet and d) wettability transitions through UV exposure and dark storage of V_2O_5 surface. The inset indicates the SEM image of a rose-garden-like nanostructured V_2O_5. Reproduced with permission.[76] © 2007 American Chemical Society. e) Schematic of hydrophilic/superhydrophilic channel like regions, which can be imprinted onto superhydrophobic surfaces. Reproduced with permission.[77] © 2011 IOP Publishing. The fluorescent microscopy image highlights the section of a superhydrophilic channel on the superhydrophobic surface. Electrically induced reversible transitions is demonstrated f) before and g) after applying voltage. Reproduced with permission.[82] © 2007 American Chemical Society.

More recently, Aria and Gharib[74] reported that the wettability of carbon nanotube arrays can be tuned by controlling the oxygenated functional groups concentrations induced by UV/ozone irradiation. Low amount of oxygenated functional groups exhibits a superhydrophobic behavior. In contrast, high surface concentration of oxygenated functional groups exhibits superhydrophilic behavior leading to a reversible wettability. As another external stimulus,

plasma treatment was used by Song *et al.*[80] to create superhydrophobic surface with controllable wettability. They synthesized poly (L-lactic acid) (PLLA) superhydrophobic surfaces using phase inversion-based methods. They showed that by increasing Ar-plasma treatment hydrophilicity of the samples increases.

In recent years, tuning the surface chemistry via electric field (i.e., electrowetting) turned to an interesting topic due to its simplicity and reproducibility.[86] Ahuja *et al.*[87] demonstrated superlyophobic surfaces (i.e., surfaces showing contact angles >150° with a wide range of liquids) with nanonail texture. They reported that the surface wettability can be reversibly switched between superlyophobic and fully wet surfaces by applying electrical voltage and current.

2.5. Motivation Behind Tuning Wettability

Tuning the interaction of liquid droplets with super-repellent surfaces by tuning the surface wettability has several applications in the fields of patterned surfaces, oil-water separation membranes, manipulation of droplets and controllable adhesion.

2.5.1. Patterned Surfaces

Fabrication of patterned surfaces, resulting from controlling the surface wettability has attained interest owing to its great number of applications.[88] Micro-condensation for water collection[89-91] and high resolution printing[92-93] can be named as a few out of many applications of patterned surfaces (see Figure 2.6).

In order to mimic water harvesting property of Namib desert beetle, Zhai *et al.*[91] suggested a patterned surface. For fabrication of the patterned surface, they first synthesized a superhydrophobic surface using polyelectrolyte multilayer films and then created hydrophilic domains by selective delivery of a philic solution on the superhydrophobic surface. Later, Garrod

et al.[90] and Dorrer and Ruhe[89] developed microcondensers for water collecting by creating hydrophilic domains on a superhydrophobic surface. They investigated the parameters like wettability and size of domains and droplets volume for efficient water collecting. For printing, Nishimoto *et al.*[93] fabricated superhydrophobic surfaces using ODP-modified textured TiO_2 surfaces and adjusted the wettability using UV irradiation. They reported enhanced resolution of such patterned surfaces in off-set printing (Figures 2.6a and 2.6b). In their other work,[92] they showed rewritable surfaces owing to photocatalytic activity of TiO_2 surfaces.
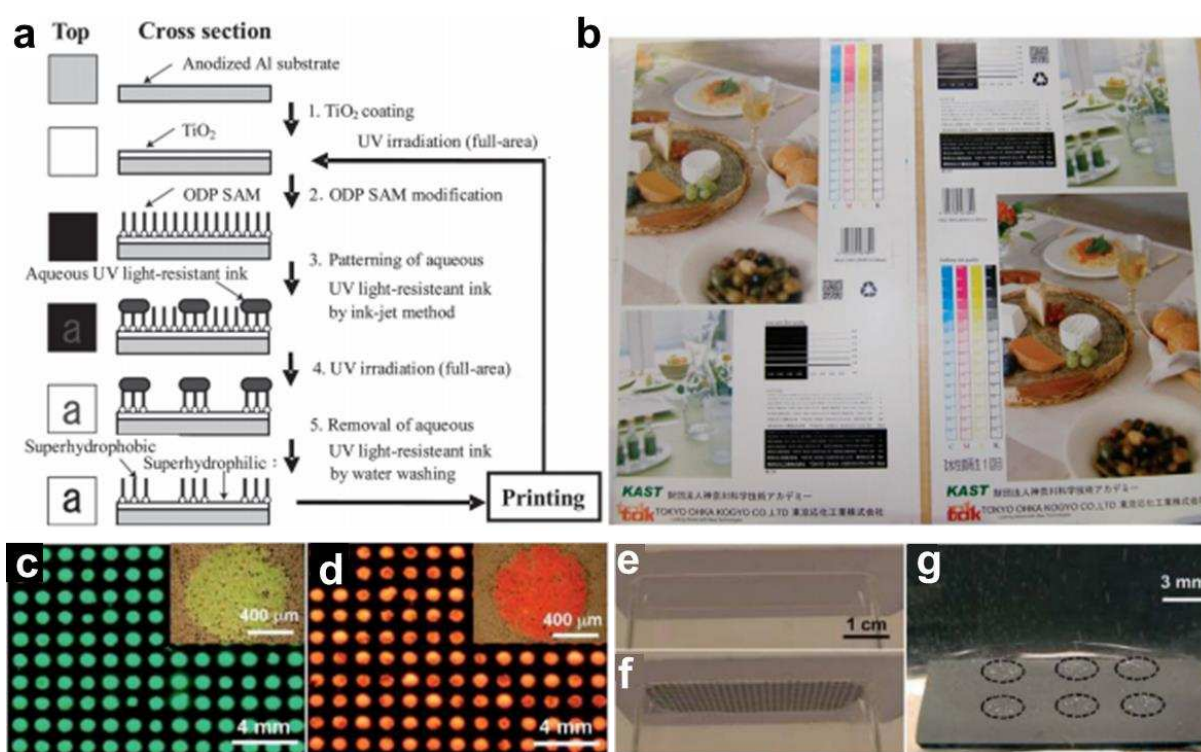
Figure 2.6. Off-set printing based on the superhydrophilic–superhydrophobic patterns. a) Schematic diagram of the patterning and reusing processes and b) Photographs of posters printed by the pristine plate (left) and reused plate (right). Reproduced with permission.[93] © 2009 Elsevier. c) and d) Site-selective self-assembly of UV fluorescent green microspheres dispersed in water and UV fluorescent red microspheres dispersed in heptane, respectively. Superomniphobic surface patterned with superomniphilic domains e) before and f) after exposure, respectively, to heptane vapors. g) Vapor bubbles nucleation of boiling methanol on the superomniphobic domains. Reproduced with permission.[94] © 2012 Wiley.

2.5.2. Water-Oil Separation Membranes

Tuning the surface wettability plays a critical role in several oil-water separation techniques out of which a few studies are presented here (Figure 2.7).[95-101] As one of the very first studies, Feng *et al.*[96] fabricated a superhydrophobic/superoleophilic by spray coating polytetrafluoroethylene (PTFE) surface onto a stainless-steel mesh. They demonstrated the separation of diesel oil and water using their engineered surfaces. Later, Tian *et al.*[98] presented a switchable superhydrophobic ZnO-coated stainless-steel mesh film, which induced a photo-induced water–oil separation. Recently, Jian *et al.*[97] fabricated a superhydrophobic/superoleophilic sponge using PTFE coated SiO_2 surfaces. Such surface exhibited oil spills removal property.
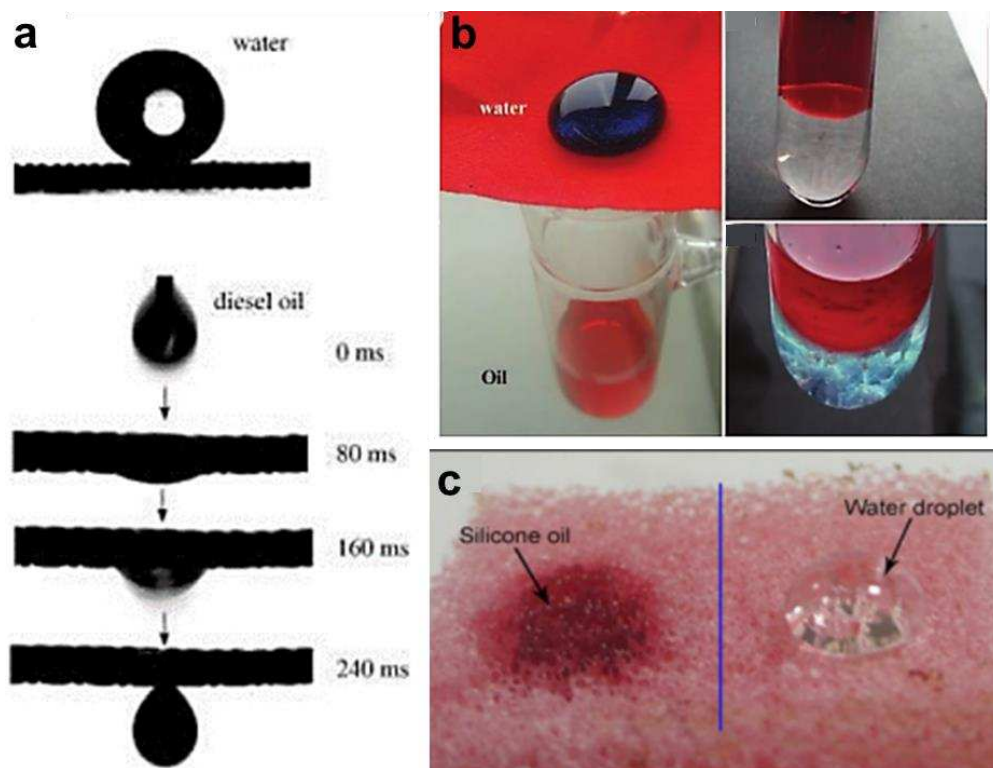
Figure 2.7. a) Water droplet with high contact angle and spreading and permeating behavior of a diesel oil on a mesh showing superhydrophobicity and superoleophilicity. Reproduced with permission.[96] © 2012 Wiley. b) Oil/water separation using modified silicone nanofilaments on polyester textile. Reproduced with permission.[101] © 2011 Wiley. c) Water droplet and oil droplet on the surface of PU/PTFE/A-SiO_2/SiO_2. Reproduced with permission.[97] © 2013 Materials Research Society.

2.5.3. Droplet Movement and Manipulation of Droplets

Spontaneous movement of droplets as a consequence of gradient in wettability of a surface has been demonstrated in numerous studies (Figure 2.8). With a solid surface energy gradient, a droplet may be able to move on the surface from the lower solid surface energy end towards the higher one by a net force, as a result of the imbalance of surface forces acting on the two opposite sides of the liquid–solid contact line. Controlling droplet motion in desired manner or in another word manipulation of droplets on super-repellent surfaces has been shown using various methods including electric fields[87, 102-104] and wettability gradients[105-110] to enable the transportation, trapping, merging and splitting of droplets on super-repellent surfaces.
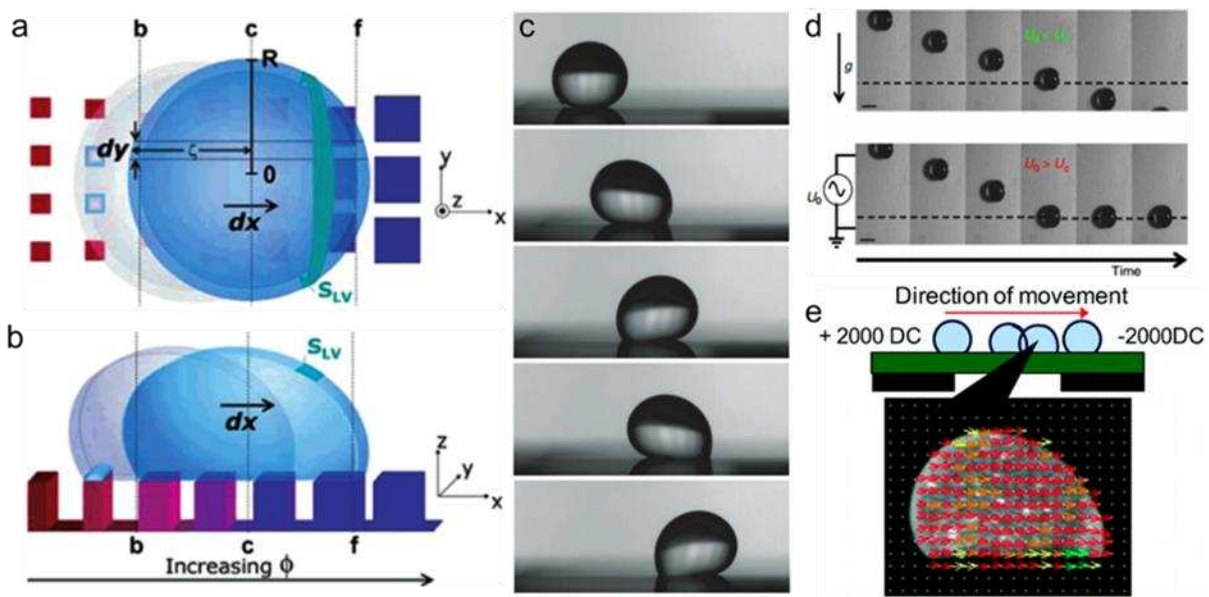
Figure 2.8. Droplet movement due to a wettability gradient, a) top view and b) side view. Reproduced with permission.[111] © 2006 American Chemical Society. c) The motion of a water droplet on a surface with a variable density of micro-textures. The time interval between two snapshots is 8 s. Reproduced with permission.[110] © 2009 IOP Publishing. d) Snapshots showing the droplet trapping at electrically tunable wetting defects on an inclined superhydrophobic surface. Reproduced with permission.[102] © 2014 Nature Publishing Group. e) Movement of droplets induced by an electric field. Reproduced with permission.[112] © 2010 American Chemical Society.

Zhu *et al.*[65] fabricated superhydrophobic surfaces via Octadecyltrichlorosilane (OTS) coated silicon micro-pillars and created a tunable wettability using controlling the inter-pillar spacing.

They observed the spontaneous movement of a droplet on a surface with a certain roughness spatial gradient. In addition, a number of other studies have introduced gradient wettability using tuning the surface texture to evoke droplet motion.[23, 111, 113] In another study, Wang *et al.*[114] utilized a brush containing animal hairs allowing the manipulation of low-viscosity liquid ink in a controlled manner. Such functionality was attributed to the anisotropic multi-scale structural feature of hairs.

2.5.4. Controllable Adhesion

Recently, there has been significant interest in superhydrophobic surfaces with controllable adhesion (Figure 2.9).[115] Lai *et al.*[116] Utilized basic principles of capillary-induced adhesion and roughness-enhanced hydrophobicity and designed different types of superhydrophobic porous-nanostructure models with controllable water-adhesive force ranging from very high to extremely low. They found that the water adhesive force of the superhydrophobic nano-textured surface can be tuned by changing the diameter and length of nanotubes. Dawood *et al.*[117] produced rose petal and lotus effects on the silicon wafer by a chemical etching process using H_2O_2 and HF, which revealed superhydrophobicity. Tuning the morphology of nanowires on the Si surface leads to spatially selective adhesive behavior.

Controllable adhesion has been studied for biological applications, such as protein adsorption and controlled cell adhesion/detachment. For example, Ballester-Beltran *et al.*[120] fabricated a superhydrophobic surface, consisting of a micro and nanotextured (i.e., hierarchically textured) polystyrene (PS) ($\gamma_{sv} \approx 35$ mNm^{-1}) surface, using a phase separation method. They investigated the adsorption of fibronectin on their superhydrophobic PS surface and compared it with that on a non-textured PS surface. Their results indicate about 60% reduction in the amount of adsorbed fibronectin on superhydrophobic PS surface compared to the non-textured PS surface. Shiu *et*

al.[121] utilized switchable superhydrophobic surfaces created by electrowetting to develop addressable protein patterning microarrays. They fabricated Teflon-based superhydrophobic surface using a combination of nano-sphere lithography and plasma treatment. They showed that high protein resistance of superhydrophobic surfaces can be switched to an enhanced protein adsorption in superhydrophilic state. As another example, Li *et al.*[122] fabricated superhydrophobic surfaces using microtextured polypropylene (PP) ($\gamma_{sv} \approx 20$ mNm^{-1}) surfaces via solvent-nonsolvent technique. By comparing the whole blood interaction with smooth and superhydrophobic PP, they indicated that the rupture and adhesion of red blood cells are remarkably reduced on the superhydrophobic PP compared to the smooth PP.
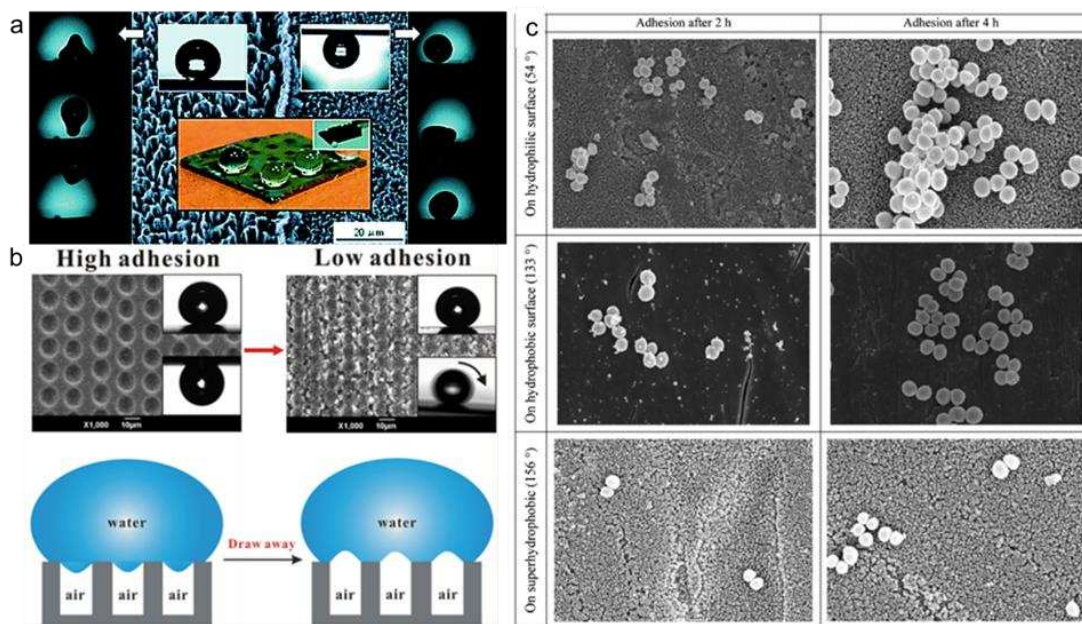
Figure 2.9. a) Spatially selective adhesion behavior by controlling the morphologies of Silicon nanowire arrays. Reproduced with permission.[117] © 2011 American Chemical Society. b) A transition between the superhydrophobic surface with ultrahigh adhesion and the superhydrophobic surface with ultralow adhesion for the PDMS surfaces irradiated by a femtosecond laser. Reproduced with permission.[118] © 2013 American Chemical Society. c) SEM images of Staphylococcus aureus adhesion after 2 h and 4 h on hydrophilic, hydrophobic and superhydrophobic surfaces. Reproduced with permission.[119] © 2011 Peifu Tang *et al.*

In the following four chapters, droplet manipulation and controlled adhesion that I obtained from tailored wettability of liquid-repellent surfaces and their applications have been discussed.

REFERENCES

(1) Genzer, J.; Efimenko, K. Recent developments in superhydrophobic surfaces and their relevance to marine fouling: a review. *Biofouling* **2006,** *22*, 339-360.

(2) Privett, B. J.; Youn, J.; Hong, S. A.; Lee, J.; Han, J.; Shin, J. H.; Schoenfisch, M. H. Antibacterial fluorinated silica colloid superhydrophobic surfaces. *Langmuir* **2011,** *27*, 9597-9601.

(3) Bhushan, B.; Jung, Y. C.; Koch, K. Self-cleaning efficiency of artificial superhydrophobic surfaces. *Langmuir* **2009,** *25*, 3240-3248.

(4) Fürstner, R.; Barthlott, W.; Neinhuis, C.; Walzel, P. Wetting and self-cleaning properties of artificial superhydrophobic surfaces. *Langmuir* **2005,** *21*, 956-961.

(5) Nishimoto, S.; Bhushan, B. Bioinspired self-cleaning surfaces with superhydrophobicity, superoleophobicity, and superhydrophilicity. *Rsc Advances* **2013,** *3*, 671-690.

(6) Wisdom, K. M.; Watson, J. A.; Qu, X.; Liu, F.; Watson, G. S.; Chen, C.-H. Self-cleaning of superhydrophobic surfaces by self-propelled jumping condensate. *Proceedings of the National Academy of Sciences* **2013,** *110*, 7992-7997.

(7) Vahabi, H.; Wang, W.; Movafaghi, S.; Kota, A. K. Free-standing, flexible, superomniphobic films. *ACS applied materials & interfaces* **2016,** *8*, 21962-21967.

(8) Bhushan, B.; Jung, Y. C. Natural and biomimetic artificial surfaces for superhydrophobicity, self-cleaning, low adhesion, and drag reduction. *Progress in Materials Science* **2011,** *56*, 1-108.

(9) Daniello, R. J.; Waterhouse, N. E.; Rothstein, J. P. Drag reduction in turbulent flows over superhydrophobic surfaces. *Physics of Fluids (1994-present)* **2009,** *21*, 085103.

(10) Ou, J.; Perot, B.; Rothstein, J. P. Laminar drag reduction in microchannels using ultrahydrophobic surfaces. *Physics of Fluids (1994-present)* **2004,** *16*, 4635-4643.

(11) Pan, S.; Kota, A. K.; Mabry, J. M.; Tuteja, A. Superomniphobic surfaces for effective chemical shielding. *Journal of the American Chemical Society* **2012,** *135*, 578-581.

(12) Boreyko, J. B.; Collier, C. P. Delayed frost growth on jumping-drop superhydrophobic surfaces. *ACS nano* **2013,** *7*, 1618-1627.

(13) Jafari, R.; Menini, R.; Farzaneh, M. Superhydrophobic and icephobic surfaces prepared by RF-sputtered polytetrafluoroethylene coatings. *Applied Surface Science* **2010,** *257*, 1540-1543.

(14) Varanasi, K. K.; Deng, T.; Smith, J. D.; Hsu, M.; Bhate, N. Frost formation and ice adhesion on superhydrophobic surfaces. *Applied Physics Letters* **2010,** *97*, 234102.

(15) Jiang, L.; Yao, X.; Li, H.; Fu, Y.; Chen, L.; Meng, Q.; Hu, W.; Jiang, L. "Water Strider" Legs with a Self-Assembled Coating of Single-Crystalline Nanowires of an Organic Semiconductor. *Advanced Materials* **2010,** *22*, 376-379.

(16) Zhang, X.; Zhao, J.; Zhu, Q.; Chen, N.; Zhang, M.; Pan, Q. Bioinspired aquatic microrobot capable of walking on water surface like a water strider. *ACS applied materials & interfaces* **2011,** *3*, 2630-2636.

(17) Isimjan, T. T.; Wang, T.; Rohani, S. A novel method to prepare superhydrophobic, UV resistance and anti-corrosion steel surface. *Chemical engineering journal* **2012,** *210*, 182-187.

(18) Liu, T.; Chen, S.; Cheng, S.; Tian, J.; Chang, X.; Yin, Y. Corrosion behavior of super-hydrophobic surface on copper in seawater. *Electrochimica Acta* **2007,** *52*, 8003-8007.

(19) Enright, R.; Miljkovic, N.; Alvarado, J. L.; Kim, K.; Rose, J. W. Dropwise condensation on micro-and nanostructured surfaces. *NANOSC MICROSC THERM.* **2014,** *18*, 223-250.

(20) Attinger, D.; Frankiewicz, C.; Betz, A. R.; Schutzius, T. M.; Ganguly, R.; Das, A.; Kim, C.-J.; Megaridis, C. M. Surface engineering for phase change heat transfer: A review. *MRS Energy & Sustainability* **2014,** *1*.

(21) Vahabi, H.; Wang, W.; Davies, S.; Mabry, J. M.; Kota, A. K. Coalescence-Induced Self-Propulsion of Droplets on Superomniphobic Surfaces. *ACS Appl. Mater. Interfaces* **2017,** *9*, 29328-29336.

(22) Miljkovic, N.; Enright, R.; Nam, Y.; Lopez, K.; Dou, N.; Sack, J.; Wang, E. N. Jumping-droplet-enhanced condensation on scalable superhydrophobic nanostructured surfaces. *Nano Lett.* **2012,** *13*, 179-187.

(23) Fang, G.; Li, W.; Wang, X.; Qiao, G. Droplet motion on designed microtextured superhydrophobic surfaces with tunable wettability. *Langmuir* **2008,** *24*, 11651-11660.

(24) Zhao, Y.; Fang, J.; Wang, H.; Wang, X.; Lin, T. Magnetic liquid marbles: manipulation of liquid droplets using highly hydrophobic Fe_3O_4 nanoparticles. *Advanced materials* **2010,** *22*, 707-710.

(25) Movafaghi, S.; Wang, W.; Metzger, A.; Williams, D.; Williams, J.; Kota, A. Tunable superomniphobic surfaces for sorting droplets by surface tension. *Lab on a Chip* **2016,** *16*, 3204-3209.

(26) Pendurthi, A.; Movafaghi, S.; Wang, W.; Shadman, S.; Yalin, A. P.; Kota, A. K. Fabrication of nanostructured omniphobic and superomniphobic surfaces with inexpensive CO2 laser engraver. *ACS applied materials & interfaces* **2017,** *9*, 25656-25661.

(27) Khorasani, M.; Mirzadeh, H. In vitro blood compatibility of modified PDMS surfaces as superhydrophobic and superhydrophilic materials. *Journal of applied polymer science* **2004,** *91*, 2042-2047.

(28) Mao, C.; Liang, C.; Luo, W.; Bao, J.; Shen, J.; Hou, X.; Zhao, W. Preparation of lotus-leaf-like polystyrene micro-and nanostructure films and its blood compatibility. *Journal of Materials Chemistry* **2009,** *19*, 9025-9029.

(29) Bark, D. L.; Vahabi, H.; Bui, H.; Movafaghi, S.; Moore, B.; Kota, A. K.; Popat, K.; Dasi, L. P. Hemodynamic performance and thrombogenic properties of a superhydrophobic bileaflet mechanical heart valve. *Annals of biomedical engineering* **2017,** *45*, 452-463.

(30) Bartlet, K.; Movafaghi, S.; Kota, A.; Popat, K. C. Superhemophobic titania nanotube array surfaces for blood contacting medical devices. *RSC Advances* **2017,** *7*, 35466-35476.

(31) Movafaghi, S.; Leszczak, V.; Wang, W.; Sorkin, J. A.; Dasi, L. P.; Popat, K. C.; Kota, A. K. Hemocompatibility of superhemophobic titania surfaces. *Advanced healthcare materials* **2017,** *6*.

(32) Boban, M.; Golovin, K.; Tobelmann, B.; Gupte, O.; Mabry, J. M.; Tuteja, A. Smooth, All-Solid, Low-Hysteresis, Omniphobic Surfaces with Enhanced Mechanical Durability. *ACS applied materials & interfaces* **2018,** *10*, 11406-11413.

(33) Wang, L.; McCarthy, T. J. Covalently attached liquids: instant omniphobic surfaces with unprecedented repellency. *Angewandte Chemie* **2016,** *128*, 252-256.

(34) Hu, H.; Liu, G.; Wang, J. Clear and durable epoxy coatings that exhibit dynamic omniphobicity. *Advanced Materials Interfaces* **2016,** *3*.

(35) Wooh, S.; Vollmer, D. Silicone Brushes: Omniphobic Surfaces with Low Sliding Angles. *Angewandte Chemie International Edition* **2016,** *55*, 6822-6824.

(36) Kota, A. K.; Choi, W.; Tuteja, A. Superomniphobic surfaces: design and durability. *MRS bulletin* **2013,** *38*, 383-390.

(37) Kota, A. K.; Kwon, G.; Tuteja, A. The design and applications of superomniphobic surfaces. *NPG Asia Materials* **2014,** *6*, e109.

(38) Cheng, Y. T.; Rodak, D.; Wong, C.; Hayden, C. Effects of micro-and nano-structures on the self-cleaning behaviour of lotus leaves. *Nanotechnology* **2006,** *17*, 1359.

(39) Marmur, A. The lotus effect: superhydrophobicity and metastability. *Langmuir* **2004,** *20*, 3517-3519.

(40) Feng, L.; Li, S.; Li, Y.; Li, H.; Zhang, L.; Zhai, J.; Song, Y.; Liu, B.; Jiang, L.; Zhu, D. Super-hydrophobic surfaces: from natural to artificial. *Adv. Mater.* **2002,** *14*, 1857-1860.

(41) Vahabi, H.; Wang, W.; Popat, K. C.; Kwon, G.; Holland, T. B.; Kota, A. K. Metallic superhydrophobic surfaces via thermal sensitization. *Appl. Phys. Lett.* **2017,** *110*, 251602.

(42) Wang, W.; Lockwood, K.; Boyd, L. M.; Davidson, M. D.; Movafaghi, S.; Vahabi, H.; Khetani, S. R.; Kota, A. K. Superhydrophobic coatings with edible materials. *ACS Appl. Mater. Interfaces* **2016,** *8*, 18664-18668.

(43) Young, T. An essay on the cohesion of fluids. *Philosophical Transactions of the Royal Society of London* **1805,** *95*, 65-87.

(44) Hare, E.; Shafrin, E.; Zisman, W. Properties of films of adsorbed fluorinated acids. *J.Phys. Chem.* **1954,** *58*, 236-239.

(45) Kota, A. K.; Mabry, J. M.; Tuteja, A. Superoleophobic surfaces: design criteria and recent studies. *Surface Innovations* **2013,** *1*, 71-83.

(46) Genzer, J.; Efimenko, K. Creating long-lived superhydrophobic polymer surfaces through mechanically assembled monolayers. *Science* **2000,** *290*, 2130-2133.

(47) Nishino, T.; Meguro, M.; Nakamae, K.; Matsushita, M.; Ueda, Y. The lowest surface free energy based on− CF3 alignment. *Langmuir* **1999,** *15*, 4321-4323.

(48) Wenzel, R. N. Resistance of solid surfaces to wetting by water. *Industrial & Engineering Chemistry* **1936,** *28*, 988-994.

(49) Cassie, A.; Baxter, S. Wettability of porous surfaces. *Transactions of the Faraday Society* **1944,** *40*, 546-551.

(50) Marmur, A. Wetting on hydrophobic rough surfaces: to be heterogeneous or not to be? *Langmuir* **2003,** *19*, 8343-8348.

(51) Choi, W.; Tuteja, A.; Mabry, J. M.; Cohen, R. E.; McKinley, G. H. A modified Cassie–Baxter relationship to explain contact angle hysteresis and anisotropy on non-wetting textured surfaces. *Journal of colloid and interface science* **2009,** *339*, 208-216.

(52) Patankar, N. A. On the modeling of hydrophobic contact angles on rough surfaces. *Langmuir* **2003,** *19*, 1249-1253.

(53) Gao, L.; McCarthy, T. J. The "lotus effect" explained: two reasons why two length scales of topography are important. *Langmuir* **2006,** *22*, 2966-2967.

(54) Johnson Jr, R. E.; Dettre, R. H. Contact angle hysteresis. III. Study of an idealized heterogeneous surface. *The journal of physical chemistry* **1964,** *68*, 1744-1750.

(55) Dettre, R. H.; Johnson Jr, R. E. Contact Angle Hysteresis. IV. Contact Angle Measurements on Heterogeneous Surfaces1. *The journal of physical chemistry* **1965,** *69*, 1507-1515.

(56) Grigoryev, A.; Tokarev, I.; Kornev, K. G.; Luzinov, I.; Minko, S. Superomniphobic magnetic microtextures with remote wetting control. *J. Am. Chem. Soc.* **2012,** *134*, 12916-12919.

(57) Mazumder, P.; Jiang, Y.; Baker, D.; Carrilero, A.; Tulli, D.; Infante, D.; Hunt, A. T.; Pruneri, V. Superomniphobic, transparent, and antireflection surfaces based on hierarchical nanostructures. *Nano Lett.* **2014,** *14*, 4677-4681.

(58) Tuteja, A.; Choi, W.; Mabry, J. M.; McKinley, G. H.; Cohen, R. E. Robust omniphobic surfaces. *Proceedings of the National Academy of Sciences* **2008,** *105*, 18200-18205.

(59) Wang, W.; Salazar, J.; Vahabi, H.; Joshi-Imre, A.; Voit, W. E.; Kota, A. K. Metamorphic superomniphobic surfaces. *Adv. Mater.* **2017,** *29*.

(60) Tuteja, A.; Choi, W.; Ma, M.; Mabry, J. M.; Mazzella, S. A.; Rutledge, G. C.; McKinley, G. H.; Cohen, R. E. Designing superoleophobic surfaces. *Science* **2007,** *318*, 1618-1622.

(61) Miwa, M.; Nakajima, A.; Fujishima, A.; Hashimoto, K.; Watanabe, T. Effects of the surface roughness on sliding angles of water droplets on superhydrophobic surfaces. *Langmuir* **2000,** *16*, 5754-5760.

(62) Acatay, K.; Simsek, E.; Ow-Yang, C.; Menceloglu, Y. Z. Tunable, superhydrophobically stable polymeric surfaces by electrospinning. *Angewandte Chemie International Edition* **2004,** *43*, 5210-5213.

(63) Jin, M.; Feng, X.; Xi, J.; Zhai, J.; Cho, K.; Feng, L.; Jiang, L. Super-hydrophobic PDMS surface with ultra-low adhesive force. *Macromolecular rapid communications* **2005,** *26*, 1805-1809.

(64) Shiu, J.-Y.; Kuo, C.-W.; Chen, P.; Mou, C.-Y. Fabrication of tunable superhydrophobic surfaces by nanosphere lithography. *Chemistry of materials* **2004,** *16*, 561-564.

(65) Zhu, L.; Feng, Y.; Ye, X.; Zhou, Z. Tuning wettability and getting superhydrophobic surface by controlling surface roughness with well-designed microstructures. *Sensors and Actuators A: Physical* **2006,** *130*, 595-600.

(66) Zhang, J.; Lu, X.; Huang, W.; Han, Y. Reversible superhydrophobicity to superhydrophilicity transition by extending and unloading an elastic polyamide film. *Macromolecular rapid communications* **2005,** *26*, 477-480.

(67) Choi, W.; Tuteja, A.; Chhatre, S.; Mabry, J. M.; Cohen, R. E.; McKinley, G. H. Fabrics with tunable oleophobicity. *Advanced Materials* **2009,** *21*, 2190-2195.

(68) Sun, T.; Wang, G.; Feng, L.; Liu, B.; Ma, Y.; Jiang, L.; Zhu, D. Reversible switching between superhydrophilicity and superhydrophobicity. *Angewandte Chemie* **2004,** *116*, 361-364.

(69) Cheng, M.; Liu, Q.; Ju, G.; Zhang, Y.; Jiang, L.; Shi, F. Bell-Shaped Superhydrophilic–Superhydrophobic–Superhydrophilic Double Transformation on a pH-Responsive Smart Surface. *Advanced Materials* **2014,** *26*, 306-310.

(70) Minko, S.; Müller, M.; Motornov, M.; Nitschke, M.; Grundke, K.; Stamm, M. Two-level structured self-adaptive surfaces with reversibly tunable properties. *Journal of the American Chemical Society* **2003,** *125*, 3896-3900.

(71) Yu, X.; Wang, Z.; Jiang, Y.; Shi, F.; Zhang, X. Reversible pH-Responsive Surface: From Superhydrophobicity to Superhydrophilicity. *Advanced Materials* **2005,** *17*, 1289-1293.

(72) Dorrer, C.; Ruehe, J. Wetting of silicon nanograss: from superhydrophilic to superhydrophobic surfaces. *Advanced Materials* **2008,** *20*, 159-163.

(73) Kietzig, A.-M.; Hatzikiriakos, S. G.; Englezos, P. Patterned superhydrophobic metallic surfaces. *Langmuir* **2009,** *25*, 4821-4827.

(74) Aria, A. I.; Gharib, M. Reversible tuning of the wettability of carbon nanotube arrays: the effect of ultraviolet/ozone and vacuum pyrolysis treatments. *Langmuir* **2011,** *27*, 9005-9011.

(75) Huang, L.; Lau, S.; Yang, H.; Leong, E.; Yu, S.; Prawer, S. Stable superhydrophobic surface via carbon nanotubes coated with a ZnO thin film. *The Journal of Physical Chemistry B* **2005,** *109*, 7746-7748.

(76) Lim, H. S.; Kwak, D.; Lee, D. Y.; Lee, S. G.; Cho, K. UV-driven reversible switching of a roselike vanadium oxide film between superhydrophobicity and superhydrophilicity. *Journal of the American Chemical Society* **2007,** *129*, 4128-4129.

(77) Oliveira, N. M.; Neto, A. I.; Song, W.; Mano, J. F. Two-dimensional open microfluidic devices by tuning the wettability on patterned superhydrophobic polymeric surface. *Applied physics express* **2010,** *3*, 085205.

(78) Song, Y.-Y.; Schmidt-Stein, F.; Bauer, S.; Schmuki, P. Amphiphilic TiO2 nanotube arrays: an actively controllable drug delivery system. *Journal of the American Chemical Society* **2009,** *131*, 4230-4232.

(79) Meng, X.; Zhao, D.; Zhang, J.; Shen, D.; Lu, Y.; Dong, L.; Xiao, Z.; Liu, Y.; Fan, X. Wettability conversion on ZnO nanowire arrays surface modified by oxygen plasma treatment and annealing. *Chemical Physics Letters* **2005,** *413*, 450-453.

(80) Song, W.; Veiga, D. D.; Custódio, C. A.; Mano, J. F. Bioinspired degradable substrates with extreme wettability properties. *Advanced Materials* **2009,** *21*, 1830-1834.

(81) Kakade, B.; Mehta, R.; Durge, A.; Kulkarni, S.; Pillai, V. Electric field induced, superhydrophobic to superhydrophilic switching in multiwalled carbon nanotube papers. *Nano letters* **2008,** *8*, 2693-2696.

(82) Krupenkin, T. N.; Taylor, J. A.; Wang, E. N.; Kolodner, P.; Hodes, M.; Salamon, T. R. Reversible wetting-dewetting transitions on electrically tunable superhydrophobic nanostructured surfaces. *Langmuir* **2007,** *23*, 9128-9133.

(83) Lahann, J.; Mitragotri, S.; Tran, T.-N.; Kaido, H.; Sundaram, J.; Choi, I. S.; Hoffer, S.; Somorjai, G. A.; Langer, R. A reversibly switching surface. *Science* **2003,** *299*, 371-374.

(84) Verplanck, N.; Coffinier, Y.; Thomy, V.; Boukherroub, R. Wettability switching techniques on superhydrophobic surfaces. *Nanoscale Research Letters* **2007,** *2*, 577.

(85) Xia, F.; Jiang, L. Bio-inspired, smart, multiscale interfacial materials. *Advanced materials* **2008,** *20*, 2842-2858.

(86) Heikenfeld, J.; Dhindsa, M. Electrowetting on superhydrophobic surfaces: present status and prospects. *Journal of Adhesion Science and Technology* **2008,** *22*, 319-334.

(87) Ahuja, A.; Taylor, J.; Lifton, V.; Sidorenko, A.; Salamon, T.; Lobaton, E.; Kolodner, P.; Krupenkin, T. Nanonails: A simple geometrical approach to electrically tunable superlyophobic surfaces. *Langmuir* **2008,** *24*, 9-14.

(88) Wen, L.; Tian, Y.; Jiang, L. Bioinspired Super-Wettability from Fundamental Research to Practical Applications. *Angewandte Chemie International Edition* **2015,** *54*, 3387-3399.

(89) Dorrer, C.; Rühe, J. r. Mimicking the Stenocara Beetle‧ Dewetting of Drops from a Patterned Superhydrophobic Surface. *Langmuir* **2008,** *24*, 6154-6158.

(90) Garrod, R.; Harris, L.; Schofield, W.; McGettrick, J.; Ward, L.; Teare, D.; Badyal, J. Mimicking a stenocara beetle's back for microcondensation using plasmachemical patterned superhydrophobic-superhydrophilic surfaces. *Langmuir* **2007,** *23*, 689-693.

(91) Zhai, L.; Berg, M. C.; Cebeci, F. C.; Kim, Y.; Milwid, J. M.; Rubner, M. F.; Cohen, R. E. Patterned superhydrophobic surfaces: toward a synthetic mimic of the Namib Desert beetle. *Nano Letters* **2006,** *6*, 1213-1217.

(92) Nakata, K.; Nishimoto, S.; Yuda, Y.; Ochiai, T.; Murakami, T.; Fujishima, A. Rewritable Superhydrophilic− Superhydrophobic Patterns on a Sintered Titanium Dioxide Substrate. *Langmuir* **2010,** *26*, 11628-11630.

(93) Nishimoto, S.; Kubo, A.; Nohara, K.; Zhang, X.; Taneichi, N.; Okui, T.; Liu, Z.; Nakata, K.; Sakai, H.; Murakami, T.; Abe, M.; Komine, T.; Fujishima, A. TiO2-based superhydrophobic–

superhydrophilic patterns: Fabrication via an ink-jet technique and application in offset printing. *Applied Surface Science* **2009,** *255*, 6221-6225, DOI: http://dx.doi.org/10.1016/j.apsusc.2009.01.084.

(94) Kobaku, S. P.; Kota, A. K.; Lee, D. H.; Mabry, J. M.; Tuteja, A. Patterned Superomniphobic–Superomniphilic Surfaces: Templates for Site-Selective Self-Assembly. *Angewandte Chemie International Edition* **2012,** *51*, 10109-10113.

(95) Crick, C. R.; Gibbins, J. A.; Parkin, I. P. Superhydrophobic polymer-coated copper-mesh; membranes for highly efficient oil–water separation. *Journal of Materials Chemistry A* **2013,** *1*, 5943-5948.

(96) Feng, L.; Zhang, Z.; Mai, Z.; Ma, Y.; Liu, B.; Jiang, L.; Zhu, D. A super-hydrophobic and super-oleophilic coating mesh film for the separation of oil and water. *Angewandte Chemie International Edition* **2004,** *43*, 2012-2014.

(97) Jiang, G.; Hu, R.; Xi, X.; Wang, X.; Wang, R. Facile preparation of superhydrophobic and superoleophilic sponge for fast removal of oils from water surface. *Journal of Materials Research* **2013,** *28*, 651-656.

(98) Tian, D.; Song, Y.; Jiang, L. Patterning of controllable surface wettability for printing techniques. *Chemical Society Reviews* **2013,** *42*, 5184-5209.

(99) Wang, B.; Liang, W.; Guo, Z.; Liu, W. Biomimetic super-lyophobic and super-lyophilic materials applied for oil/water separation: a new strategy beyond nature. *Chemical Society Reviews* **2015,** *44*, 336-361.

(100) Xue, Z.; Wang, S.; Lin, L.; Chen, L.; Liu, M.; Feng, L.; Jiang, L. A novel superhydrophilic and underwater superoleophobic hydrogel-coated mesh for oil/water separation. *Advanced Materials* **2011,** *23*, 4270-4273.

(101) Zhang, J.; Seeger, S. Polyester materials with superwetting silicone nanofilaments for oil/water separation and selective oil absorption. *Advanced Functional Materials* **2011,** *21*, 4699-4704.

(102) Ghosh, S.; Lagraauw, R.; Otten, S.; Pit, A.; Berendsen, C.; Zeegers, J.; van den Ende, D.; Mugele, F. Trapping of drops by wetting defects. *Nature communications* **2014,** *5*.

(103) Kwon, G.; Kota, A.; Li, Y.; Sohani, A.; Mabry, J. M.; Tuteja, A. On-Demand Separation of Oil-Water Mixtures. *Advanced Materials* **2012,** *24*, 3666-3671.

(104) McHale, G.; Herbertson, D.; Elliott, S.; Shirtcliffe, N.; Newton, M. Electrowetting of nonwetting liquids and liquid marbles. *Langmuir* **2007,** *23*, 918-924.

(105) Ishii, D.; Shimomura, M. Invisible gates for moving water droplets: adhesive force gradients on a biomimetic superhydrophobic surface. *Chemistry of Materials* **2013,** *25*, 509-513.

(106) Ju, J.; Zheng, Y.; Jiang, L. Bioinspired one-dimensional materials for directional liquid transport. *Accounts of chemical research* **2014,** *47*, 2342-2352.

(107) McHale, G.; Elliott, S. J.; Newton, M. I.; Shirtcliffe, N. J. Superhydrophobicity: Localized parameters and gradient surfaces. *Contact Angle, Wettability and Adhesion', Koninklijke Brill NV* **2009,** *6*, 219-233.

(108) McHale, G.; Shirtcliffe, N. J.; Newton, M. I. Super-hydrophobic and super-wetting surfaces: Analytical potential? *Analyst* **2004,** *129*, 284-287, DOI: 10.1039/B400567H.

(109) Nilsson, M. A.; Rothstein, J. P. Using sharp transitions in contact angle hysteresis to move, deflect, and sort droplets on a superhydrophobic surface. *Physics of Fluids* **2012,** *24*, 062001, DOI: doi:http://dx.doi.org/10.1063/1.4723866.

(110) Reyssat, M.; Pardo, F.; Quéré, D. Drops onto gradients of texture. *EPL (Europhysics Letters)* **2009,** *87*, 36003.

(111) Shastry, A.; Case, M. J.; Böhringer, K. F. Directing droplets using microstructured surfaces. *Langmuir* **2006,** *22*, 6161-6167.

(112) Sakai, N.; Fujishima, A.; Watanabe, T.; Hashimoto, K. Quantitative evaluation of the photoinduced hydrophilic conversion properties of TiO2 thin film surfaces by the reciprocal of contact angle. *The Journal of Physical Chemistry B* **2003,** *107*, 1028-1035.

(113) Yang, J.-T.; Chen, J. C.; Huang, K.-J.; Yeh, J. A. Droplet manipulation on a hydrophobic textured surface with roughened patterns. *Journal of microelectromechanical systems* **2006,** *15*, 697-707.

(114) Wang, Q.; Su, B.; Liu, H.; Jiang, L. Chinese brushes: Controllable liquid transfer in ratchet conical hairs. *Advanced Materials* **2014,** *26*, 4889-4894.

(115) Liu, M.; Zheng, Y.; Zhai, J.; Jiang, L. Bioinspired super-antiwetting interfaces with special liquid− solid adhesion. *Accounts of chemical research* **2009,** *43*, 368-377.

(116) Lai, Y.; Gao, X.; Zhuang, H.; Huang, J.; Lin, C.; Jiang, L. Designing superhydrophobic porous nanostructures with tunable water adhesion. *Advanced Materials* **2009,** *21*, 3799-3803.

(117) Dawood, M.; Zheng, H.; Liew, T.; Leong, K.; Foo, Y.; Rajagopalan, R.; Khan, S.; Choi, W. Mimicking both petal and lotus effects on a single silicon substrate by tuning the wettability of nanostructured surfaces. *Langmuir* **2011,** *27*, 4126-4133.

(118) Yong, J.; Chen, F.; Yang, Q.; Zhang, D.; Bian, H.; Du, G.; Si, J.; Meng, X.; Hou, X. Controllable adhesive superhydrophobic surfaces based on PDMS microwell arrays. *Langmuir* **2013,** *29*, 3274-3279.

(119) Tang, P.; Zhang, W.; Wang, Y.; Zhang, B.; Wang, H.; Lin, C.; Zhang, L. Effect of superhydrophobic surface of titanium on staphylococcus aureus adhesion. *Journal of Nanomaterials* **2011,** *2011*, 2.

(120) Ballester-Beltrán, J.; Rico, P.; Moratal, D.; Song, W.; Mano, J. F.; Salmerón-Sánchez, M. Role of superhydrophobicity in the biological activity of fibronectin at the cell–material interface. *Soft Matter* **2011,** *7*, 10803-10811.

(121) Shiu, J. Y.; Chen, P. Addressable protein patterning via switchable superhydrophobic microarrays. *Advanced Functional Materials* **2007,** *17*, 2680-2686.

(122) Li, C.; Ye, W.; Jin, J.; Xu, X.; Liu, J.; Yin, J. Immobilization of nattokinase-loaded red blood cells on the surface of superhydrophobic polypropylene targeting fibrinolytic performance. *J. Mater. Chem. B* **2015,** *3*, 3922-3926.

CHAPTER 3 – TUNABLE SUPEROMNIPHOBIC SURFACES FOR SORTING

DROPLETS BY SURFACE TENSION

Summary: We utilized tunable superomniphobic surfaces with flower-like TiO_2 nanostructures to fabricate a simple device with precisely tailored surface energy domains that, for the first time, can sort droplets by surface tension (**published in Lab on a Chip, 2016**). We envision that our methodology for droplet sorting will enable inexpensive and energy-efficient analytical devices for personalized point-of-care diagnostic platforms, lab-on-a-chip systems, biochemical assays and biosensors.

3.1. Introduction

Recent years have witnessed a significant spike in manipulation of liquid droplets because of their applications in microfluidic diagnostics,[1-2] DNA analysis,[3-4] drug discovery,[5] microreactors[6-7] and biosensing.[8] Particularly, droplet manipulation on super-repellent surfaces[9-10] has been widely studied because droplets exhibit high mobility, minimal contamination and minimal sample loss on such surfaces. Various droplet manipulation methods including electric fields,[11-14] magnetic fields,[15-17] guiding tracks,[18-20] and wettability gradients,[21-26] have been developed to enable the transportation, trapping, merging and splitting of droplets on super-repellent surfaces. However, there are very few studies[21, 25] that demonstrate droplet sorting (i.e., systematically ordering or categorizing droplets by a physical property of the droplet) on super-repellent surfaces.

As described in chapter two, super-repellent surfaces can be broadly classified as superhydrophobic surfaces and superomniphobic surfaces.[27-30] The few studies[21, 25] that demonstrated droplet sorting have employed superhydrophobic surfaces to sort water droplets based on the droplet size. However, to the best of our knowledge, there are no studies that

employ super-repellent surfaces to sort droplets based on surface tension. Since superhydrophobic surfaces cannot repel low surface tension liquids, superomniphobic surfaces are necessary for sorting droplets by surface tension over a wide range (i.e., both high and low surface tension liquids).

In this work, we synthesized tunable superomniphobic surfaces with fluorinated, flower-like TiO_2 nanostructures. We demonstrated that the surface chemistry, and consequently the solid surface energy and contact angle hysteresis, of our superomniphobic surfaces can be tuned using UV irradiation. This allowed us to systematically tune the mobility of droplets with different surface tensions on our superomniphobic surfaces. Each of these surfaces with same surface texture, but different solid surface energy allowed certain high surface tension liquid droplets to freely roll past the surface while "trapping" other low surface tension liquid droplets due to adhesion. Leveraging this selective mobility of droplets based on their surface tension, we fabricated a simple device with precisely tailored discrete surface energy domains that, for the first time, can sort droplets by their surface tension. The novelty of our work lies in the design of discrete and tunable superomniphobic domains as well as the ability of the device to sort droplets by surface tension.

Droplet sorting occurs on our device due to a balance between the work done by gravity and the work expended due to adhesion (that depends on liquid surface tension), without the need for any external energy input. Our devices can be fabricated easily in a short time and we demonstrated that each device can be reused multiple times (up to 25 times in our experiments) to sort droplets by surface tension over a wide range (28.7 mN m^{-1} to 72.1 mN m^{-1}). Further, our devices can be readily used to estimate the surface tension of miscible liquid mixtures that in turn enables the estimation of mixture composition. This is particularly useful for in-the field and on-

the-go operations, where complex analysis equipment is unavailable. We envision that our methodology for droplet sorting will enable inexpensive and energy efficient analytical devices for personalized point-of-care diagnostic platforms, lab-on-a-chip systems, biochemical assays and biosensors.

3.2. Design Principles

As described in Chapter two, superhydrophobic and superomniphobic surfaces are fabricated by combining low solid surface energy (typically $\gamma_{sv} < 15$ mN m^{-1}) materials and textured surfaces.[31-35] Although superhydrophobic surfaces can be fabricated with a wide variety of textures, fabrication of superomniphobic surfaces requires a re-entrant texture (i.e., multivalued surface topography).[11, 31-35]

Liquid droplets roll off easily from super-repellent surfaces because of the low $\Delta\theta^*$. Based on a balance between work done by gravity (left side of equation 3-1) and work expended due to adhesion (right side of equation 3-1), the roll off angle on a super-repellent surface is given as:[31, 36]

$$\rho g V \sin\omega \approx \gamma_{lv} D_{TCL} \left(\cos\theta_{rec}^* - \cos\theta_{adv}^* \right) \tag{3-1}$$

Here, θ_{adv}^* and θ_{rec}^* are the apparent advancing and receding contact angles, respectively, ρ is the density of the liquid, g is acceleration due to gravity, and V is the volume of the liquid droplet. D_{TCL} is the width of solid–liquid–vapor contact line perpendicular to the rolling direction. When the shape of the droplet does not deviate significantly from a spherical cap, the width of the triple phase contact line can be computed as:[37]

$$D_{TCL} = 2.\cos\left(\bar{\theta}^* - \frac{\pi}{2}\right) \cdot \left[\frac{3V}{\pi\left(2 - 3\cos\bar{\theta}^* + \cos^3\bar{\theta}^*\right)}\right]^{\frac{1}{3}} \qquad (3\text{-}2)$$

Here, $\bar{\theta}^*$ is the average apparent contact angle, given as:

$$\cos\bar{\theta}^* = \frac{\cos\theta_{adv}^* + \cos\theta_{rec}^*}{2} \qquad (3\text{-}3)$$

When a liquid droplet with roll off angle ω is placed on a super-repellent surface tilted relative to the horizontal at a tilt angle α, the liquid droplet will roll off from the surface when ω < α and the liquid droplet will remain adhered (i.e., not roll off and stick) to the surface when ω > α.

Consider droplets with different surface tension, but the same volume. Typically, in systems with no specific solid–liquid interactions, liquids with lower γ_{lv} adhere more to a super-repellent surface (i.e., display higher ω) and liquids with higher γ_{lv} adhere less (i.e., display lower ω). This is because of the higher D_{TCL} and higher $\Delta\theta^*$ associated with low γ_{lv} liquids.[38] So, when a super-repellent surface with solid surface energy γ_{sv} is tilted at an appropriate tilt angle α, it may be anticipated that certain higher surface tension liquid droplets with ω < α will roll off from the surface while other lower surface tension liquid droplets with ω > α will remain adhered to the surface. Similarly, when a super-repellent surface with identical texture, but a slightly different solid surface energy is tilted at the same tilt angle α, it may be anticipated that a different set of higher surface tension liquid droplets with ω' < α will roll off from the surface and another set of lower surface tension liquid droplets with ω' > α will remain adhered to the surface. If γ_{sv} < γ_{sv}' then ω < ω', i.e., at a fixed tilt angle α, the super-repellent surface with lower solid surface

energy will allow more liquids with lower surface tension to roll off from the surface compared to the one with higher solid surface energy. In this manner, different super-repellent surfaces with identical texture can be used to sort droplets into different sets – one set of higher surface tension liquids that freely roll past the surface and another set of lower surface tension liquids that are trapped on the surface and so on. If the super-repellent surfaces are superhydrophobic, they can be used to sort only a narrow range of high γ_{lv} liquids. On the other hand, if the super-repellent surfaces are superomniphobic, they can be used to sort a wide range of liquids with both high γ_{lv} and low γ_{lv}. Utilizing the principles discussed thus far, we fabricated a simple device with multiple precisely tailored γ_{sv} domains of tunable superomniphobic surfaces to sort liquid droplets by their surface tension.

3.3. Fabrication and Characterization of Superomniphobic Surfaces

We synthesized our superomniphobic surfaces via hydrothermal synthesis of titanium dioxide (TiO₂) nanostructures[39] and subsequent surface modification with a fluorinated silane. For hydrothermal synthesis of superomniphobic surfaces, titanium (Ti) sheets (Titanium Joe Inc.; 6 cm long × 2 cm wide × 0.8 mm thick) were cleaned by sonication in acetone and isopropanol, dried with nitrogen and placed in a PTFE-lined stainless-steel autoclave containing 20 mM hydrofluoric acid (47% Alfa Aesar). The autoclave was sealed and the Ti sheets were etched under hydrothermal conditions at 100 °C for different times. After hydrothermal synthesis, the samples were rinsed thoroughly with deionized water, dried with nitrogen, and the surface was modified via vapor phase silanization at 120 °C for 1 hour using 200 μL of heptadecafluoro-1,1,2,2-tetrahydrodecyl trichlorosilane (Figure 3.1a). In order to determine the surface morphology, the surfaces were imaged using SEM (JEOL JSM-6500F) at 15 kV. Also, the contact angles and roll off angles were measured using a contact angle goniometer (Ramé-Hart

200-F1). The contact angles were measured by advancing or receding 5 ± 0.5 μL droplets on the surface using a micrometer syringe (Gilmont). The roll off angles were measured by tilting the stage until the 5 ± 0.5 μL droplet rolled off from the surface. At least six measurements were performed on each surface. The errors in contact angle and roll off angle were $\pm1°$ and $\pm0.5°$, respectively.
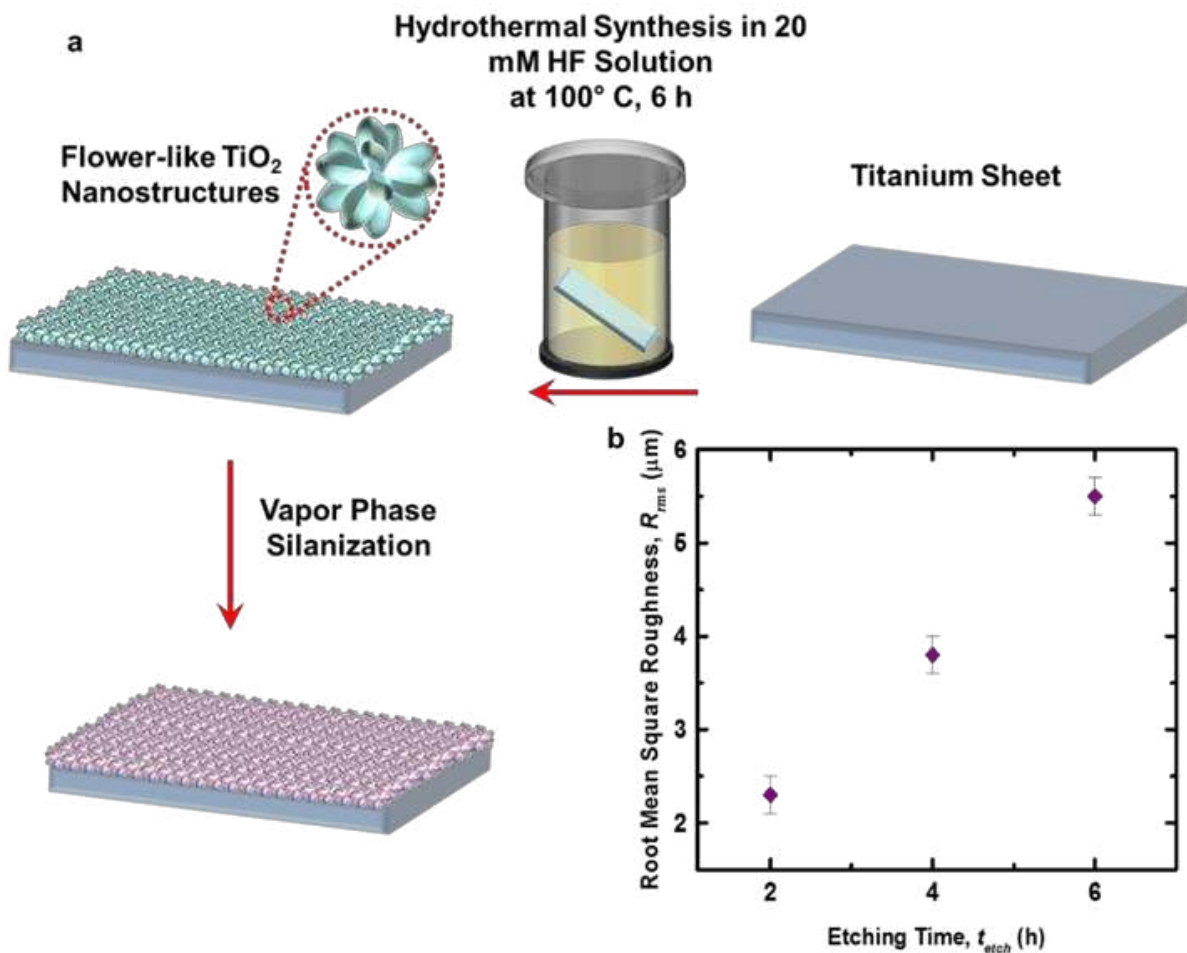
Figure 3.1. a) Schematic depicting the fabrication of the superomniphobic surfaces with fluorinated flower-like TiO$_2$ nanostructures. b) The root mean square roughness of the surfaces at different etching times.

The etching time t_{etch} in hydrothermal synthesis allowed us to tailor the morphology of the TiO$_2$ nanostructures and obtain the required re-entrant texture. As the etching time t_{etch} increased, more TiO$_2$ nanostructures formed and consequently the roughness R_{rms} of the surface increased

(Figure 3.1b). Significant differences were observed between the root mean square roughness of the surfaces at different etching times ($p \leq 0.05$ at $\alpha=0.05$). The root mean square roughness R_{rms} of the surfaces was measured using an optical profilometer (Zygo Zescope).
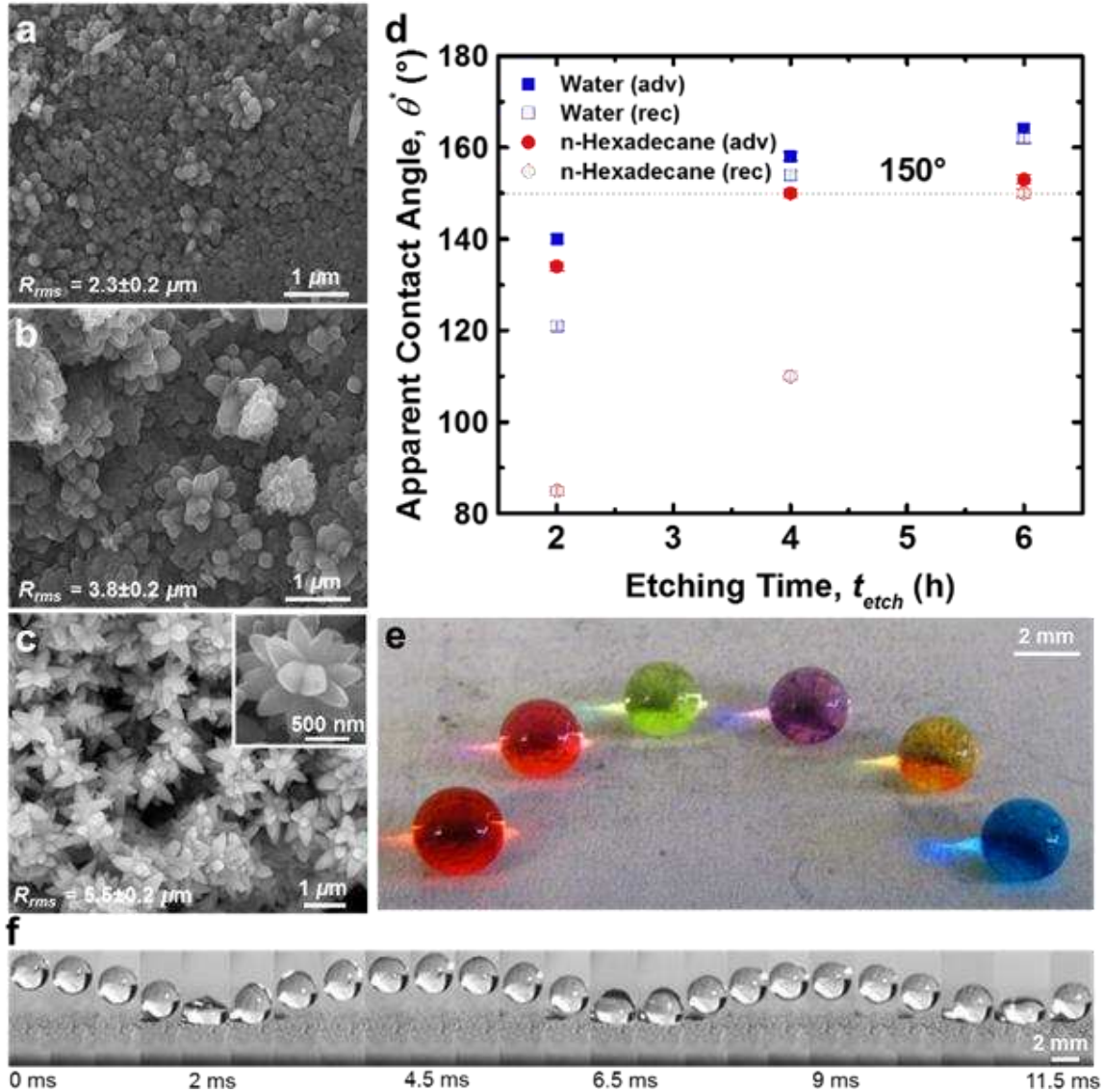
Figure 3.2. a), b) and c) SEM images showing the morphology of TiO$_2$ nanostructures after 2, 4 and 6 hours, respectively, of etching under hydrothermal conditions. The root mean square roughness R_{rms} increased with etching time. The inset in (c) shows the re-entrant texture of the flower-like TiO$_2$ nanostructure. d) Apparent contact angles of water and n-hexadecane on the surfaces shown in (a)–(c) after the surfaces are fluorinated. e) Droplets (left to right) of n-hexadecane, water + 60% ethanol, water + 30% ethanol, water + 20% ethanol, water + 10% ethanol, and water showing very high apparent contact angles on the superomniphobic TiO$_2$ surface. f) A series of snapshots showing a droplet of water + 60% ethanol bouncing on the superomniphobic TiO$_2$ surface.

Low etching time (t_{etch} = 2 h) resulted in bead-like TiO$_2$ nanostructures (Figure 3.2a). After this surface was fluorinated, it displayed relatively low contact angles and high contact angle hysteresis (Figure 3.2d) with water (γ_{lv} = 72.1 mN m^{-1}; a representative high γ_{lv} liquid) and n-hexadecane (γ_{lv} = 27.5 mN m^{-1}; a representative low γ_{lv} liquid) indicating that the surface roughness is unsuitable to render it super-repellent. On this surface, both water and n-hexadecane are primarily in the Wenzel state. Slightly higher etching time (t_{etch} = 4 h) resulted in predominantly bead-like TiO$_2$ nanostructures along with a few flower-like TiO$_2$ nanostructures (Figure 3.2b). After this surface was fluorinated, it displayed very high contact angles and very low contact angle hysteresis with water (Figure 3.2d) indicating that it is superhydrophobic. However, the surface displayed relatively lower contact angles and higher contact angle hysteresis with n-hexadecane indicating that it is not superoleophobic. This is because of insufficient re-entrant textured nanostructures on the surface. On this surface, water is in the Cassie–Baxter state and n-hexadecane is primarily in the Wenzel state.

Sufficiently high etching time ($t_{etch} \geq$ 6 h) resulted in flower-like TiO$_2$ nanostructures (Figure 3.2c). After this surface was fluorinated, it displayed very high contact angles and very low contact angle hysteresis with water and n-hexadecane (Figure 3.2d) indicating that it is both superhydrophobic and superoleophobic, i.e., superomniphobic. Further, significant differences were observed between the average receding contact angles for n-hexadecane at different etching times ($p \leq 0.05$ at α=0.05). The re-entrant texture of the flower-like TiO$_2$ nanostructures coupled with the low solid surface energy (γ_{sv} = 10 mN m^{-1}) imparted by the fluorinated groups rendered our surfaces superomniphobic. On this surface, both water and n-hexadecane are in the Cassie–Baxter state. The superomniphobicity is further evident from a wide range of liquids

beading up (Figure 3.2e) and bouncing (Figure 3.2f) on the surface due to their high contact angles and low contact angle hysteresis. The apparent advancing and the apparent receding contact angles of different liquids on superomniphobic surfaces are listed in Table 3.1.

Table 3.1. The apparent advancing and the apparent receding contact angles of different liquids on superomniphobic surfaces before UV irradiation.

Liquid	Surface tension (mN m^{-1})	θ^*_{adv}	θ^*_{rec}
Water	72.1	164°	162°
Water + 10% Ethanol	53.4	161°	159°
Water + 20% Ethanol	43.7	159°	155°
Water + 30% Ethanol	37.2	156°	153°
Water + 60% Ethanol	28.7	154°	150°
n-hexadecane	27.5	153°	150°

3.4. Tuning the Surface Wettability of Superomniphobic Surfaces

We chose to synthesize our superomniphobic surfaces with TiO_2 because the photocatalytic activity of TiO_2 would allow us to precisely tune the surface chemistry, and consequently the solid surface energy, via UV irradiation. The surface chemistry, and consequently the solid surface energy, of the superomniphobic surfaces with flower-like TiO_2 nanostructures was tuned by UV irradiating the surface for different times using a 254 nm UV bench lamp (UVP XX-40S). The samples were placed approximately 2 cm away from the UV lamp.
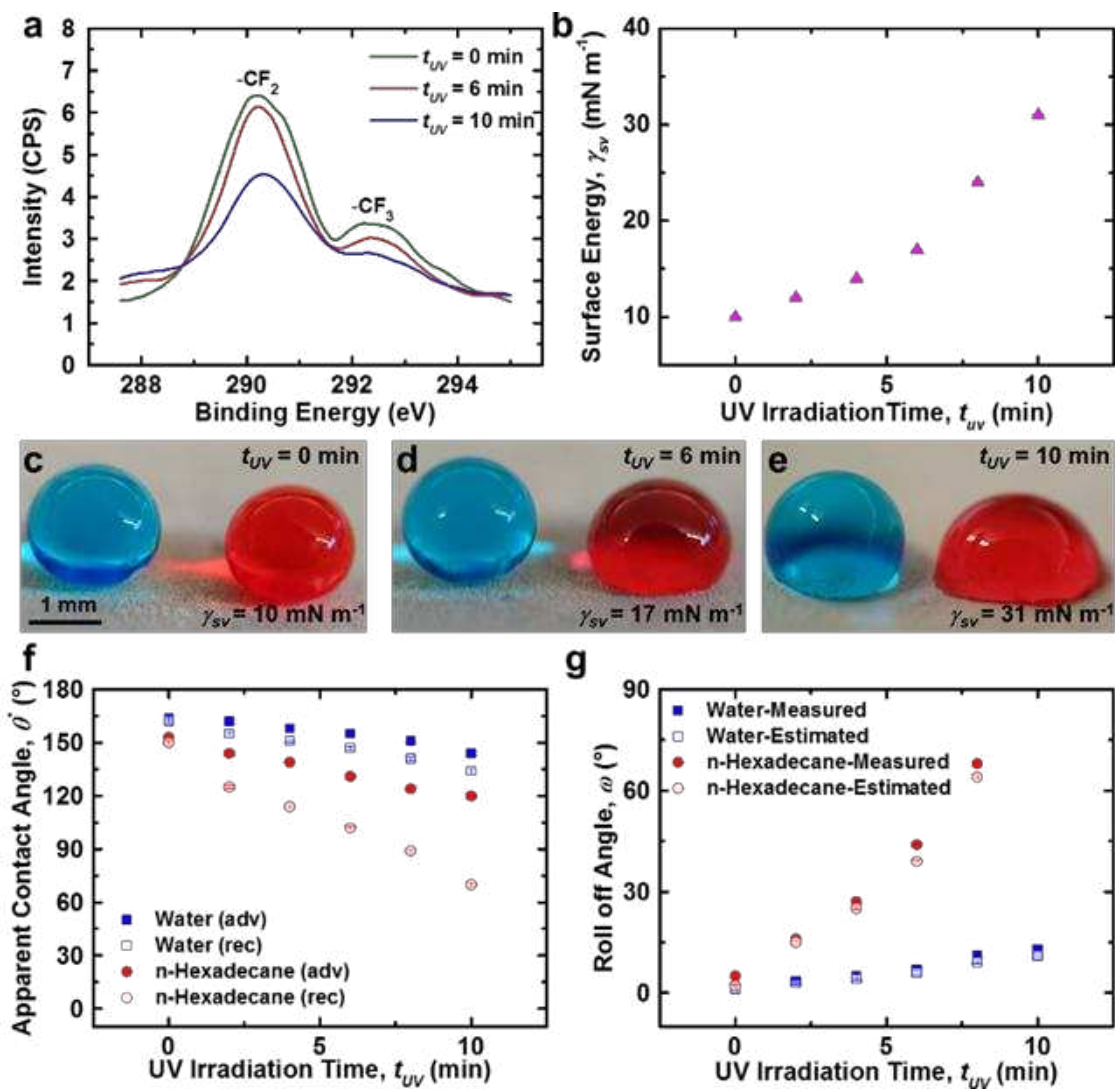
Figure 3.3. a) High resolution C1s X-ray photo-electron spectroscopy (XPS) scan showing the degradation of –CF_2 and –CF_3 groups with increasing UV irradiation time t_{UV}. b) The solid surface energy of fluorinated TiO_2 surfaces increasing with increasing UV irradiation time. c), d) and e) The wettability of water (blue) and *n*-hexadecane (red) droplets on fluorinated TiO_2 surfaces increasing with increasing UV irradiation time. f) Apparent contact angles of water and *n*-hexadecane on fluorinated TiO_2 surfaces decreasing with increasing UV irradiation time. g) The measured roll off angles of ∼5 μL *n*-hexadecane droplets on fluorinated TiO_2 surfaces increasing more rapidly compared to those of ∼5 μL water droplets with increasing UV irradiation time. The measured roll off angles are in good agreement with the estimated roll off angles. Significant differences were observed between the average receding contact angles for n-hexadecane at different UV irradiation times t_{UV} ($p \le 0.05$ at $\alpha=0.05$).

Under UV irradiation, electron–hole pairs are generated on the surface of TiO_2, which in turn produce radical species such as OH and O_2^{-}.[40] These radical species gradually degrade organic compounds such as the fluorinated groups on our superomniphobic surfaces.[41-42] The

degradation of $-CF_2$ and $-CF_3$ groups is evident from the high resolution C1s X-ray photo-electron spectroscopy (XPS) scan (Figure 3.3a). XPS analysis was conducted on the surfaces before and after UV irradiation using a PHI-5800 spectrometer (Physical Electronics) to verify the degradation of the fluorinated groups ($-CF_2$ and $-CF_3$) upon UV irradiation. As a result, with increasing UV irradiation time t_{UV}, the solid surface energy of our superomniphobic surfaces increased (Figure 3.3b). Further, significant differences were observed between the solid surface energy of our superomniphobic surfaces at different UV irradiation times t_{UV} ($p \leq 0.05$ at α=0.05).

In order to determine the solid surface energy, non-textured, uniform, thin films of TiO_2 (150 nm thick) were deposited on piranha cleaned glass substrates via RF ion beam sputtering with ion beam assist using a Ti target under 130 µTorr of oxygen in argon. Subsequently, the non-textured TiO_2 surfaces were modified via vapor phase silanization at 120 °C for 1 hour using 200 µL of heptadecafluoro-1,1,2,2- tetrahydrodecyl trichlorosilane. The advancing contact angles measured at different UV irradiation times on fluorinated, non-textured TiO_2 surfaces were used to estimate the solid surface energy. Owens-Wendt[43] approach was used to estimate the solid surface energy γ_{sv} of the fluorinated TiO_2 surfaces before and after UV irradiation. n-hexadecane (γ_{lv} = 27.5 mN m^{-1}) was used as the non-polar liquid to estimate the dispersive component of the solid surface energy γ_{sv}^d and water (γ_{lv}^d = 21.1 mN m^{-1} and γ_{lv}^p = 51.0 mN m^{-1}) was used as the polar liquid to estimate the polar component of the solid surface energy γ_{sv}^p. Assuming the advancing contact angle is approximately equal to Young's contact angle,[31, 33-34, 44-46] the advancing contact angles θ_{adv} measured at different UV irradiation times t_{UV} on fluorinated, non-textured TiO_2 surfaces were used to estimate the solid surface energy (Table 3.2). The error in

solid surface energy was ±0.5 mN m^{-1}. Correspondingly, the apparent contact angles decreased and the contact angle hysteresis increased for both water and n-hexadecane (Figures 3.3c–3.3f).

Table 3.2. Advancing contact angles of water and n-hexadecane and solid surface energies, at different UV irradiation times, for fluorinated, non-textured TiO$_2$ surfaces.

t_{UV} (min)	θ_{adv}		γ_{sv} (mN m^{-1})
	n-hexadecane	Water	
0	80°	120°	10
2	77°	108°	12
4	73°	104°	14
6	69°	97°	17
8	62°	85°	24
10	56°	74°	31

Here, it is important to note that the apparent receding contact angle decreased, and the contact angle hysteresis increased more rapidly for n-hexadecane (lower γ_{lv} liquid) compared to water (higher γ_{lv} liquid). Consequently, the roll off angles increased more rapidly for n-hexadecane compared to water with increasing t_{UV} (Figure 3.3g). The influence of t_{UV} on γ_{sv} and consequently on the apparent advancing and receding contact angles θ^*_{adv} and θ^*_{rec}, and roll off angles ω of water and n-hexadecane on our superomniphobic TiO$_2$ surfaces is shown in Table 3.3. The estimated roll off angles of different liquids shown in Figure 3.2g were obtained using equation 3-1.

It is evident from Table 3.3 and Figure 3.3f that θ^*_{adv} and θ^*_{rec} decrease for both n-hexadecane and water with increasing t_{UV}. Further, it is evident that θ^*_{rec} decreases (Figure 3.3f) and ω increases (Figure 3.3g) more rapidly for n-hexadecane (lower γ_{lv} liquid) compared to water (higher γ_{sv} liquid) with increasing t_{UV}. In this work, our primary interest lies in $t_{UV} \leq 10$ min

because at $t_{UV} \geq 10$ min, n-hexadecane droplets remain adhered and can no longer roll off, i.e., the mobility of n-hexadecane droplets can no longer be tuned or changed. For longer UV irradiation times (i.e., 10 min < t_{UV} < 30 min), our experiments indicate that the apparent receding contact angles of n-hexadecane continue to decrease more rapidly than water. For very long UV irradiation times (i.e., t_{UV} > 30 min), our experiments indicate that the surfaces become superomniphilic (i.e., the apparent contact angles of both water and n-hexadecane are ~0°). It is worth noting that in spite of numerous studies,[47-55] the explicit mechanisms involved in UV-induced wettability of TiO_2 surfaces (including the rate and degree of degradation of organic compounds such as fluorinated groups) are not completely established and continue to be an area of active research.

Table 3.3. The apparent advancing and receding contact angles and roll off angles of water and n-hexadecane on superomniphobic surfaces after UV irradiation.

t_{UV} (min)	γ_{sv} (mN m^{-1})	θ^*_{adv}		θ^*_{rec}		ω	
		n-hexadecane	Water	n-hexadecane	Water	n-hexadecane	Water
0	10	153°	164°	150°	162°	5°	2°
2	12	144°	162°	125°	155°	16°	3.5°
4	14	139°	158°	114°	151°	27°	5°
6	17	131°	155°	102°	147°	44°	7°
8	24	124°	151°	89°	141°	68°	11°
10	31	120°	144°	70°	134°	No roll off	13°

For example, on a superomniphobic surface before UV irradiation (t_{UV} = 0 min, γ_{sv} = 10 mN m^{-1}), the difference between the measured roll off angles of water (ω = 2°) and n-hexadecane (ω = 5°) is very small. However, on a UV irradiated surface (t_{UV} = 6 min, γ_{sv} = 17 mN m^{-1}), the difference between the measured roll off angles of water (ω = 7°) and n-hexadecane (ω = 44°) is quite significant. When this UV irradiated surface is tilted relative to the horizontal at an angle α

= 15°, the higher γ_{lv} water droplets roll off from the surface and the lower γ_{lv} n-hexadecane droplets remain adhered to the surface. In this manner, we can allow certain higher surface tension liquids to freely roll past the surface while trapping other lower surface tension liquids.

3.5. A Device to Sort Droplets by Surface Tension

While a single surface with a fixed solid surface energy is sufficient to sort liquids into two sets – one with higher surface tension liquids that freely roll past the surface and another with lower surface tension liquids that are trapped on the surface – it cannot provide a finer sorting of liquids by their surface tension. In order to sort a wide range of liquids by their surface tension, we fabricated a simple device with multiple, discrete domains with identical texture, but different precisely tailored solid surface energy. The solid surface energy of each discrete domain was tuned to the desired value by controlling the UV irradiation time while masking the other areas with a PTFE tape (Figure 3.4a). The discrete domains were fabricated along the length of the device in the order of increasing solid surface energy (Figure 3.4b). The device was tilted relative to the horizontal at an angle α with the lowest solid surface energy domain at the top of the incline and the highest solid surface energy domain at the bottom of the incline.
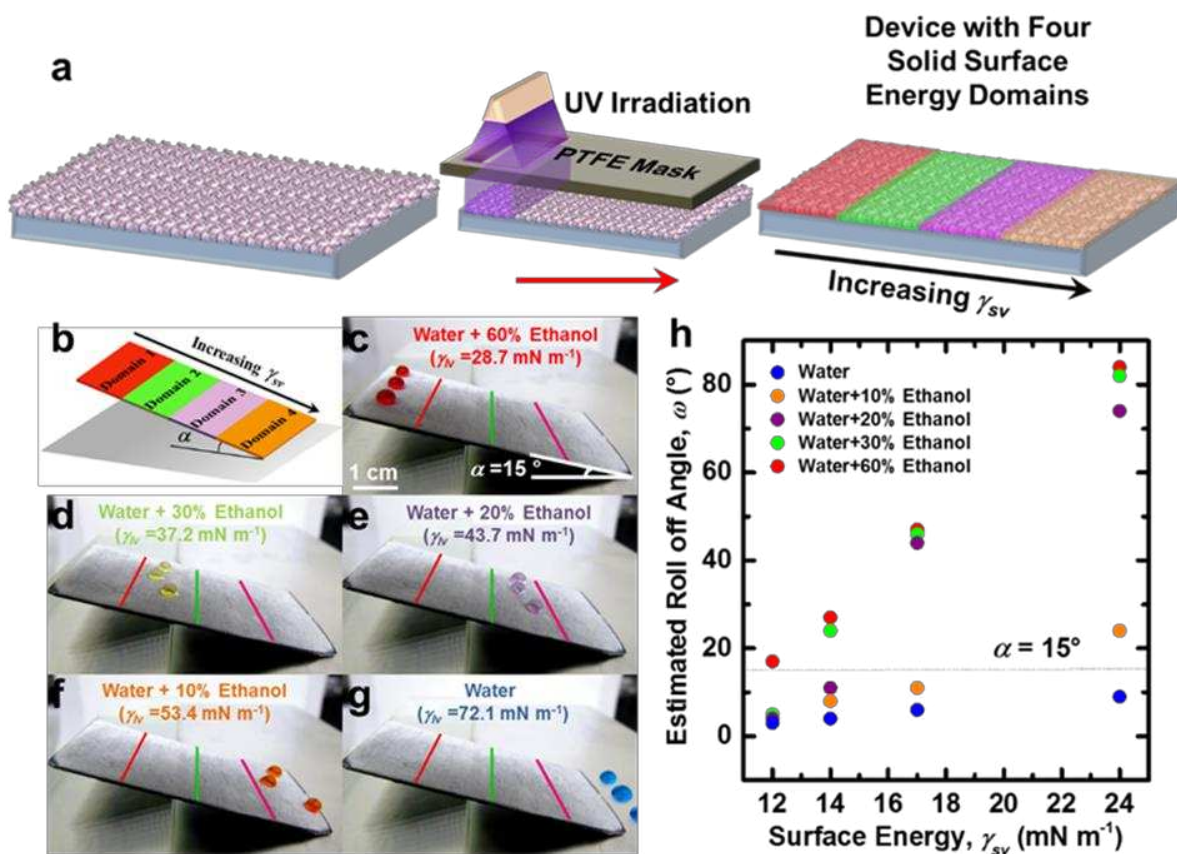
Figure 3.4. Schematic depicting the a) fabrication process of a device and b) final device with multiple, discrete domains of identical texture, but different solid surface energies. c)–g) A series of snapshots showing the sorting of ~5 μL liquid droplets with different surface tension values using a device with four discrete surface energy domains tilted at an angle of 15° relative to the horizontal. Each domain is 15 mm ± 2 mm long. h) The estimated roll off angles of 5 μL liquid droplets with different surface tension values on super-repellent surfaces with different solid surface energies.

When a liquid droplet is introduced at the top of the incline, depending on its surface tension, it will freely roll past the domains where its roll off angle $\omega < \alpha$ and it will get trapped in the first domain where its roll off angle $\omega' > \alpha$. As an example, here we demonstrate sorting of five different ~5 μL liquid droplets by their surface tension – water (γ_{lv} = 72.1 mN m^{-1}), water + 10% ethanol (γ_{lv} = 53.4 mN m^{-1}), water + 20% ethanol (γ_{lv} = 43.7 mN m^{-1}), water + 30% ethanol (γ_{lv} = 37.2 mN m^{-1}) and water + 60% ethanol (γ_{lv} = 28.7 mN m^{-1}) – using a device with four precisely tailored solid surface energy domains – domain 1 (γ_{sv} = 12 mN m^{-1}, t_{UV} = 2 min),

domain 2 (γ_{sv} = 14 mN m^{-1}, t_{UV} = 4 min), domain 3 (γ_{sv} = 17 mN m^{-1}, t_{UV} = 6 min) and

domain 4 (γ_{sv} = 24 mN m^{-1}, t_{UV} = 8 min). We used water–ethanol mixtures to demonstrate

droplet sorting because this allows us to systematically tune the surface tension of liquid droplets

over a wide range (28.7 mN m^{-1} to 72.1 mN m^{-1}).

Table 3.4. Apparent advancing and apparent receding contact angles, and the estimated roll off angles of different water-ethanol mixtures in each of the discrete domains shown in Figures 3.4c–3.4g. For each tested liquid, significant differences were observed between the roll off angles at each of the discrete domains ($p \leq 0.05$ at α=0.05).

		Water	Water +10% Ethanol	Water +20% Ethanol	Water +30% Ethanol	Water +60% Ethanol
Surface tension (mN m^{-1})		72.1	53.4	43.7	37.2	28.7
Domain 1	θ^*_{adv}	162°	158°	156°	150°	145°
(t_{UV} = 2 min;	θ^*_{rec}	155°	150°	147°	141°	121°
γ_{sv} = 12 mN m-1)	ω	3°	3°	4°	5°	17°
Domain 2	θ^*_{adv}	158°	152°	146°	141°	140°
(t_{UV} = 4 min;	θ^*_{rec}	151°	140°	132°	117°	111°
γ_{sv} = 14 mN m-1)	ω	4°	8°	11°	24°	27°
Domain 3	θ^*_{adv}	155°	143°	140°	132°	131°
(t_{UV} = 6 min;	θ^*_{rec}	147°	132°	109°	101°	95°
γ_{sv} = 17 mN m-1)	ω	6°	11°	44°	46°	47°
Domain 4	θ^*_{adv}	151°	129°	127°	126°	122°
(t_{UV} = 8 min;	θ^*_{rec}	141°	115°	95°	90°	81°
γ_{sv} = 24 mN m-1)	ω	9°	24°	74°	82°	84°

We estimated the roll off angles for 5 µL droplets of each of the five liquids in each of the

four domains by measuring the apparent contact angles and using equation 3-1. The estimated

roll off angles of different water-ethanol mixtures in each of the discrete domains of our device

are listed in Table 3.4. It is evident from Table 3.4 that all of our UV irradiated surfaces used to

fabricate the device have finite roll off angles ($\omega < 90°$) with the liquids listed. While these liquid droplets may adhere to a UV irradiated surface at low tilt angles ($\alpha < \omega$), they roll off from the UV irradiated surface at higher tilt angles ($\alpha > \omega$).

If the droplets were completely in the Wenzel state, they would remain adhered to the surface and no longer exhibit mobility (i.e., droplets would not have a finite roll off angle ω). Based on this, we conclude that the droplets on the UV irradiated surfaces used to fabricate the device (e.g., Figures 3.4c–3.4g) are primarily in the Cassie-Baxter state. Further, it is evident from Table 3.4 that the contact angle hysteresis of droplets with lower surface tension is higher than that of droplets with higher surface tension. Contact angle hysteresis primarily arises from surface roughness and heterogeneity.[56-58] It is related to the energy barriers that a liquid droplet must overcome during its movement along a solid surface, and thus characterizes the resistance to droplet movement.[56-58] Typically, the resistance to droplet movement is higher for lower surface tension liquids compared to higher surface tension liquids.[59] This is possibly because lower surface tension liquids have higher solid-liquid contact area (and longer triple phase contact line), which in turn is due to their lower contact angles. Consequently, on our tunable superomniphobic surfaces, for any given solid surface energy, the contact angle hysteresis of droplets with lower surface tension is higher than that of droplets with higher surface tension. Based on the estimated roll off angles (Figure 3.4h) which is obtained using Equation 3-1, when the device is tilted at an angle $\alpha = 15°$, droplets of water + 60% ethanol should get trapped in domain 1; droplets of water + 30% ethanol should freely roll past domain 1, but get trapped in domain 2; droplets of water + 20% ethanol should freely roll past domains 1 and 2, but get trapped in domain 3; droplets of water + 10% ethanol should freely roll past domains 1, 2 and 3, but get trapped in domain 4; and droplets of water should freely roll past all domains. These

predictions match reasonably well with the experiments (Figure 3.4c–3.4g) indicating that our devices with discrete domains of precisely tailored solid surface energy and a predetermined tilt angle (based on estimated roll off angles) can, for the first time, sort liquid droplets by their surface tension.

Our devices can be reused multiple times (up to 25 times in our experiments) after completely drying the adhered liquid droplets from a previous experiment. In order to evaluate the reusability of our devices, we first wet each discrete solid surface energy domain with an extremely low surface tension liquid (e.g., ethanol; γ_{lv} = 22.1 mN m^{-1}) that remained adhered to the surface. Then, we completely dried the liquid on the surface by heating. Subsequently, we measured the roll off angles of different liquids in each domain to verify that the surface repellence has not been altered. Our experiments indicated that the roll off angles of different liquids in each domain remained unaltered even after a few wetting/drying cycles.

To illustrate this with an example, here we present (Figure 3.5) the measured roll off angles of different liquids (water, water + 10% ethanol, water + 20% ethanol, water + 30% ethanol, and water + 60% ethanol) on one of the domains with γ_{sv} = 12 mN m^{-1} after wetting with ethanol and subsequently drying for 25 times. The functionality of the device remains un-altered up to 25 cycles. As we increase the number of cycles further, the range over which we can sort droplets by surface tension decreases. This is because the re-entrant texture of our superomniphobic surfaces starts to deteriorate with increased cycles. This in turn causes the low surface tension liquid droplets to adopt the Wenzel state (and consequently, the droplet mobility can no longer be tuned) at increasingly more locations on the surface. Here, it is worth noting that improving the mechanical durability of superomniphobic surfaces continues to be a grand challenge in the field of surface science.
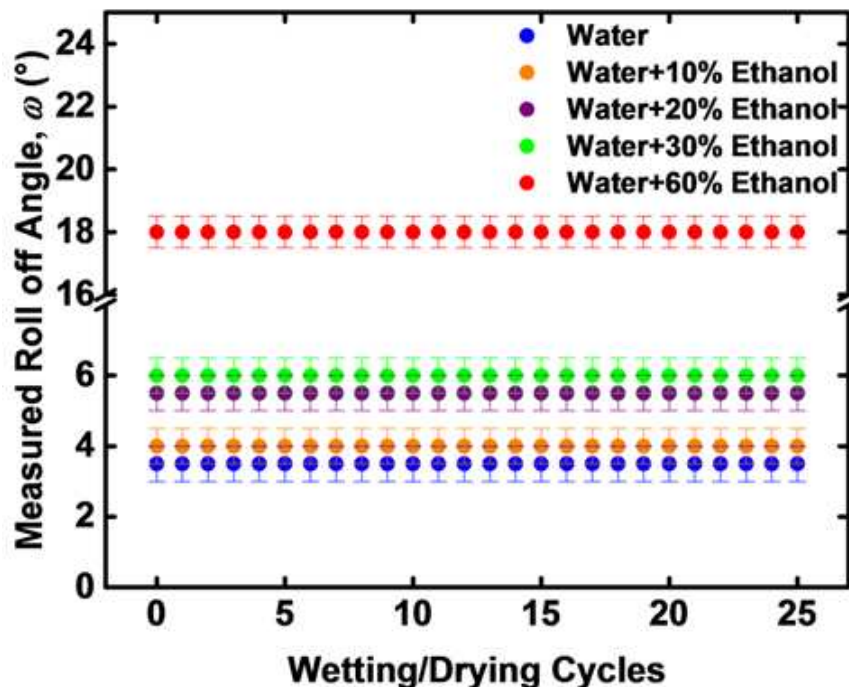
Figure 3.5. The measured roll off angles of different liquids on the domain with γ_{sv} = 12 mN m^{-1} after wetting with ethanol and subsequently drying, for 25 times. For each liquid, no statistically significant difference was observed between roll off angles at different wetting/drying cycles. Using power analysis, it is verified that the test has adequate power.

A careful inspection of sorting droplets by surface tension using our devices (Figure 3.4c– 3.4g) indicates that the droplets of the same liquid (with same surface tension) adhere at slightly different locations (typically < 10 mm from each other) within a discrete domain (with same surface energy). We attribute this to the small variation in droplet volume (±0.5 µL) that leads to different kinetic energies of the droplets as well as the small spatial variation in the surface roughness (±0.2 µm) that leads to different droplet mobility. We ensured that each discrete domain is long enough (~15 mm) so that the kinetic energy of the accelerating droplets is completely overcome by the work expended due to adhesion precisely in the first domain, where its roll off angle is higher than the tilt angle. In other words, when a liquid droplet is introduced at the top of the incline, depending on its surface tension, it will freely roll past the domains

where its roll off angle is lower than the tilt angle and it will get trapped in the first domain, where its roll off angle is higher than the tilt angle.

3.6. Conclusions

In summary, we synthesized superomniphobic surfaces with fluorinated, flower-like TiO$_2$ nanostructures. We demonstrate that the surface chemistry, and consequently the solid surface energy, of our superomniphobic surfaces can be tuned using UV irradiation. This allows us to systematically tune the mobility of droplets with different surface tensions on our superomniphobic surfaces. Leveraging the selective mobility of droplets on our superomniphobic surfaces based on their surface tensions, we fabricated a simple device with precisely tailored solid surface energy domains that, for the first time, can sort droplets by surface tension (γ_{lv} = 28.7 mN m^{-1} to 72.1 mN m^{-1}). Our devices can be fabricated easily in a short time and each device can be reused multiple times to sort droplets by surface tension. In addition, using estimated roll off angles, new devices can be systematically designed with predetermined tilt angle, number and surface energy of superomniphobic domains to sort droplets with different surface tension ranges and different droplet volumes. Our methodology and mechanism are applicable to a wide range of surface tensions and droplet volumes as long as the droplets are in the Cassie–Baxter state and not all in the Wenzel state. We envision that our methodology for droplet sorting will enable inexpensive and energy-efficient analytical devices for personalized point-of-care diagnostic platforms, lab-on-a-chip systems, biochemical assays and biosensors.

REFERENCES

(1) Teh, S.-Y.; Lin, R.; Hung, L.-H.; Lee, A. P. Droplet microfluidics. *Lab on a Chip* **2008,** *8*, 198-220.

(2) Whitesides, G. M. The origins and the future of microfluidics. *Nature* **2006,** *442*, 368-373.

(3) Kühnemund, M.; Witters, D.; Nilsson, M.; Lammertyn, J. Circle-to-circle amplification on a digital microfluidic chip for amplified single molecule detection. *Lab on a Chip* **2014,** *14*, 2983-2992.

(4) Mazutis, L.; Araghi, A. F.; Miller, O. J.; Baret, J.-C.; Frenz, L.; Janoshazi, A.; Taly, V.; Miller, B. J.; Hutchison, J. B.; Link, D. Droplet-based microfluidic systems for high-throughput single DNA molecule isothermal amplification and analysis. *Analytical chemistry* **2009,** *81*, 4813-4821.

(5) Kang, L.; Chung, B. G.; Langer, R.; Khademhosseini, A. Microfluidics for drug discovery and development: From target selection to product lifecycle management. *Drug discovery today* **2008,** *13*, 1-13.

(6) Abbyad, P.; Dangla, R.; Alexandrou, A.; Baroud, C. N. Rails and anchors: guiding and trapping droplet microreactors in two dimensions. *Lab on a Chip* **2011,** *11*, 813-821.

(7) Dubois, P.; Marchand, G.; Fouillet, Y.; Berthier, J.; Douki, T.; Hassine, F.; Gmouh, S.; Vaultier, M. Ionic liquid droplet as e-microreactor. *Analytical Chemistry* **2006,** *78*, 4909-4917.

(8) Liu, K.-K.; Wu, R.-G.; Chuang, Y.-J.; Khoo, H. S.; Huang, S.-H.; Tseng, F.-G. Microfluidic systems for biosensing. *Sensors* **2010,** *10*, 6623-6661.

(9) Chu, Z.; Seeger, S. Superamphiphobic surfaces. *Chemical Society Reviews* **2014,** *43*, 2784-2798.

(10) Wen, L.; Tian, Y.; Jiang, L. Bioinspired Super-Wettability from Fundamental Research to Practical Applications. *Angewandte Chemie International Edition* **2015**.

(11) Ahuja, A.; Taylor, J.; Lifton, V.; Sidorenko, A.; Salamon, T.; Lobaton, E.; Kolodner, P.; Krupenkin, T. Nanonails: A simple geometrical approach to electrically tunable superlyophobic surfaces. *Langmuir* **2008,** *24*, 9-14.

(12) Ghosh, S.; Lagraauw, R.; Otten, S.; Pit, A.; Berendsen, C.; Zeegers, J.; van den Ende, D.; Mugele, F. Trapping of drops by wetting defects. *Nature communications* **2014,** *5*.

(13) Kwon, G.; Kota, A.; Li, Y.; Sohani, A.; Mabry, J. M.; Tuteja, A. On-Demand Separation of Oil-Water Mixtures. *Advanced Materials* **2012,** *24*, 3666-3671.

(14) McHale, G.; Herbertson, D.; Elliott, S.; Shirtcliffe, N.; Newton, M. Electrowetting of nonwetting liquids and liquid marbles. *Langmuir* **2007,** *23*, 918-924.

(15) Hong, X.; Gao, X.; Jiang, L. Application of superhydrophobic surface with high adhesive force in no lost transport of superparamagnetic microdroplet. *Journal of the American Chemical Society* **2007,** *129*, 1478-1479.

(16) Khalil, K. S.; Mahmoudi, S. R.; Abu-dheir, N.; Varanasi, K. K. Active surfaces: Ferrofluid-impregnated surfaces for active manipulation of droplets. *Applied Physics Letters* **2014,** *105*, 041604.

(17) Timonen, J. V.; Latikka, M.; Leibler, L.; Ras, R. H.; Ikkala, O. Switchable static and dynamic self-assembly of magnetic droplets on superhydrophobic surfaces. *Science* **2013,** *341*, 253-257.

(18) Glavan, A. C.; Martinez, R. V.; Subramaniam, A. B.; Yoon, H. J.; Nunes, R.; Lange, H.; Thuo, M. M.; Whitesides, G. M. Omniphobic "RF paper" produced by silanization of paper with fluoroalkyltrichlorosilanes. *Advanced Functional Materials* **2014,** *24*, 60-70.

(19) Mertaniemi, H.; Forchheimer, R.; Ikkala, O.; Ras, R. H. Rebounding Droplet-Droplet Collisions on Superhydrophobic Surfaces: from the Phenomenon to Droplet Logic. *Advanced Materials* **2012,** *24*, 5738-5743.

(20) Mertaniemi, H.; Jokinen, V.; Sainiemi, L.; Franssila, S.; Marmur, A.; Ikkala, O.; Ras, R. H. Superhydrophobic Tracks for Low-Friction, Guided Transport of Water Droplets. *Advanced Materials* **2011,** *23*, 2911-2914.

(21) Ishii, D.; Shimomura, M. Invisible gates for moving water droplets: adhesive force gradients on a biomimetic superhydrophobic surface. *Chemistry of Materials* **2013,** *25*, 509-513.

(22) Ju, J.; Zheng, Y.; Jiang, L. Bioinspired one-dimensional materials for directional liquid transport. *Accounts of chemical research* **2014,** *47*, 2342-2352.

(23) McHale, G.; Elliott, S. J.; Newton, M. I.; Shirtcliffe, N. J. Superhydrophobicity: Localized parameters and gradient surfaces. *Contact Angle, Wettability and Adhesion', Koninklijke Brill NV* **2009,** *6*, 219-233.

(24) McHale, G.; Shirtcliffe, N. J.; Newton, M. I. Super-hydrophobic and super-wetting surfaces: Analytical potential? *Analyst* **2004,** *129*, 284-287, DOI: 10.1039/B400567H.

(25) Nilsson, M. A.; Rothstein, J. P. Using sharp transitions in contact angle hysteresis to move, deflect, and sort droplets on a superhydrophobic surface. *Physics of Fluids* **2012,** *24*, 062001, DOI: doi:http://dx.doi.org/10.1063/1.4723866.

(26) Reyssat, M.; Pardo, F.; Quéré, D. Drops onto gradients of texture. *EPL (Europhysics Letters)* **2009,** *87*, 36003.

(27) Kota, A. K.; Choi, W.; Tuteja, A. Superomniphobic surfaces: Design and durability. *MRS Bulletin* **2013,** *38*, 383-390, DOI: doi:10.1557/mrs.2013.101.

(28) Kota, A. K.; Kwon, G.; Tuteja, A. The design and applications of superomniphobic surfaces. *NPG Asia Mater* **2014,** *6*, e109, DOI: 10.1038/am.2014.34.

(29) Lafuma, A.; Quere, D. Superhydrophobic states. *Nat Mater* **2003,** *2*, 457-460.

(30) Nosonovsky, M.; Bhushan, B. Superhydrophobic surfaces and emerging applications: non-adhesion, energy, green engineering. *Current Opinion in Colloid & Interface Science* **2009,** *14*, 270-280.

(31) Kota, A. K.; Li, Y.; Mabry, J. M.; Tuteja, A. Hierarchically Structured Superoleophobic Surfaces with Ultralow Contact Angle Hysteresis. *Advanced Materials* **2012,** *24*, 5838-5843, DOI: 10.1002/adma.201202554.

(32) Liu, T.; Kim, C. Turning a surface superrepellent even to completely wetting liquids. *Science* **2014,** *346*.

(33) Tuteja, A.; Choi, W.; Ma, M.; Mabry, J. M.; Mazzella, S. A.; Rutledge, G. C.; McKinley, G. H.; Cohen, R. E. Designing superoleophobic surfaces. *Science* **2007,** *318*, 1618-1622.

(34) Tuteja, A.; Choi, W.; Mabry, J. M.; McKinley, G. H.; Cohen, R. E. Robust omniphobic surfaces. *Proceedings of the National Academy of Sciences* **2008,** *105*, 18200-18205.

(35) Zhao, H.; Law, K. Y.; Sambhy, V. Fabrication, Surface Properties, and Origin of Superoleophobicity for a Model Textured Surface. *Langmuir* **2011,** *27*, 5927-5935, DOI: 10.1021/la104872q.

(36) Furmidge, C. G. L. Studies at phase interfaces. I. The sliding of liquid drops on solid surfaces and a theory for spray retention. *Journal of Colloid Science* **1962,** *17*, 309-324, DOI: http://dx.doi.org/10.1016/0095-8522(62)90011-9.

(37) Choi, W.; Tuteja, A.; Mabry, J. M.; Cohen, R. E.; McKinley, G. H. A modified Cassie–Baxter relationship to explain contact angle hysteresis and anisotropy on non-wetting textured surfaces. *Journal of colloid and interface science* **2009,** *339*, 208-216.

(38) Whyman, G.; Bormashenko, E.; Stein, T. The rigorous derivation of Young, Cassie–Baxter and Wenzel equations and the analysis of the contact angle hysteresis phenomenon. *Chemical Physics Letters* **2008,** *450*, 355-359.

(39) Wu, G.; Wang, J.; Thomas, D. F.; Chen, A. Synthesis of F-doped flower-like TiO2 nanostructures with high photoelectrochemical activity. *Langmuir* **2008,** *24*, 3503-3509.

(40) Wang, R.; Hashimoto, K.; Fujishima, A.; Chikuni, M.; Kojima, E.; Kitamura, A.; Shimohigoshi, M.; Watanabe, T. Light-induced amphiphilic surfaces. *Nature* **1997,** *388*, 431-432.

(41) Lai, Y.; Huang, J.; Cui, Z.; Ge, M.; Zhang, K. Q.; Chen, Z.; Chi, L. Recent Advances in TiO2-Based Nanostructured Surfaces with Controllable Wettability and Adhesion. *Small* **2015**.

(42) Liu, K.; Cao, M.; Fujishima, A.; Jiang, L. Bio-inspired titanium dioxide materials with special wettability and their applications. *Chemical reviews* **2014,** *114*, 10044-10094.

(43) Owen, D.; Wendt, R. Estimation of the surface free energy of polymer. *J Appl Polym Sci* **1969,** *13*, 1741-1747.

(44) Neumann, A. Contact angles and their temperature dependence: thermodynamic status, measurement, interpretation and application. *Advances in colloid and interface science* **1974,** *4*, 105-191.

(45) Kwok, D. Y.; Neumann, A. W. Contact angle measurement and contact angle interpretation. *Advances in Colloid and Interface Science* **1999,** *81*, 167-249, DOI: http://dx.doi.org/10.1016/S0001-8686(98)00087-6.

(46) Pan, S.; Kota, A. K.; Mabry, J. M.; Tuteja, A. Superomniphobic surfaces for effective chemical shielding. *Journal of the American Chemical Society* **2012,** *135*, 578-581.

(47) Wang, R.; Hashimoto, K.; Fujishima, A.; Chikuni, M.; Kojima, E.; Kitamura, A.; Shimohigoshi, M.; Watanabe, T. Light-induced amphiphilic surfaces. *Nature* **1997,** *388*, 431-432.

(48) Wang, R.; Hashimoto, K.; Fujishima, A.; Chikuni, M.; Kojima, E.; Kitamura, A.; Shimohigoshi, M.; Watanabe, T. Photogeneration of highly amphiphilic TiO 2 surfaces. *Advanced Materials* **1998,** *10*, 135-138.

(49) Wang, R.; Sakai, N.; Fujishima, A.; Watanabe, T.; Hashimoto, K. Studies of surface wettability conversion on TiO2 single-crystal surfaces. *The Journal of Physical Chemistry B* **1999,** *103*, 2188-2194.

(50) Watanabe, T.; Nakajima, A.; Wang, R.; Minabe, M.; Koizumi, S.; Fujishima, A.; Hashimoto, K. Photocatalytic activity and photoinduced hydrophilicity of titanium dioxide coated glass. *Thin solid films* **1999,** *351*, 260-263.

(51) Sakai, N.; Fujishima, A.; Watanabe, T.; Hashimoto, K. Quantitative evaluation of the photoinduced hydrophilic conversion properties of TiO2 thin film surfaces by the reciprocal of contact angle. *The Journal of Physical Chemistry B* **2003,** *107*, 1028-1035.

(52) Wang, C.-y.; Groenzin, H.; Shultz, M. J. Molecular species on nanoparticulate anatase TiO2 film detected by sum frequency generation: trace hydrocarbons and hydroxyl groups. *Langmuir* **2003,** *19*, 7330-7334.

(53) White, J. M.; Szanyi, J.; Henderson, M. A. The photon-driven hydrophilicity of titania: A model study using TiO2 (110) and adsorbed trimethyl acetate. *The Journal of Physical Chemistry B* **2003,** *107*, 9029-9033.

(54) Takeuchi, M.; Sakamoto, K.; Martra, G.; Coluccia, S.; Anpo, M. Mechanism of photoinduced superhydrophilicity on the TiO2 photocatalyst surface. *The Journal of Physical Chemistry B* **2005,** *109*, 15422-15428.

(55) Zubkov, T.; Stahl, D.; Thompson, T. L.; Panayotov, D.; Diwald, O.; Yates, J. T. Ultraviolet light-induced hydrophilicity effect on TiO2 (110)(1× 1). Dominant role of the photooxidation of adsorbed hydrocarbons causing wetting by water droplets. *The Journal of Physical Chemistry B* **2005,** *109*, 15454-15462.

(56) Dettre, R.; Johnson, R. Contact angle hysteresis, I. Study of an idealized rough surface. *Adv. Chem. Ser* **1964,** *43*, 112.

(57) Dettre, R. H.; Johnson Jr, R. E. Contact Angle Hysteresis. IV. Contact Angle Measurements on Heterogeneous Surfaces1. *The journal of physical chemistry* **1965,** *69*, 1507-1515.

(58) Johnson Jr, R. E.; Dettre, R. H. Contact angle hysteresis. III. Study of an idealized heterogeneous surface. *The journal of physical chemistry* **1964,** *68*, 1744-1750.

(59) Bormashenko, E.; Pogreb, R.; Whyman, G.; Bormashenko, Y.; Erlich, M. Vibration-induced Cassie-Wenzel wetting transition on rough surfaces. *Applied physics letters* **2007,** *90*, 201917.

CHAPTER 4 – RAPID, FIELD-DEPLOYABLE, LOW-COST DEVICE TO DETECT

FUEL QUALITY

Summary: We employed liquid repellent (e.g., non-textured, non-polar slippery) surfaces to fabricate a simple, field-deployable, low-cost device to rapidly detect the quality of fuel blends (e.g., diesel-kerosene blends with different compositions) by sensing their surface tension with significantly improved resolution (**submitted to ACS Applied Materials & Interfaces, 2018**). In addition to detecting adulterated fuel, we envision that our methodology can also be used for personalized point-of-care diagnostic platforms, biochemical assays and biosensors.

4.1. Introduction

Numerous developing countries in Asia (e.g., India) and Africa (e.g., Nigeria) offer subsidized fuels such as kerosene to support lighting and cooking needs of the rural poor.[1-3] However, the lower cost of kerosene compared to market-rate fuels results in fuel adulteration, the unauthorized addition of foreign substance into fuel (e.g., introduction of kerosene to diesel or gasoline). For example, about 40% of the kerosene sold in India frequently gets blended with gasoline and diesel.[4-6] This significantly alters the desired specifications of the fuel and can give rise to the substantial economic and environmental concerns.[4, 6] Thus far, the misuse of kerosene has been hard to quantify in the field (e.g., at the dispensing gas station) because the currently used technologies (e.g., gas chromatography–mass spectrometry, Fourier transform infrared spectrometry, microcontroller sensor, long period fiber grating, hydrometer etc.) are either time consuming or expensive or not sensitive enough or require well-equipped analytical laboratories.[6-9] To circumvent this issue, there is a critical need to develop and deploy rapid, low-cost, easy-to-use devices to detect fuel adulteration in the field, specifically in developing economies where fuel quality is a concern.

In the past decade, manipulation of liquid droplets with the aim of identifying the physical or chemical properties of the liquids has received significant attention.[10-15] In chapter three, we developed a device that can rapidly detect compositions of liquid blends by sensing their surface tension.[15] The device was fabricated using a textured superomniphobic surface.[16-18] However, such superomniphobic surface-based devices have relatively low resolution (~ 10 mN m^{-1}) and poor mechanical durability (i.e., not field-deployable) due to the surface texture. In order to overcome these challenges, in this work, we employed liquid repellent (e.g., non-textured, non-polar slippery) surfaces to fabricate a simple, field-deployable, low-cost device to rapidly detect the quality of fuel blends (e.g., diesel-kerosene blends with different compositions) by sensing their surface tension with significantly improved resolution (~1 mN m^{-1}). In addition to detecting adulterated fuel, we envision that our methodology can also be used for personalized point-of-care diagnostic platforms, biochemical assays and biosensors.

4.2. Design Principles

The working principle of our devices relies on the differences in the mobility of liquid droplets with different surface tensions. One measure of the mobility of a liquid droplet on a solid surface is the sliding angle (i.e., the minimum angle ω by which the surface must be tilted relative to the horizontal for a droplet to slide off from the surface). As stated in chapters two and three, low contact angle hysteresis on non-textured surfaces $\Delta\theta = \theta_{adv} - \theta_{rec}$ (i.e., the difference between the advancing [maximum] contact angle θ_{adv} and the receding [minimum] contact angle θ_{rec}) results in low sliding angles ω, as implied by a balance between work done by gravity and work expended due to adhesion:[19-20]

$$\rho g V \sin\omega \approx \gamma_{lv} D_{TCL} \left(\cos\theta_{rec} - \cos\theta_{adv} \right) \tag{4-1}$$

Here, D_{TCL} is the width of solid–liquid–vapor contact line perpendicular to the sliding direction, γ_{lv} and ρ are the surface tension and density of the liquid, g is acceleration due to gravity, and V is the volume of the liquid droplet.

Typically, for droplets of a binary liquid system (e.g., a miscible liquid blend or a solution) or droplets of a homologous series (e.g., alkanes etc.) on a non-textured, non-polar slippery solid surface, the sliding angle ω increases with increasing surface tension γ_{lv}. This is perhaps due to the increased dispersive interactions between the non-polar solid and the liquid. Now, consider three droplets of a binary liquid system or a homologous series with same volume, but different surface tensions – low surface tension $\gamma_{lv,low}$, intermediate surface tension $\gamma_{lv,inter}$, and high surface tension $\gamma_{lv,high}$ – placed on a non-textured, non-polar slippery surface. When the surface is horizontal, all the three droplets will remain stationary. When the surface is tilted at a certain tilt angle α relative to horizontal, it may be anticipated that the droplet with $\gamma_{lv,low}$ slides off, while the droplets with $\gamma_{lv,inter}$ and $\gamma_{lv,high}$ remain adhered to the surface. At a higher tilt angle α', it may be anticipated that the droplets with $\gamma_{lv,low}$ and $\gamma_{lv,inter}$ slide off, while the droplet with $\gamma_{lv,high}$ remains adhered to the surface. At an even higher tilt angle α'', it may be anticipated that all the three droplets will slide off from the surface. In this manner, using non-textured, non-polar surfaces tilted at different tilt angles, the sliding angle ω of a droplet of a binary liquid system or a homologous series with unknown composition can be estimated. Using this estimated sliding angle ω, the surface tension γ_{lv} and the chemical composition of the unknown liquid can be estimated using pre-determined calibration curves. This is the premise of our devices that can detect the quality of fuel or fuel blends.

It must be noted that for an effective sorting of droplets based on surface tension with a high resolution, sufficient difference in sliding angles is necessary. One way to increase the resolution of the device (i.e., the difference in sliding angles of different liquids) is by increasing the contact angle hysteresis. In fact, the motion of partially wetting liquid drops in contact with a solid surface is strongly affected by contact angle hysteresis and interfacial pinning.[21] Contact angle hysteresis is related to the energy barriers that a liquid droplet must overcome during its movement along a solid surface, and thus characterizes the resistance to droplet movement (e.g., the resistance of micro-scale heterogeneities on the surface).[22-24] Typically, the resistance to droplet movement and so the contact angle hysteresis on non-textured, non-polar slippery surfaces is lower for low surface tension liquids compared to high surface tension liquids. This is consistent with the theory (Equation 4-1), that the sliding angle typically decreases with both decreasing liquid surface tension and contact angle hysteresis.[19, 25] However, while comparing the sliding angles of different liquids, one should be cautious about the droplets volume, density of liquids and also the chemical interaction of the liquids with the substrate.[26-28] Therefore, in order to properly sort liquid droplets based on their surface tension, with an appropriate choice of surface chemistry and surface roughness and droplet volume, one could obtain sufficient variation in sliding angle.

4.3. Fabrication of Non-textured, Non-polar Slippery Surfaces

Building on the principles discussed above, we fabricated non-textured, non-polar slippery surfaces using two different surface chemistries, octadecyltrichlorosilane (OTS) and heptadecafluoro-1,1,2,2-tetrahydrodecyl trichlorosilane (FDTS) via liquid phase silanization. For fabrication of non-textured, non-polar slippery OTS-and FDTS-treated surface, the silicon wafer/glass substrate was first sonicated in ethanol-DI water (1:1, v/v) solution for 10 min and

then rinsed with copious amounts of DI water to remove any impurity on the surface. The cleaned silicon wafer/glass substrate was then placed in a plasma chamber (Plasma etch) for 15 minutes to deposit hydroxyl groups over the surface which reacts readily with silane. After that the silicon wafer/glass substrate was placed in a reactive solution which was prepared at scales ranging from 10 to 50 ml in a polypropylene screw-cap tube (Falcon) for 2 hours. For example, 15 ml of toluene (Fisher Chemical), 12 μl of hydrochloric acid (Fisher Scientific) and 16 μl of either octadecyltrichlorosilane (to fabricate OTS-treated surface; Gelest) or heptadecafluoro-1,1,2,2-tetrahydrodecyl trichlorosilane (to fabricate FDTS-treated surface; Gelest) were added to a bottle (see Figure 4.1). The sample was then dried by blowing nitrogen.
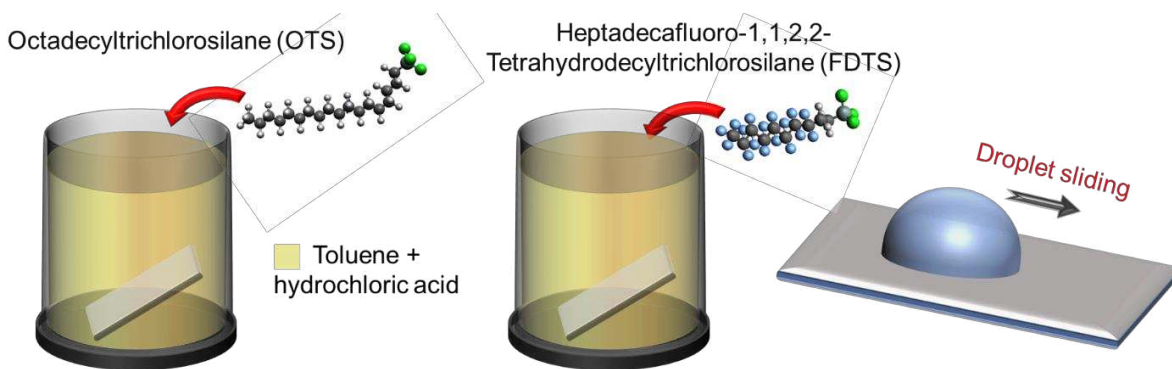
Figure 4.1. Schematics depicting the fabrication of non-textured, non-polar slippery OTS- and FDTS-treated surfaces.

We employed two different surface chemistries (i.e., hydrocarbon and fluorocarbon) to create different resolution of sorting liquid droplets based on surface tension. Such variation in the resolution of sorting between hydrocarbon and fluorocarbon can be attributed to the fluorocarbon chains being stiffer than hydrocarbon chains.[29-32] Further, we chose silicon wafers as our substrates because those are extremely smooth (to avoid the presence of micro-scale heterogeneities on the surface that affects the contact angle hysteresis) and upon forming hydroxyl groups, react readily with silanes.

4.4. Characterization of Non-textured, Non-polar Slippery Surfaces

In order to characterize the surface chemical composition and assure the uniformity and coverage of the surface chemistry across each sample, we conducted XPS and obtained the full survey spectra and high-resolution C1s XPS spectra (see Figure 4.2.) for each studied surface chemistry. At least three spots were analyzed on each studied surface chemistry and one full survey and one C1s spectra is shown for each surface chemistry.
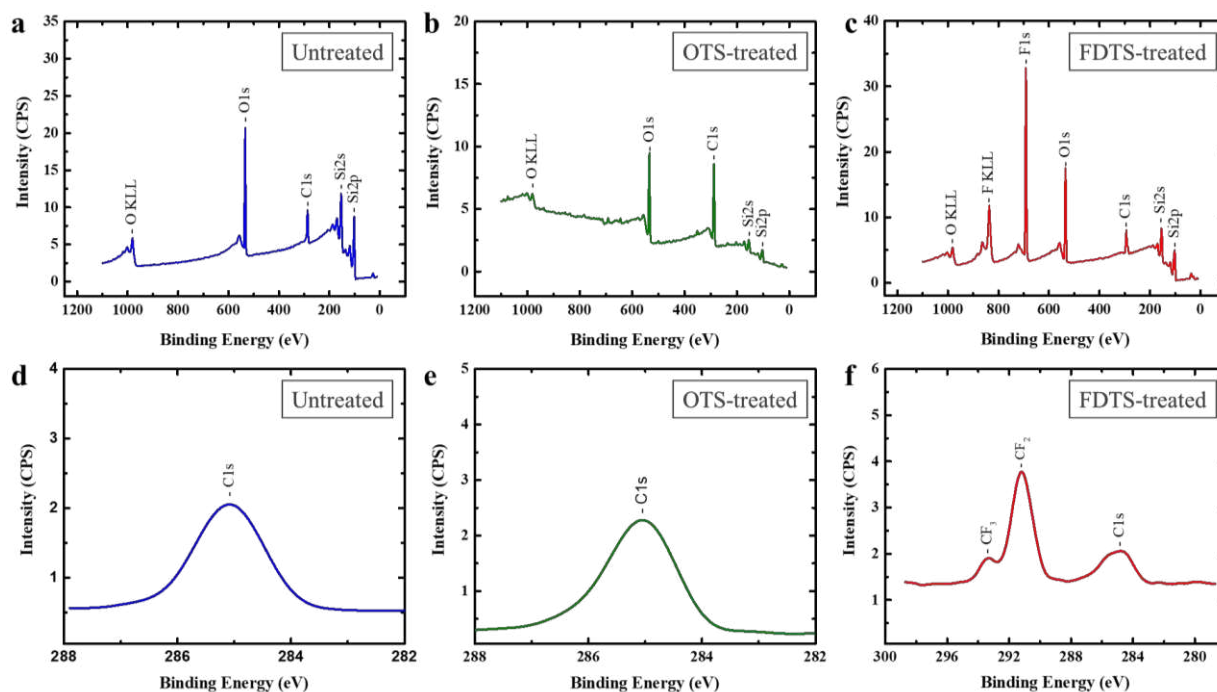
Figure 4.2. Full survey XPS spectra of a) untreated, b) OTS-treated and c) FDTS-treated silicon wafers. High-resolution C1s XPS spectra of d) untreated, e) OTS-treated and f) FDTS-treated silicon wafers.

Further, a wide range of liquids with a broad range of surface tension and viscosity can slide off easily from such non-textured, non-polar slippery surfaces. We measured the advancing and receding contact angles and sliding angles for liquids with a wide range of surface tension, $20 \text{ mN m}^{-1} \leq \gamma_{lv} \leq 72 \text{ mN m}^{-1}$, on non-textured, non-polar slippery OTS and FDTS-treated silicon wafer as shown in Table 4.1.

57

Table 4.1. The contact angles and sliding angles of different liquids on OTS-treated silicon wafers.

Liquid	Surface tension (mN m^{-1})	θ_{adv} (°)	θ_{rec} (°)	ω (°)
Diiodomethane	50.8	70	65	5
Dimethylformamide	37.1	45	40	4
Toluene	28.2	39	36	2
Chloroform	27.5	37	34	2

4.5. Non-textured, Non-polar Slippery Surfaces – Experiments

In order to study the resolution of sorting of liquid droplets on non-textured, non-polar slippery surfaces, we investigated the sliding angles of different liquid systems on non-textured, non-polar slippery OTS- and FDTS- treated silicon wafers. First, we measured the sliding angle of liquid droplets of water-sodium dodecyl sulfate (SDS) liquid system, water-ethanol liquid system and alkanes (Figures 4.3a–4.3c) on non-textured, non-polar slippery OTS-treated silicon wafers. For each liquid system, we looked at the influence of the liquid droplet volume on the sliding angle and the resolution of sorting. As anticipated by decreasing the liquid droplet volume, the sliding angle for each liquid droplet increases.[33-34] Further, by decreasing the liquid droplet volume, the range of variation of sliding angles and so the sorting resolution increases. For example, the sliding angles for water-SDS liquid system on non-textured, non-polar slippery OTS-treated silicon wafer change between 6° to 13° for 20µl liquid droplets, 11° to 22° for 10µl liquid droplets and 24° to 85° for 2µl liquid droplets (Figure 4.3a). However, it should be noted that the sliding velocity on liquid droplets with smaller volume is lower compared to larger volume droplets and sometimes the movement of droplet may not be clear or noticeable

without watching carefully at the motion of triple-phase contact line. Consequently, it requires better precision to sort liquid droplets with smaller volume based on their surface tension (particularly droplets with volume <2 μl). Further, the easy sliding of water droplet (a representative high surface tension liquid; γ_{lv} = 72 mN m^{-1}) and n-decane droplet (a representative low surface tension liquid; γ_{lv} = 20 mN m^{-1}) on non-textured, non-polar slippery OTS-treated silicon wafers is demonstrated (see Figures 4.3d–4.3e).
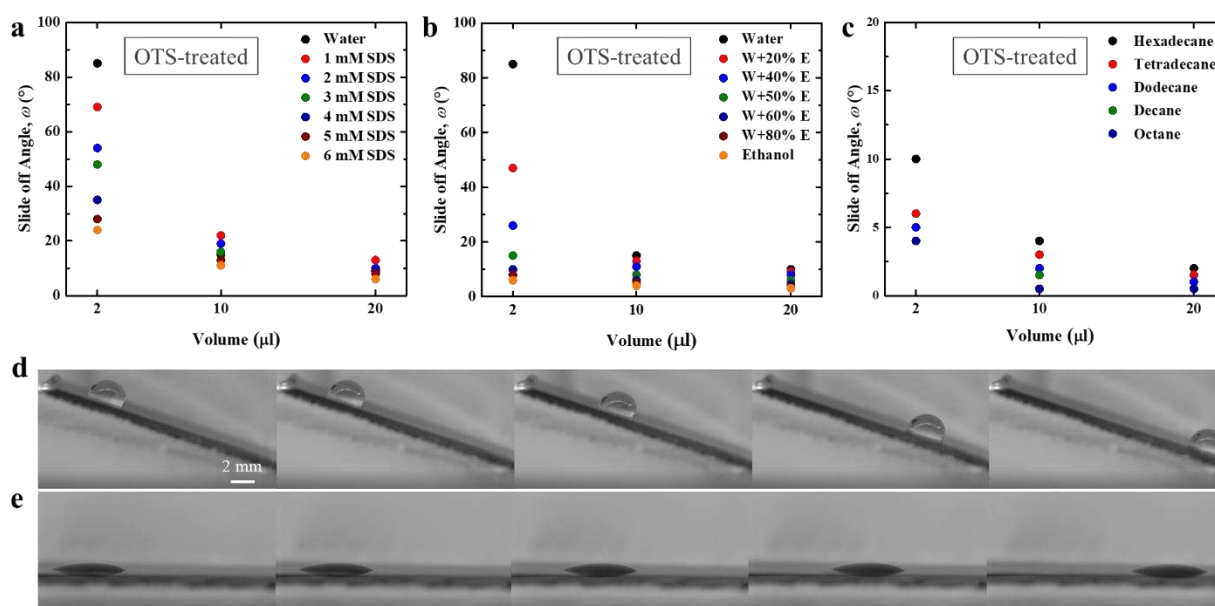
Figure 4.3. Variation of sliding angle with volume on non-textured, non-polar slippery OTS-treated silicon wafer for a) water-SDS liquid system, b) water-ethanol liquid system and c) alkanes. A series of snapshots captured from the video showing the sliding of a 10 μl d) water droplet (a representative high surface tension liquid) and e) n-decane droplet (a representative low surface tension liquid) on non-textured, non-polar slippery OTS-treated silicon wafer tilted at 20° and 3° relative to horizontal, respectively. For each liquid, significant difference was observed between sliding angles of 10 μl and 2 μl droplets ($p \leq 0.05$ at α=0.05). Further, significant difference was observed between sliding angles of alkanes on OTS-treated silicon wafers for 2 μl droplets ($p \leq 0.05$ at α=0.05).

Further, we measured the sliding angle of liquid droplets of water-SDS liquid system, water-ethanol liquid system and alkanes for 2, 5 and 10 μl droplets (Figures 4.4a–4.4c) on non-textured, non-polar slippery FDTS-treated silicon wafers. Similar to OTS-treated silicon wafers,

on slippery non-textured FDTS-treated silicon wafers, the increase in the liquid surface tension and the decrease in liquid droplet volume result in the increase in the sliding angle for each liquid droplet. Water droplet and n-decane droplet can easily slide on slippery non-textured FDTS-treated silicon wafers (see Figures 4.4d–4.4e) easily.
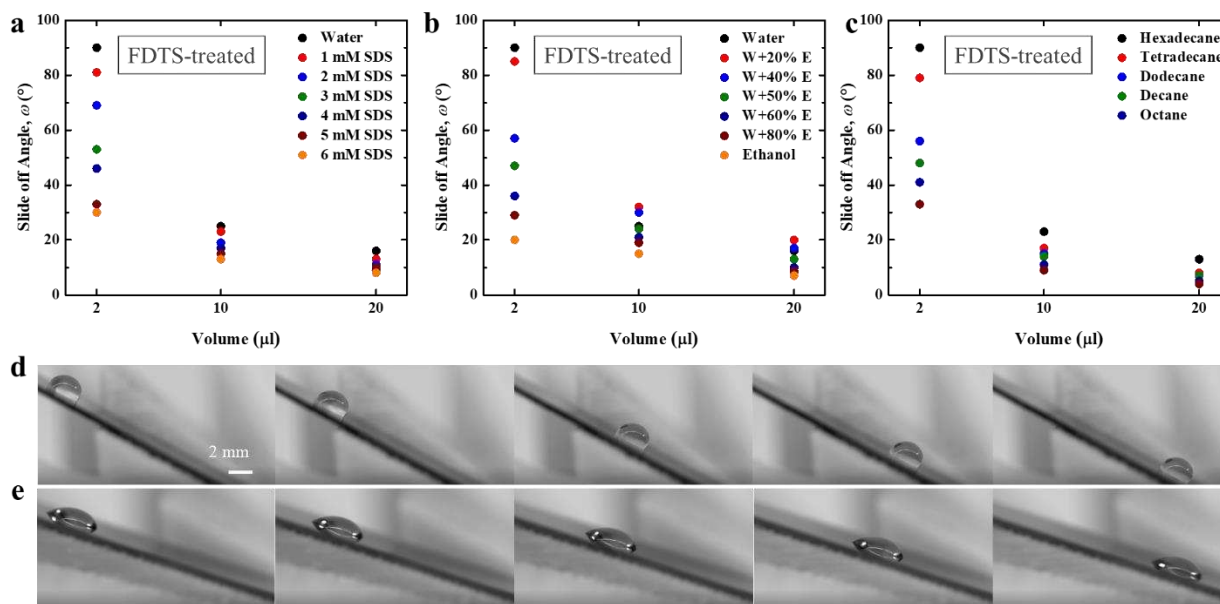
Figure 4.4. Variation of sliding angle with volume on non-textured, non-polar slippery FDTS-treated silicon wafer for a) water-SDS liquid system, b) water-ethanol liquid system and c) alkanes. A series of snapshots captured from the video showing the sliding of a 10 μl d) water droplet and e) n-decane droplet on non-textured, non-polar slippery FDTS-treated silicon wafer tilted at 30° and 10° relative to horizontal, respectively. For each liquid, significant difference was observed between sliding angles of 20 μl, 10 μl and 2 μl droplets ($p \leq 0.05$ at $\alpha=0.05$). Further, significant difference was observed between sliding angles of alkanes on FDTS-treated silicon wafers for 2 μl droplets ($p \leq 0.05$ at $\alpha=0.05$).

Our results indicated that different surface chemistries may induce different sorting resolution for a particular liquid system. For example, for 10 μl liquid droplets of different alkanes, the sliding angles change between 0.5° to 4° on non-textured, non-polar slippery OTS-treated silicon wafers, but between 9° to 23° on non-textured, non-polar slippery FDTS-treated silicon wafers (Figures 4.3c and 4.4c). Further, our experimentally measured sliding angles match reasonably well with the predictions based on the work by Furmidge. It should be noted

that, the sorting resolution for water-SDS and water-ethanol liquid systems is comparable on both non-textured, non-polar slippery OTS- and FDTS-treated surfaces and either of these surfaces can be utilized for sorting of these liquid systems.

4.6. A Device to Detect the Fuel Quality

In order to design the fuel quality sensor, we measured the sliding angles of the fuel blends with different compositions (i.e., diesel-kerosene liquid system) for different droplet volumes on a non-textured, non-polar slippery OTS-treated silicon wafer (Figure 4.5a). The sliding angles for diesel-kerosene liquid system on non-textured, non-polar slippery OTS-treated silicon wafer change between 1° to 4° for 20μl liquid droplets, 2° to 6° for 10μl liquid droplets, 5° to 11° for 5μl liquid droplets and 9° to 25° for 2μl liquid (Figure 4.5a). As anticipated the sliding angle decreases with both decreasing liquid surface tension and contact angle hysteresis. Based on the obtained values, non-textured, non-polar slippery OTS-treated silicon wafer cannot provide sufficient differences between the sliding angles of different compositions of fuel blends. Therefore, such surface is not a good candidate for detecting small differences in surface tension and consequently could not identify the adulteration of diesel blended with small amounts of kerosene. In addition, as discussed earlier, although the differences in sliding angles of diesel-kerosene liquid system is relatively high (i.e., 9° to 25°) for 2μl liquids, the motion of 2μl liquid droplets cannot be clearly visualized. To resolve this issue, we utilized glass slides and fabricated them similar to silicon wafers to obtain non-textured, non-polar slippery OTS-treated glass substrate. We measured the sliding angles for diesel-kerosene liquid system on non-textured, non-polar slippery OTS-treated glass and observed the change in sliding angles between 5° to 10° for 20μl liquid droplets, 7° to 16° for 10μl liquid droplets, 9° to 25° for 5μl liquid droplets and 21° to 47° for 2μl liquid (Figure 4.5b). Such differences between the sorting resolution of

non-textured, non-polar slippery OTS silicon wafer and glass can be attributed to the relatively higher surface roughness of OTS-treated glass slide (R_{rms} = 15.7±0.8 nm) compared to the OTS-treated silicon wafer (R_{rms} = 3.6±0.5 nm). The relatively higher surface roughness on glass substrate results in higher contact angle hysteresis and consequently higher sliding angles for diesel-kerosene liquid systems. Therefore, non-textured, non-polar slippery OTS-treated glass substrates were chosen as the desired substrates for the fuel quality sensor based on their sorting resolution. It should also be noted that the droplets of diesel with different concentration of kerosene could not slide off from non-textured, non-polar slippery FDTS-treated silicon wafer or glass, likely due to the existing impurities (e.g., lead, sulfur, halogenated compounds, etc.) in fuel blends and their interaction with fluorocarbon surface chemistry.

We designed a simple device consisting of different tilt angles for holding non-textured, non-polar slippery OTS-treated glass substrates at certain angles relative to horizontal (Figure 4.5c) and fabricated it through 3D printing. The device with different tilt angles was fabricated using 3D printer from acrylonitrile butadiene styrene (ABS) using uPrint SE (Stratasys, Eden Prairie, MN, USA). The 3D-printed device was designed with Creo Parametric software. For demonstration of fuel quality sensor, we placed three non-textured, non-polar slippery OTS-treated glass substrates on the 3D-printed embedded stands corresponding to 12°, 15° and 20° tilt angles relative to the horizontal. First, three 5 µl droplets of diesel + 25% kerosene (with γ_{lv} = 22.3 mN m^{-1}) were placed on non-textured, non-polar slippery OTS-treated glass substrates (Figure 4.5d). As anticipated based on the measured sliding angles, Diesel + 25% kerosene liquid droplets slid off from all three 12°, 15° and 20° tilted non-textured, non-polar slippery OTS-treated glass substrates (Figure 4.5d). After that, we placed three 5 µl droplets of diesel + 10%

kerosene (with γ_{lv} = 23.9 mN m^{-1}) on the tilted non-textured, non-polar slippery OTS-treated

glass substrates (Figure 4.5e).
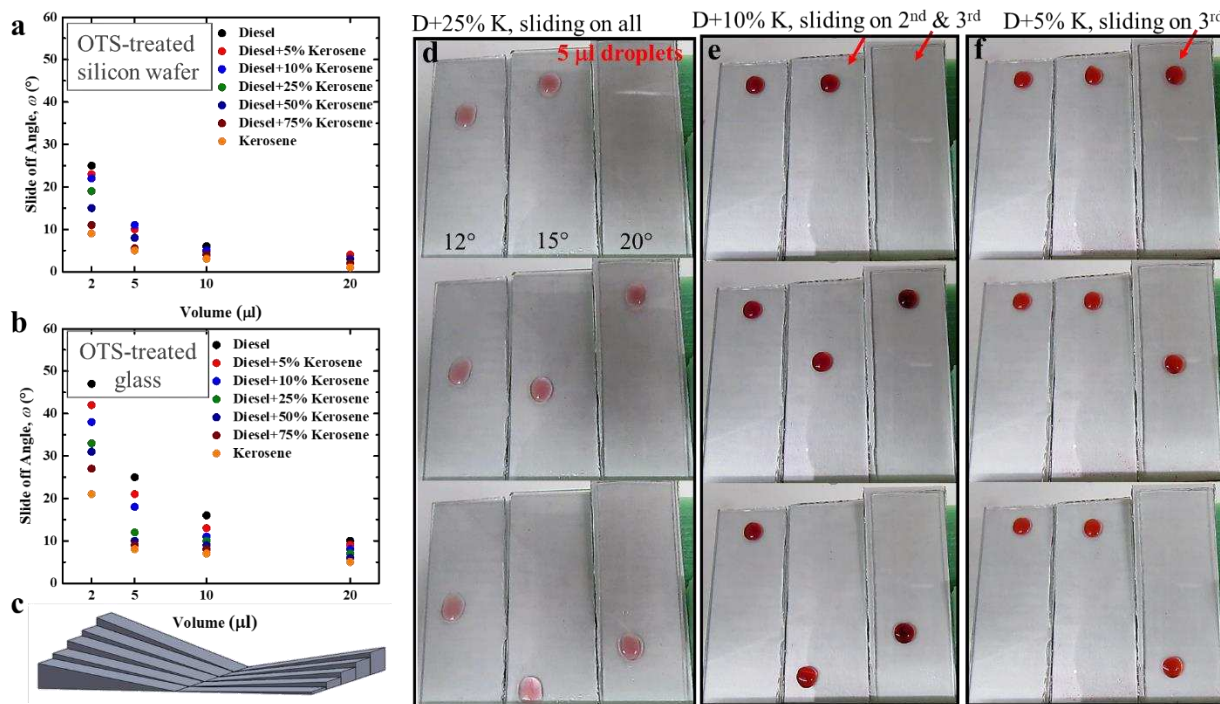
Figure 4.5. Variation of sliding angle with volume on non-textured, non-polar slippery OTS-treated a) silicon wafer substrate and b) glass substrate. c) A schematic of a field sensor with multiple angles sensing surfaces. (d-f) A series of snapshots captured from the video showing the fuel quality sensor. Three 5 μl droplets of d) diesel + 25% kerosene, e) diesel + 10% kerosene and f) diesel + 5% kerosene are placed on non-textured, non-polar slippery OTS-treated glass substrates tilted at 12°, 15° and 20°, respectively. Diesel + 25% kerosene droplets slide from all three tilted glass substrates, while diesel + 10% kerosene droplets slide only from 15° and 20° tilted glass substrates (and not 12° tilted glass substrate) and diesel + 5% kerosene droplets slide only from 20° tilted glass substrates (and not 12° and 15° tilted glass substrates). No statistically significant difference was observed for diesel-kerosene mixtures on OTS-treated silicon wafer for 20 μl and 10 μl droplets. Further, significant difference was observed between sliding angles of diesel-kerosene mixtures on OTS-treated glass for 2 μl droplets ($p \leq 0.05$ at α=0.05).

Diesel + 10% kerosene liquid droplets slid off only from 15° and 20° tilted non-textured,

non-polar slippery OTS-treated glass substrates (and not from 12° tilted substrate). Finally, three

5 μl droplets of diesel + 5% kerosene (with γ_{lv} = 24.5 mN m^{-1}) were placed on the tilted non-

textured, non-polar slippery OTS-treated glass substrates and slid only from 20° tilted substrate

(and not 12° and 15° tilted substrates; Figure 4.5f). In this manner, we demonstrated sorting of

fuel blends droplets based on their liquid composition which enables detecting the fuel adulteration. Such surfaces can be reused multiple times after completely washing and drying with ethanol and water solvents.

4.7. Conclusions

In conclusion, we fabricated non-textured, non-polar, slippery OTS and FDTS-treated surfaces that on which liquids with a wide range of surface tension can easily slide off. We discussed that the sliding angle of a liquid droplet on a slippery surface is strongly dependent on the liquid surface tension and contact angle hysteresis, which in turn depends on the composition of the liquid blend. Using such slippery surfaces and building on principles of sliding angles, we designed and fabricated a simple fuel sensor that can rapidly detect the composition of fuel blends. We demonstrated that our fuel sensor can detect small differences in surface tension and consequently could detect adulteration of diesel blended with small amounts of kerosene. In addition to detecting adulterated fuel, we envision that our methodology can also be used for personalized point-of-care diagnostic platforms, biochemical assays and biosensors.

REFERENCES

(1) del Granado, F. J. A.; Coady, D.; Gillingham, R. The unequal benefits of fuel subsidies: A review of evidence for developing countries. *World Development* **2012,** *40*, 2234-2248.

(2) Gangopadhyay, S.; Ramaswami, B.; Wadhwa, W. Reducing subsidies on household fuels in India: how will it affect the poor? *Energy Policy* **2005,** *33*, 2326-2336.

(3) Pitt, M. M. Equity, externalities and energy subsidies The case of kerosine in Indonesia. *Journal of Development Economics* **1985,** *17*, 201-217.

(4) Shenoy, B. V. Lessons learned from attempts to reform India's kerosene subsidy. **2010**.

(5) Rao, N. D. Kerosene subsidies in India: When energy policy fails as social policy. *Energy for Sustainable Development* **2012,** *16*, 35-43.

(6) Gawande, A.; Kaware, J. Fuel adulteration consequences in India: a review. *Sci Revs Chem Commun* **2013,** *3*, 161-171.

(7) Teixeira, L. S.; Oliveira, F. S.; dos Santos, H. C.; Cordeiro, P. W.; Almeida, S. Q. Multivariate calibration in Fourier transform infrared spectrometry as a tool to detect adulterations in Brazilian gasoline. *Fuel* **2008,** *87*, 346-352.

(8) Wiziack, N. K. L.; Catini, A.; Santonico, M.; D'amico, A.; Paolesse, R.; Paterno, L.; Fonseca, F. J.; Di Natale, C. A sensor array based on mass and capacitance transducers for the detection of adulterated gasolines. *Sensors and Actuators B: Chemical* **2009,** *140*, 508-513.

(9) M., B. L. V. a. H. Review on the Detection of Fuel Adulteration through Sensor based Techniques. *Int. J. Sci. Res. Publ.* **2017,** *7*, 2250-3153.

(10) Whitesides, G. M. The origins and the future of microfluidics. *Nature* **2006,** *442*, 368-373.

(11) Mazutis, L.; Araghi, A. F.; Miller, O. J.; Baret, J.-C.; Frenz, L.; Janoshazi, A.; Taly, V.; Miller, B. J.; Hutchison, J. B.; Link, D. Droplet-based microfluidic systems for high-throughput single DNA molecule isothermal amplification and analysis. *Analytical chemistry* **2009,** *81*, 4813-4821.

(12) Liu, K.-K.; Wu, R.-G.; Chuang, Y.-J.; Khoo, H. S.; Huang, S.-H.; Tseng, F.-G. Microfluidic systems for biosensing. *Sensors* **2010,** *10*, 6623-6661.

(13) Ishii, D.; Shimomura, M. Invisible gates for moving water droplets: adhesive force gradients on a biomimetic superhydrophobic surface. *Chemistry of Materials* **2013,** *25*, 509-513.

(14) Nilsson, M. A.; Rothstein, J. P. Using sharp transitions in contact angle hysteresis to move, deflect, and sort droplets on a superhydrophobic surface. *Phys. Fluids* **2012,** *24*, 062001.

(15) Movafaghi, S.; Wang, W.; Metzger, A.; Williams, D.; Williams, J.; Kota, A. Tunable superomniphobic surfaces for sorting droplets by surface tension. *Lab on a Chip* **2016,** *16*, 3204-3209.

(16) Movafaghi, S.; Leszczak, V.; Wang, W.; Sorkin, J. A.; Dasi, L. P.; Popat, K. C.; Kota, A. K. Hemocompatibility of superhemophobic titania surfaces. *Advanced healthcare materials* **2017,** *6*.

(17) Pendurthi, A.; Movafaghi, S.; Wang, W.; Shadman, S.; Yalin, A. P.; Kota, A. K. Fabrication of nanostructured omniphobic and superomniphobic surfaces with inexpensive CO2 laser engraver. *ACS applied materials & interfaces* **2017,** *9*, 25656-25661.

(18) Vahabi, H.; Wang, W.; Movafaghi, S.; Kota, A. K. Free-standing, flexible, superomniphobic films. *ACS applied materials & interfaces* **2016,** *8*, 21962-21967.

(19) Furmidge, C. Studies at phase interfaces. I. The sliding of liquid drops on solid surfaces and a theory for spray retention. *Journal of colloid science* **1962,** *17*, 309-324.

(20) Kota, A. K.; Li, Y.; Mabry, J. M.; Tuteja, A. Hierarchically structured superoleophobic surfaces with ultralow contact angle hysteresis. *Advanced Materials* **2012,** *24*, 5838-5843.

(21) Semprebon, C.; Varagnolo, S.; Filippi, D.; Perlini, L.; Pierno, M.; Brinkmann, M.; Mistura, G. Deviation of sliding drops at a chemical step. *Soft matter* **2016,** *12*, 8268-8273.

(22) Marmur, A. Contact angle hysteresis on heterogeneous smooth surfaces. *J. Colloid Interface Sci.* **1994,** *168*, 40-46.

(23) Johnson Jr, R. E.; Dettre, R. H. Contact angle hysteresis. III. Study of an idealized heterogeneous surface. *The journal of physical chemistry* **1964,** *68*, 1744-1750.

(24) Gao, L.; McCarthy, T. J. Contact angle hysteresis explained. *Langmuir* **2006,** *22*, 6234-6237.

(25) Wang, L.; McCarthy, T. J. Covalently attached liquids: instant omniphobic surfaces with unprecedented repellency. *Angew. Chem.* **2016,** *128*, 252-256.

(26) Varagnolo, S.; Filippi, D.; Mistura, G.; Pierno, M.; Sbragaglia, M. Stretching of viscoelastic drops in steady sliding. *Soft matter* **2017,** *13*, 3116-3124.

(27) Richard, D.; Quéré, D. Viscous drops rolling on a tilted non-wettable solid. *EPL (Europhysics Letters)* **1999,** *48*, 286.

(28) Yoshida, N.; Abe, Y.; Shigeta, H.; Takami, K.; Osaki, H.; Watanabe, T.; Hashimoto, K.; Nakajima, A. Preparation and water droplet sliding properties of transparent hydrophobic polymer coating by molecular design for self-organization. *J. Sol-Gel Sci. Technol.* **2004,** *31*, 195-199.

(29) Texter, J. *Reactions and synthesis in surfactant systems*, CRC Press: 2001.

(30) Kujawa, P.; Liu, R. C.; Winnik, F. M. Do fluorocarbon, hydrocarbon, and polycyclic aromatic groups intermingle? A study of the interactions in water between fluorocarbon-and hydrocarbon-modified poly (N-isopropylacrylamides). *The Journal of Physical Chemistry B* **2002,** *106*, 5578-5585.

(31) Eaton, D. F.; Smart, B. E. Are fluorocarbon chains stiffer than hydrocarbon chains? Dynamics of end-to-end cyclization in a C8F16 segment monitored by fluorescence. *Journal of the American Chemical Society* **1990,** *112*, 2821-2823.

(32) Uneyama, K. *Organofluorine chemistry*, John Wiley & Sons: 2008.

(33) Chang, C.-C.; Wu, C.-J.; Sheng, Y.-J.; Tsao, H.-K. Anti-smudge behavior of facilely fabricated liquid-infused surfaces with extremely low contact angle hysteresis property. *RSC Advances* **2016,** *6*, 19214-19222.

(34) Yong, J.; Yang, Q.; Chen, F.; Zhang, D.; Du, G.; Bian, H.; Si, J.; Hou, X. Bioinspired superhydrophobic surfaces with directional Adhesion. *RSC Advances* **2014,** *4*, 8138-8143.

CHAPTER 5 – HEMOCOMPATIBILITY OF SUPERHEMOPHOBIC TITANIA SURFACES

Summary: In this work, we investigated the blood platelet adhesion and activation of truly superhemophobic surfaces and compared them with that of hemophobic surfaces and hemophilic surfaces (**published in Advanced Healthcare Materials, 2016; RSC Advances, 2017; Colloids and Surfaces B: Biointerfaces, 2018**). Our analysis indicates that only those superhemophobic surfaces with a robust Cassie-Baxter state display significantly lower platelet adhesion and activation. We envision that the understanding gained through this work will lead to the fabrication of improved hemocompatible, superhemophobic medical implants.

5.1. Introduction

Titanium-based implants have received a great deal of attention for their biocompatibility with many different tissues in the human body. However, when these implants come in contact with blood, protein adsorption and platelet adhesion and activation occur, which may lead to further thrombosis and sometimes failure of these implants.[1-6] It is well known that blood protein adsorption and platelet adhesion and activation can be tailored by tuning the chemistry and texture of surfaces.[7-11] One strategy that has been recently receiving attention is improving hemocompatibility (e.g., reduced protein adsorption and platelet adhesion and activation) by employing superhydrophobic surfaces.[8, 12-15] As described in chapter two, superhydrophobic surfaces display very high contact angles and very low roll off angles with water (a liquid with high surface tension, $\gamma_{lv} = 72.1$ mN m^{-1}).[16-17] But superhydrophobic surfaces may not display high contact angles and more importantly very low roll off angles with blood (a liquid with relatively lower surface tension,[18] $\gamma_{lv} \approx 56$ mN m^{-1}). In this context, we define superhemophobic surfaces as surfaces that display very high contact angles (> 150°) and very low roll off angles (< 10°) with blood. While there are a few studies[19-21] investigating the hemocompatibility of

superhydrophobic titania surfaces, it is not clear from the reports whether they are superhemophobic or not. In this work, for the first time, we investigated the blood protein and platelet adhesion and activation of truly superhemophobic surfaces and compared them with that of hemophobic surfaces (i.e., surfaces display contact angles > 90° with blood) and hemophilic surfaces (i.e., surfaces display contact angles < 90° with blood). Further, we studied the bacteria adhesion and biofilm formation on superhydrophobic titania nanotube surfaces. For each of our surfaces, we characterized the wettability using contact angle goniometry, the surface chemistry using XPS, and platelet adhesion and activation using fluorescence microscopy and SEM. Based on our results, the blood protein and platelet adhesion and activation reduced on superhemophobic surfaces. However, our results indicate that not all superhemophobic titania surfaces lead to significantly reduced platelet adhesion and activation. Our analysis indicates that only those superhemophobic surfaces with a robust Cassie-Baxter state[22] display significantly lower platelet adhesion and activation compared to hemophobic and hemophilic surfaces. Further, the bacteria adhesion and biofilm formation on superhydrophobic titania nanotube surfaces were lower compared to unmuddied titanium and unmodified nanotube arrays. We envision that the understanding gained through this work will lead to the fabrication of improved hemocompatible, superhemophobic medical implants.

5.2. Design Principles

As described in chapter two, when a liquid droplet is in Cassie-baxter state, pockets of air remain trapped underneath the liquid droplet introducing a composite liquid-air-solid interface. This greatly reduces the solid-liquid interfacial area, which in turn leads to high θ^* and low roll off angles ω.[23-26] Typically, the Cassie-Baxter state is preferred for designing super-repellent surfaces (e.g., superhydrophobic and superhemophobic surfaces). [16-17, 27] The Cassie-Baxter state

can be obtained by combining a surface chemistry possessing a low solid surface energy with an appropriate texture.[28-29]

As discussed in chapter two, the Cassie-Baxter state is a metastable state.[30-31] In order to have effective super-repellence to liquids, it is essential to have a robust Cassie-Baxter state with high $P_{breakthrough}$. One measure of the robustness of Cassie-Baxter state is the robustness factor A^*.[32-33] The robustness factor represents the ratio between the breakthrough pressure $P_{breakthrough}$ and reference pressure $P_{ref} = 2\gamma_{lv}/l_{cap}$, where $l_{cap} = \sqrt{\dfrac{\gamma_{lv}}{\rho g}}$ is the capillary length, ρ is the liquid density and g is the acceleration due to gravity. The reference pressure is approximately the minimum possible pressure difference across the composite interface for millimetric or larger liquid droplets or puddles on extremely non-wetting textured surfaces. When a liquid is in the Cassie-Baxter state on a textured solid, a generalized force balance across the composite (solid-liquid-air) interface can be written as:[32-33]

$$P_{breakthrough} \text{ (Interfacial area)} = \gamma_{lv} \text{ (Contact line length) } \sin \delta\theta \qquad (5\text{-}1)$$

Here, $\delta\theta$ is the sag angle of the liquid-vapor interface. For a textured solid composed of hexagonally packed textured surfaces composed of discrete pillars (such as the textures used in this work), equation 5-1 can be written as:

$$P_{breakthrough}\left(6\sqrt{3}(R+D)^2\right) \approx \gamma_{lv}\left(6\pi R\right)\sin \delta\theta \qquad (5\text{-}2)$$

Here, $2R$ is the pillar diameter and $2D$ is the inter-feature spacing (Figure 5.1). Solving for $P_{breakthrough}$, we get:

$$P_{breakthrough} \approx \left| \frac{\gamma_{lv}\pi R \cos \theta}{\sqrt{3}(R+D)^2} \right| \qquad (5\text{-}3)$$

Here, θ is the Young's contact angle. The robustness factor A^* is obtained as:

$$A^* = \frac{P_{breakthrough}}{P_{ref}} \approx \left| \frac{\pi R l_{cap} \cos\theta}{2\sqrt{3}(R+D)^2} \right| \tag{5-4}$$

Large values of A^* ($A^* \gg 1$) imply a robust Cassie-Baxter state. On the other hand, values of $A^* < 1$ imply that the composite interface cannot maintain its stability against small pressure differentials across the liquid-vapor interface and the Cassie-Baxter state is not robust. [32-33]
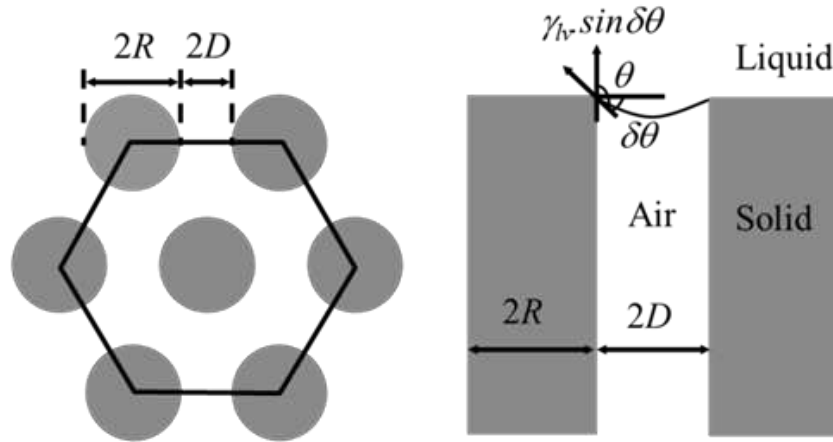
Figure 5.1. A textured solid composed of hexagonally packed pillars with diameter $2R$ and inter-feature spacing of $2D$.

5.3. Fabrication of Titania Surfaces

In this work, we fabricated superhemophobic titania surfaces with different values of A^* and compared their platelet adhesion and activation with hemophobic and hemophilic surfaces. In order to fabricate the hemophilic, hemophobic and superhemophobic titania surfaces, we employed three different morphologies – non-textured, nanoflowers and nanotubes – and for each morphology, three different surface chemistries – unmodified, PEGylated[34] and fluorinated.[35] We synthesized the non-textured titania surfaces via oxidation,[36] titania nanoflower surfaces via hydrothermal synthesis[37] and titania nanotube surfaces via electrochemical anodization.[6]

Titanium sheets (8 mm long × 8 mm wide × 0.8 mm thick) were cleaned with soap, followed by sonication in acetone and isopropanol and then dried with nitrogen gas. Non-textured titania surfaces were fabricated by dipping cleaned titanium sheets in 1:1:20 HF:H_2O_2:H_2O (by volume)

oxidizing solution for 10 seconds. Then, the samples were rinsed with de-ionized (DI) water and dried with nitrogen gas. For fabricating titania nanotubes, a two-electrode cell was used with the cleaned titanium sample as the anode and a platinum sheet as the cathode (Figure 5.2). The electrolyte was prepared by mixing 95% diethylene glycol with 2% hydrofluoric acid HF and 3% DI water. All experiments were carried out at room temperature, at 60 V for 24 h. After anodization, the samples were rinsed with isopropanol and dried with nitrogen gas. Subsequently, the substrates were annealed in oxygen ambient at 530° C for 6 h to obtain the titania nanotube arrays. Titania nanoflowers were fabricated as described in chapter three.
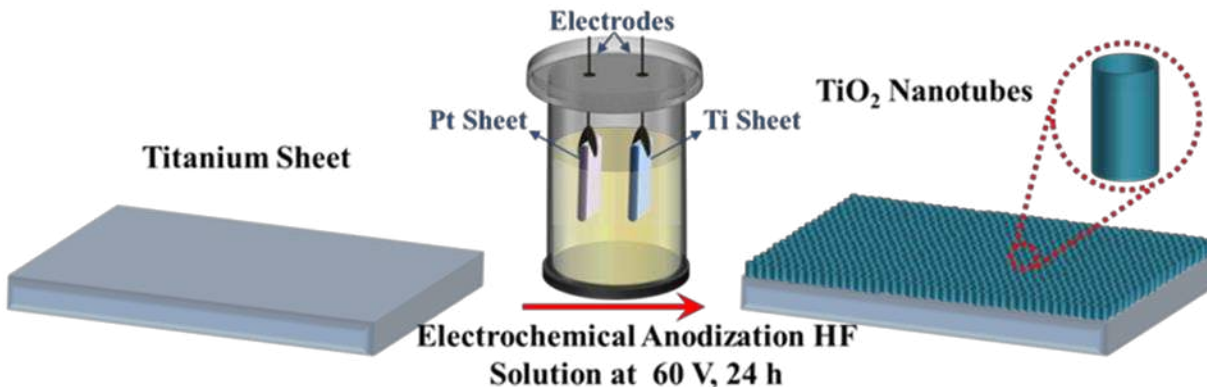
Figure 5.2. Schematic depicting the fabrication of titania nanotubes.

5.4. Surface Morphology, Surface Chemistry and Surface Wettability of Titania Surfaces

SEM images show the nearly smooth morphology of non-textured titania surfaces (Figure 5.3a), the textured morphology of titania nanoflowers with $2R \approx 1$ μm (Figure 5.3b) and the textured morphology of titania nanotubes with $2R \approx 0.25$ μm (Figure 5.3c). Subsequently, each titania morphology was left unmodified, PEGylated with a PEG silane and fluorinated with a fluorosilane. The titania surfaces were PEGylated via liquid phase silanization with 2 vol% 2-[Methoxy (Polyethyleneoxy) propyl] trimethoxysilane in ethanol for 24 h. The titania surfaces were fluorinated via vapor phase silanization with 200 μl of heptadecafluoro-1,1,2,2-

tetrahydrodecyl trichlorosilane at 120°C for 1 hour. We estimated the solid surface energy of our surfaces using Owens-Wendt analysis as described in chapter three. The solid surface energy of unmodified, PEGylated and fluorinated titania surfaces are γ_{sv} = 40 mN m^{-1}, γ_{sv} = 51 mN m^{-1} and γ_{sv} = 11 mN m^{-1}, respectively.
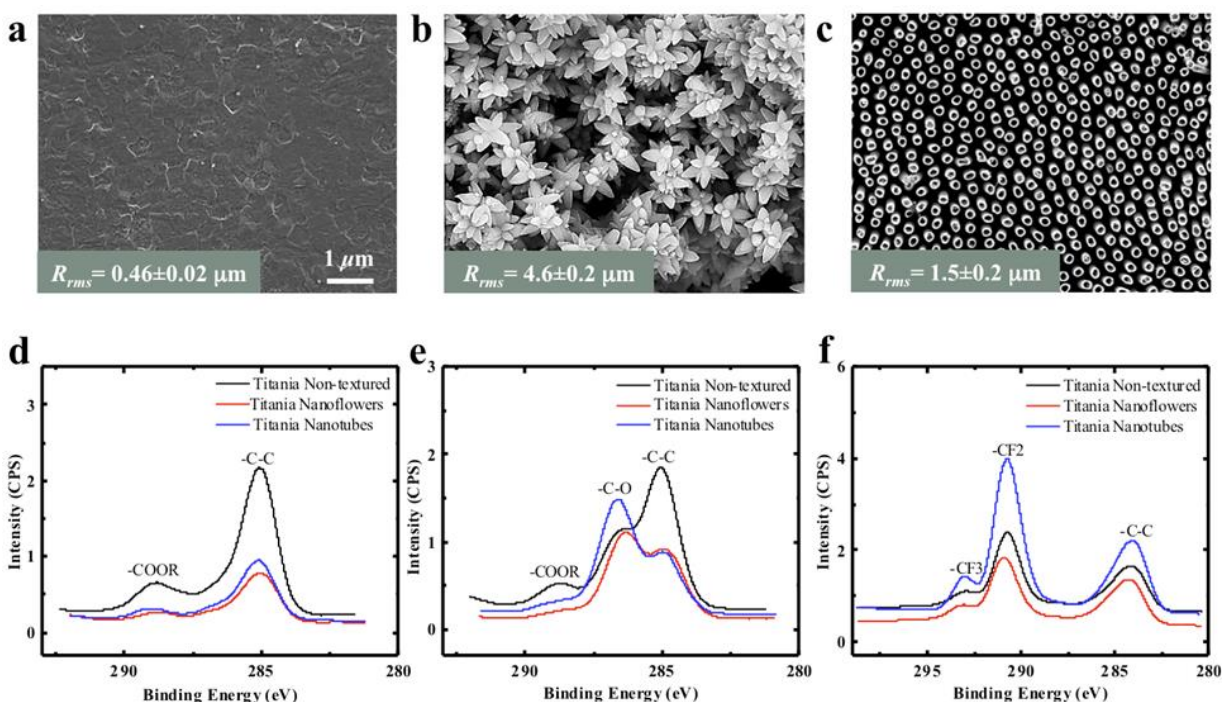
Figure 5.3. a), b) and c) SEM images showing the morphology of titania non-textured, titania nanoflowers and titania nanotubes, respectively. The root mean square roughness R_{rms} of each surface is shown. d), e) and f) High resolution C1s XPS spectra for unmodified, PEGylated and fluorinated titania surfaces, respectively.

We chose to PEGylate and fluorinate the surfaces because the steric repulsion induced by the water-soluble PEG layer[38-39] and the reduced interaction induced by the low solid surface energy of the fluorocarbons[40-42] are known to reduce platelet adhesion and activation. The high resolution C1s spectra (Figures 5.3d−5.3f) indicate the presence of the characteristic –CO groups on PEGylated surfaces[43] and the characteristic –CF$_2$ and –CF$_3$ groups on fluorinated surfaces.[44] We characterized the wettability of all titania surfaces (i.e., different morphologies and surface chemistries) by measuring the contact angles and roll off angles of human blood plasma in Table

5.1. The characterization techniques including optical profilometery, SEM, XPS and contact angle goniometry were performed as described in chapter three. Based on the contact angles, all unmodified and PEGylated surfaces (non-textured, nanoflowers and nanotubes) are hemophilic, fluorinated non-textured surfaces are hemophobic, and fluorinated nanoflower and fluorinated nanotube surfaces are superhemophobic. Human blood plasma droplets are in the Wenzel state on the unmodified nanoflower and nanotube surfaces and the PEGylated nanoflower and nanotube surfaces. In contrast, human blood plasma droplets are in the Cassie-Baxter state on the fluorinated nanoflower and nanotube surfaces and consequently, these surfaces are superhemophobic. As might be anticipated, on superhemophobic titania surfaces, blood droplets can easily roll off.

Table 5.1. Contact angles and roll off angles of human blood plasma on all the titania surfaces fabricated in this work. NR implies no roll off.

	Contact angles and roll off angles		
	Non-textured	Nanoflower	Nanotube
Unmodified	$\theta=61°$, NR Hemophilic	$\theta^*=25°$, NR Hemophilic	$\theta^*=30°$, NR Hemophilic
PEGylated	$\theta=31°$, NR Hemophilic	$\theta^*=20°$, NR Hemophilic	$\theta^*=18°$, NR Hemophilic
Fluorinated	$\theta=97°$, NR Hemophobic	$\theta^*=161°$, $\omega=7°$ Superhemophobic	$\theta^*=159°$, $\omega=5°$ Superhemophobic

5.5. Platelet Adhesion

After surface fabrication and characterized, the titania samples were sterilized and incubated for 2 h in human blood plasma. Whole blood was drawn from a healthy individual with care to avoid locally activated platelets and centrifuged in vials at 300g for 15 min to separate the human blood plasma from the erythrocytes. Sterilized titania surfaces (washed in 70% ethanol, then in

PBS and air dried) were incubated in 1 ml of the plasma in a 24-well plate at 37°C and 5% CO_2 on a horizontal shaker plate (100 rpm) for 2 h. After incubation of titania surfaces in human blood plasma, the unadhered platelets were removed by gently rinsing with PBS. Adhered platelets were fixed in a 3.7 wt % formaldehyde in PBS solution for 15 min and subsequently washed multiple times with PBS. The cell membranes were permeabilized using 1% Triton-X in PBS for 3 min. The titania surfaces were then incubated in PBS solutions containing 500 µl of rhodamine phalloidin (cytoskeleton red stain) for 25 min. The surfaces were subsequently rinsed with PBS and imaged using a fluorescence microscope (Zeiss). The % area of adhered platelets f_{adh} was obtained using ImageJ software. In order to evaluate the platelet adhesion, we measured the % area of adhered platelets f_{adh} using fluorescence microscopy (Figure 5.4a–5.4i). Among the non-textured titania surfaces (Figure 5.4a–5.4c), the PEGylated and the fluorinated surfaces resulted in a 5% and 10% lower f_{adh}, respectively, compared to the unmodified surfaces. The slightly lower f_{adh} on the PEGylated and the fluorinated surfaces is due to the steric repulsion induced by the water-soluble PEG layer and the reduced interaction induced by the low solid surface energy of the fluorocarbons, respectively. Among the unmodified titania surfaces (Figures 5.4a–5.4g), the nanoflower and nanotube surfaces resulted in 6% and 5% higher f_{adh}, respectively, compared to the non-textured surfaces. The slightly higher f_{adh} on the nanoflower and nanotube surfaces is due to the higher blood-solid interfacial area resulting from the Wenzel state. Similarly, among the PEGylated titania surfaces (Figures 5.4b–5.4h), the nanoflower and nanotube surfaces resulted in 10% and 7% higher f_{adh}, respectively, compared to the non-textured surfaces due to the higher blood-solid interfacial resulting from the Wenzel state. Among the fluorinated titania surfaces (Figures 5.4c–5.4i), the superhemophobic nanoflower and superhemophobic nanotube surfaces resulted in 15% and 67% lower f_{adh}, respectively, compared

74

to the non-textured surfaces. The lower f_{adh} on the superhemophobic nanoflower and superhemophobic nanotube surfaces is due to the lower blood-solid interfacial resulting from the Cassie-Baxter state.
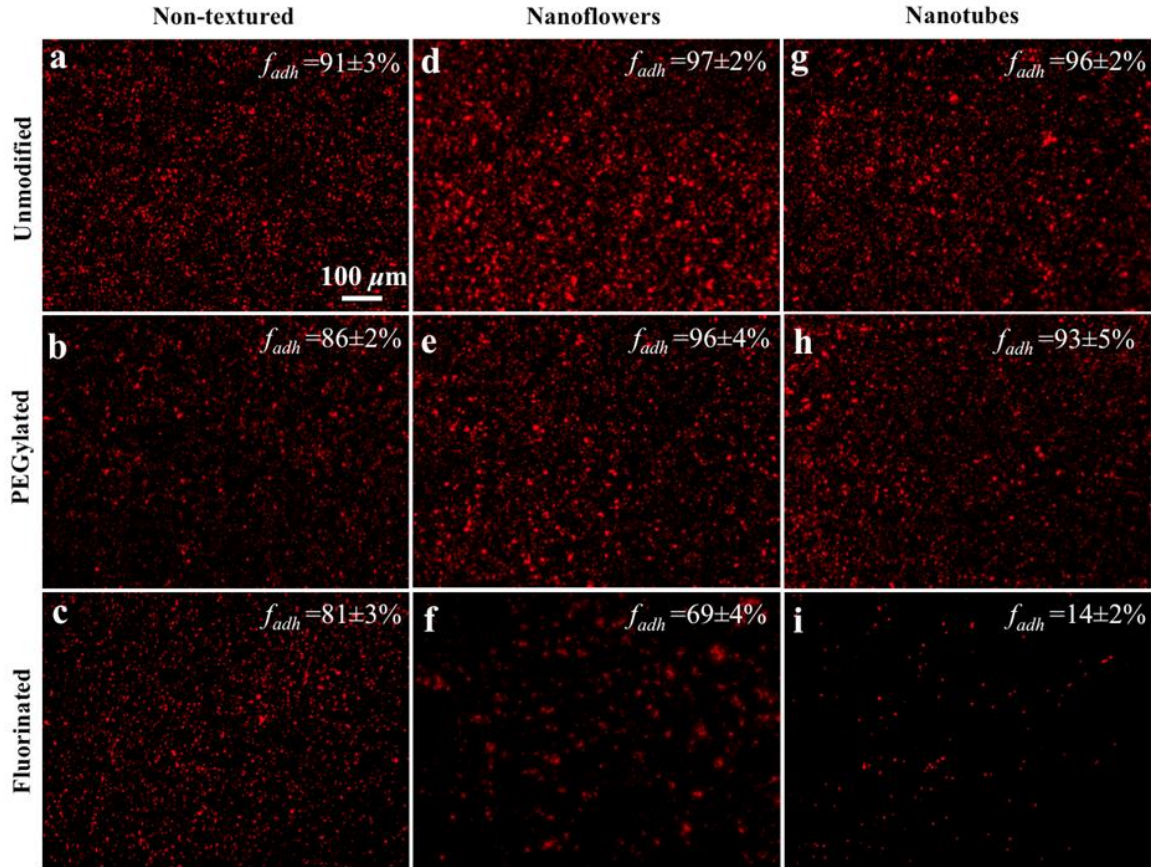
Figure 5.4. Fluorescence microscope images showing platelet adhesion for all the titania surfaces. a), b) and c) Unmodified, PEGylated and fluorinated non-textured surfaces, respectively. d), e) and f) Unmodified, PEGylated and fluorinated nanoflower surfaces, respectively. g), h) and i) Unmodified, PEGylated and fluorinated nanotube surfaces, respectively. Significant differences were observed between % area of adhered platelets on fluorinated non-textured, nanoflowers and nanotubes surfaces ($p \leq$ 0.05 at α=0.05).

5.6. Whole Blood Clotting

We compared the whole blood clotting on our hemophilic, hemophobic and superhemophobic surfaces by measuring the free hemoglobin concentration. In a typical experiment, whole human blood was drawn from a healthy individual, and 5 μL of the blood was immediately placed on unmodified non-textured, nanoflower and nanotube surfaces as well as

fluorinated non-textured, nanoflower and nanotube surfaces contained in a 48-well plate. The blood was allowed to clot on the surfaces for 15 min at room temperature. Subsequently, 500 μL of deionized water was added to each well. The surfaces were gently agitated for 30 s and left in DI water for 5 min to release free hemoglobin from red blood cells that were not trapped in the thrombus. To measure the free hemoglobin concentration, 200 μL of the solution in each well was then transferred into a 96-well plate. The absorbance of the solution with free hemoglobin was measured at a wavelength of 540 nm using a plate reader. The value of absorbance is directly proportional to the concentration of free hemoglobin in DI water and is an inverse measure of the degree of clotting.

Our results (see Table 5.2) indicate that the amount of free hemoglobin is slightly higher (i.e., blood clotting is slightly lower) for the fluorinated non-textured titania surfaces compared to the unmodified non-textured titania surfaces. Further, the amount of free hemoglobin on unmodified textured (i.e., nanoflower and nanotube) titania surfaces is lower (i.e., blood clotting is higher) compared to unmodified non-textured titania surfaces. Due to the superhemophobicity of the fluorinated nanoflower and fluorinated nanotube surfaces, blood droplets immediately rolled off and did not remain on these surfaces even when they are horizontal, possibly indicating low potential for blood clotting. However, rigorous blood clotting experiments via immersion could not be conducted because our substrates are not textured on all sides. These whole blood clotting results are consistent with our platelet adhesion and activation results. The platelet adhesion results are consistent with our whole blood clotting results. Among the superhemophobic surfaces, the nanoflower surfaces display significantly higher platelet adhesion compared to the nanotube surfaces. This will be discussed further later. In order to investigate platelet activation, the titania samples were sterilized and incubated for 2 h in human blood plasma and the fixed

surfaces were subsequently studied using a SEM. Prior to imaging the platelet activation, the incubated titania surfaces were gently rinsed with PBS to remove the unadhered platelets. The adhered platelets were first fixed in a primary fixative (6% glutaraldehyde, 0.1 M sodium cacodylate, and 0.1 M sucrose) for 45 min and then in a secondary fixative (primary fixative without glutaraldehyde) for 10 min. The surfaces were then dehydrated in consecutive solutions of ethanol (35%, 50%, 70%, and 100%) for 10 min each and finally in a solution of hexamethyldisilazane for 10 min. The surfaces were then air-dried and imaged.

Table 5.2. Free hemoglobin concentration (measured as absorbance) after clotting experiments on various surfaces.

Surface	Free hemoglobin conc. (measured as absorbance)	
	Before clotting	After clotting
Unmodified non-textured surface	3.0±0.2	0.6±0.1
Fluorinated non-textured surface	3.0±0.2	1.0±0.3
Unmodified nanoflower surface	3.0±0.2	0.5±0.2
Unmodified nanotube surface	3.0±0.2	0.5±0.2

5.7. Platelet Activation

Typically, platelet activation manifests as change in platelet shape, including dendritic extensions[6, 45] and platelet aggregation.[46-47] Our results indicate that all unmodified titania surfaces (Figures 5.5a−5.5g) display both dendritic extensions and aggregation. The PEGylated non-textured surfaces (Figure 5.5b) display aggregation, PEGylated nanoflower surfaces (Figure 5.5e) display dendritic extensions and the PEGylated nanotube surfaces (Figure 5.5h) display both dendritic extensions and aggregation. In other words, all hemophilic surfaces (Figures 5.5a−5.5b, Figures 5.5d−5.5e, Figures 5.5g−5.5h) display platelet activation. In addition, the

77

fluorinated non-textured hemophobic surfaces also display platelet activation via dendritic extensions and aggregation (Figure 5.5c). Among the superhemophobic surfaces, the fluorinated nanoflower surfaces (Figure 5.5f) display platelet activation via aggregation, but the fluorinated nanotube surfaces display no platelet activation.
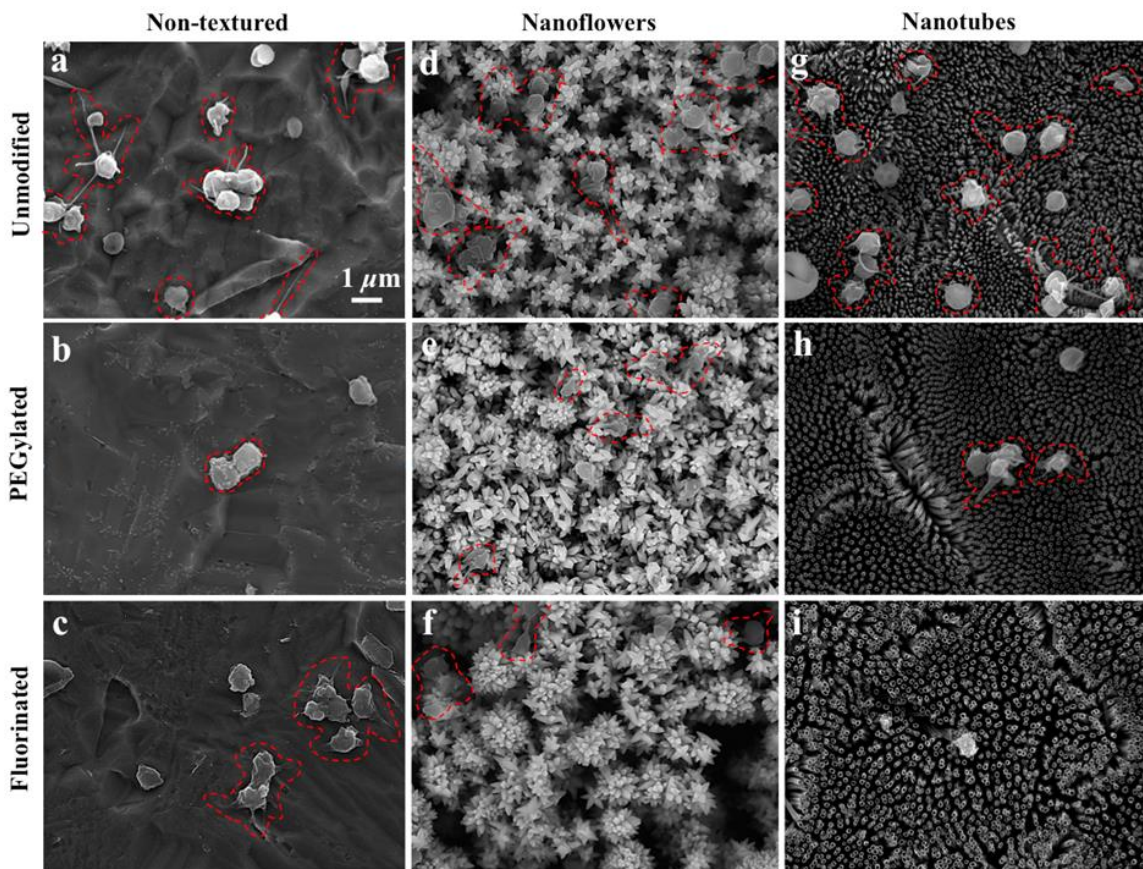
Figure 5.5. SEM images showing platelet activation (enclosed by dotted lines in red) on the titania surfaces. a), b) and c) Unmodified, PEGylated and fluorinated non-textured surfaces, respectively. d), e) and f) Unmodified, PEGylated and fluorinated nanoflower surfaces, respectively. g), h) and i) Unmodified, PEGylated and fluorinated nanotube surfaces, respectively.

5.8. Robustness Factor A^*

While both fluorinated nanoflower surfaces and fluorinated nanotube surfaces are superhemophobic, the fluorinated nanoflower surfaces display significantly higher platelet adhesion and activation compared to the fluorinated nanotube surfaces. This can be explained in terms of robustness of the Cassie-Baxter state for these two surfaces. The robustness factor A^* values for superhemophobic surfaces titania nanoflowers and titania nanotubes are calculated

using Equation 5-4. For human blood plasma, the density ρ = 1025 kg m^{-3} [48] and the surface tension γ_{lv} = 56mN m^{-1}.[18] For human blood plasma, we obtained the capillary length l_{cap} = 2.36 mm. We assumed that the Young's contact angle of human blood plasma on fluorinated titania surface is approximately equal to the static contact angle θ = 97° of human blood plasma on the non-textured fluorinated titania surface (see Table 5.1).
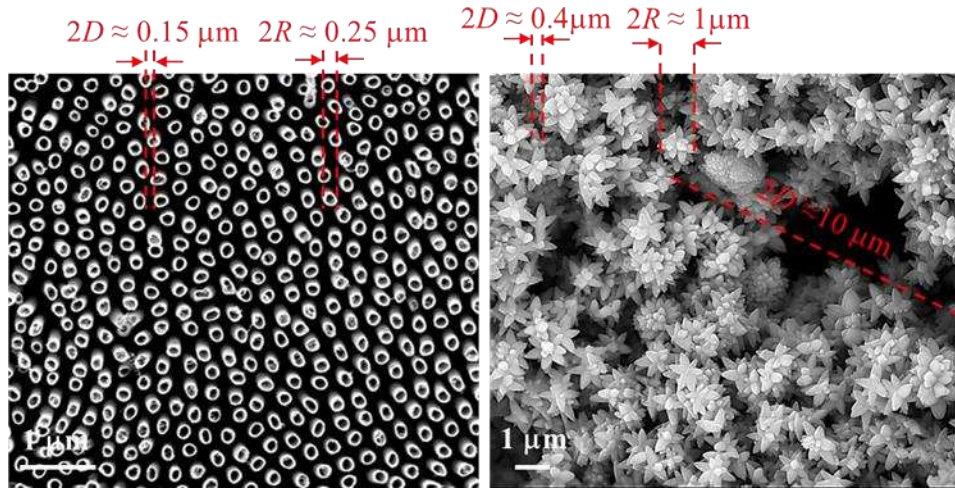
Figure 5.6. SEM images of – a) Titania nanotubes and b) Titania nanoflowers.

For titania nanotubes (Figure 5.6a), the feature size (i.e., nanotube diameter) $2R \approx 0.25$ μm and the inter-feature spacing $2D \approx 0.15$ μm. For titania nanoflowers (Figure 5.6b), the feature size (i.e., nanoflower diameter) $2R \approx 1$ μm, but there is a significant variation in the inter-feature spacing $2D \approx 0.4$ μm to 10 μm. Using the above listed values, we estimated the robustness factor A^* for superhemophobic titania nanotube and titania nanoflower surfaces (see Table 5.3).

For titania nanotubes, the feature size (i.e., nanotube diameter) $2R \approx 0.25$ μm and the inter-feature spacing $2D \approx 0.15$ μm, resulting in a highly robust Cassie-Baxter state for human blood plasma with $A^* \approx 815$. For titania nanoflowers, the feature size (i.e., nanoflower diameter) $2R \approx 1$ μm and the inter-feature spacing $2D \approx 0.4$ μm to 10 μm, resulting in $A^* \approx 266$ to 4. In other words, due to the large variation in the inter-feature spacing, there is a large variation in the

robustness of the Cassie-Baxter state for the fluorinated nanoflower surfaces. When such fluorinated nanoflower surfaces are subjected to shaking during incubation, the human blood plasma can easily breakthrough and transition from the Cassie-Baxter state to the Wenzel state in local pockets with low robustness (e.g., $A^* \approx 4$) of the Cassie-Baxter state. These local Wenzel states lead to higher blood-solid interfacial area and consequently higher platelet adhesion and activation for the fluorinated nanoflower surfaces compared to the fluorinated nanotube surfaces with a complete and robust Cassie-Baxter state. These results indicate that not all superhemophobic titania surfaces lead to significantly reduced platelet adhesion and activation. Further, our analysis indicates that only those superhemophobic surfaces with a robust Cassie-Baxter state display significantly lower platelet adhesion and activation compared to hemophobic and hemophilic surfaces.

Table 5.3. The estimated robustness parameter A^* for titania nanotubes and nanoflowers.

Texture	$2R$ (µm)	$2D$ (µm)	A^*
Nanotubes	0.25	0.15	815
Nanoflowers	1	0.4 to 10	266 to 4

5.9. Protein Adsorption

In collaboration with Dr. Popat research group, we have investigated the adsorption of human fibrinogen and human serum albumin on superhemophobic titania nanotube surfaces using XPS. Protein adsorption on sterilized substrates was characterized using the process described elsewhere.[1, 49] A precise way to characterize proteins adsorbed on the surface is to determine the contribution of N–C=O (amide) peak in the overall C 1s peak (Figure 5.7a). The results indicate that the unmodified titanium (Ti) had the highest fibrinogen adsorption, followed by unmodified nanotube arrays (NT) and superhemophobic nanotube surfaces (S-NT). The high-

resolution N 1s peak, which is characteristic to proteins as it is not inherently present on any surface, followed similar trend as that of N–C=O peak (Figure 5.7b). The albumin adsorption followed similar trend as that of fibrinogen adsorption with higher adsorption on Ti, followed by NT and S-NT.
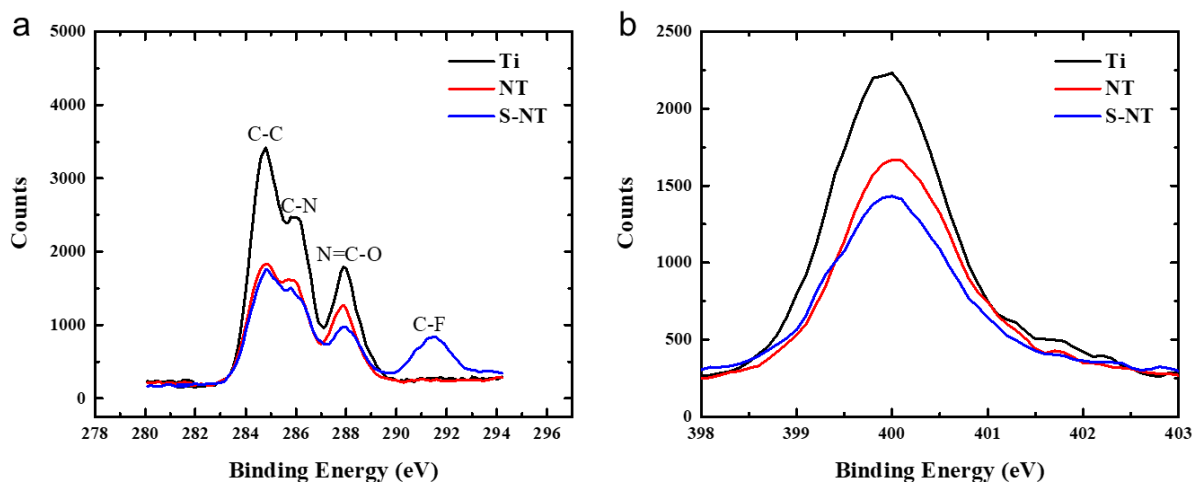
Figure 5.7. High resolution C 1s and N 1s scans for albumin adsorption on unmodified titanium (Ti), unmodified nanotube arrays (NT) and superhemophobic nanotube surfaces (S-NT).

5.10. Bacteria Adhesion

In collaboration with Dr. Popat research group, we have investigated the ability of superhydrophobic titania nanotube arrays to prevent initial gram-positive and gram-negative bacterial adhesion and further biofilm formation and have compared the results with unmodified titanium and unmodified nanotube arrays. Fluorescence microscopy was used to investigate the adhesion of *S. aureus* and *P. aeruginosa* bacteria to studied surfaces. The results for *S. aureus* indicated that the adhesion of live (green) and dead (red) bacteria was highest on Ti after 24 h of culture as compared to all other surfaces (Figure 5.8) followed by lower adhesion on NT surfaces ($p < 0.05$). Further, S-NT showed the least adhesion of *S. aureus* compared to all other surfaces after 6 and 24 h of culture (Figure 5.8; $p < 0.05$). Similar results were observed with *P. aeruginosa*. In addition, S-NT showed almost no biofilm formation after 24 h for *S. aureus* and *P. aeruginosa* bacteria. The reduction in bacteria adhesion on the S-NT can be attributed to the

reduced surface energy of the superhydrophobic surfaces along with their tendency to reduce protein adsorption to the surface which makes it more difficult for bacteria to adhere, reducing adhesion and making it easier to remove those that do attach.[51-53]
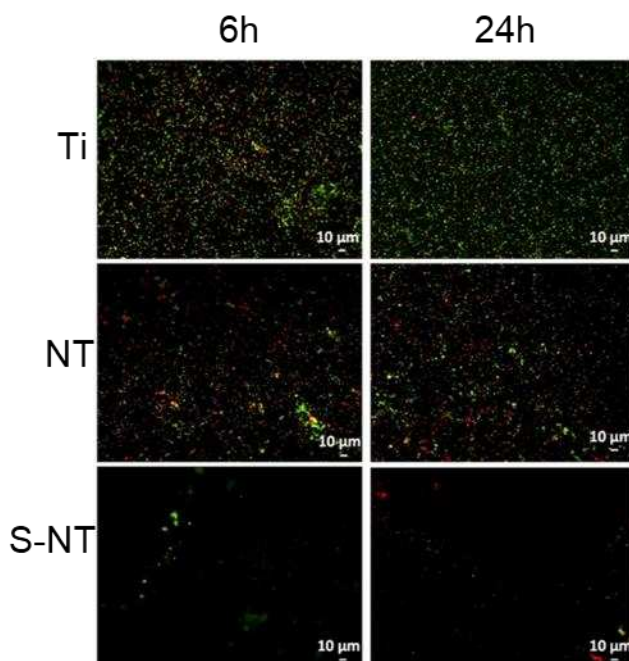
Figure 5.8. Representative fluorescence microscopy images of *S. aureus* on different surfaces after 6 h and 24 h of culture. Green stain represents live bacteria and red stain represents dead bacteria.

5.11. Conclusions

In summary, we fabricated hemophilic, hemophobic and superhemophobic titania surfaces by employing three different morphologies – non-textured, nanoflowers and nanotubes – and for each morphology, three different surface chemistries – unmodified, PEGylated and fluorinated. For each of our titania surfaces, we characterized the wettability using contact angle goniometry, the surface chemistry using XPS, and platelet adhesion and activation using fluorescence microscopy and SEM. Our results indicate that although the protein adsorption and platelet adhesion and activation is reduced on superhemophobic surfaces, not all superhemophobic titania surfaces lead to significantly reduced platelet adhesion and activation. Our analysis indicates that only those superhemophobic surfaces with a robust Cassie-Baxter state display

significantly lower platelet adhesion and activation compared to hemophobic and hemophilic surfaces. Further, the bacteria adhesion and biofilm formation on superhydrophobic titania nanotube surfaces were lower compared to unmuddied titanium and unmodified nanotube arrays. We envision that the understanding gained through this work will lead to the fabrication of improved hemocompatible, superhemophobic medical implants.

REFERENCES

(1) Leszczak, V.; Smith, B. S.; Popat, K. C. Hemocompatibility of polymeric nanostructured surfaces. *Journal of Biomaterials Science, Polymer Edition* **2013,** *24*, 1529-1548.

(2) Tang, L.; Hu, W. Molecular determinants of biocompatibility. *Expert review of medical devices* **2005,** *2*, 493-500.

(3) Spijker, H. T.; Bos, R.; Busscher, H. J.; van Kooten, T. G.; van Oeveren, W. Platelet adhesion and activation on a shielded plasma gradient prepared on polyethylene. *Biomaterials* **2002,** *23*, 757-766.

(4) Koh, L. B.; Rodriguez, I.; Venkatraman, S. S. A novel nanostructured poly (lactic-co-glycolic-acid)–multi-walled carbon nanotube composite for blood-contacting applications: Thrombogenicity studies. *Acta biomaterialia* **2009,** *5*, 3411-3422.

(5) Huang, N.; Yang, P.; Leng, Y.; Chen, J.; Sun, H.; Wang, J.; Wang, G.; Ding, P.; Xi, T.; Leng, Y. Hemocompatibility of titanium oxide films. *Biomaterials* **2003,** *24*, 2177-2187.

(6) Smith, B. S.; Yoriya, S.; Grissom, L.; Grimes, C. A.; Popat, K. C. Hemocompatibility of titania nanotube arrays. *Journal of Biomedical Materials Research Part A* **2010,** *95*, 350-360.

(7) Liu, H.; Zhai, J.; Jiang, L. Wetting and anti-wetting on aligned carbon nanotube films. *Soft Matter* **2006,** *2*, 811-821.

(8) Sun, T.; Tan, H.; Han, D.; Fu, Q.; Jiang, L. No platelet can adhere—largely improved blood compatibility on nanostructured superhydrophobic surfaces. *Small* **2005,** *1*, 959-963.

(9) Chen, L.; Liu, M.; Bai, H.; Chen, P.; Xia, F.; Han, D.; Jiang, L. Antiplatelet and thermally responsive poly (N-isopropylacrylamide) surface with nanoscale topography. *Journal of the American Chemical Society* **2009,** *131*, 10467-10472.

(10) Thevenot, P.; Hu, W.; Tang, L. Surface chemistry influence implant biocompatibility. *Current topics in medicinal chemistry* **2008,** *8*, 270.

(11) Nonckreman, C. J.; Fleith, S.; Rouxhet, P. G.; Dupont-Gillain, C. C. Competitive adsorption of fibrinogen and albumin and blood platelet adhesion on surfaces modified with nanoparticles and/or PEO. *Colloids and Surfaces B: Biointerfaces* **2010,** *77*, 139-149.

(12) Khorasani, M.; Mirzadeh, H. In vitro blood compatibility of modified PDMS surfaces as superhydrophobic and superhydrophilic materials. *Journal of applied polymer science* **2004,** *91*, 2042-2047.

(13) Zhou, M.; Yang, J. H.; Ye, X.; Zheng, A. R.; Li, G.; Yang, P. F.; Zhu, Y.; Cai, L. In *Blood Platelet's behavior on nanostructured superhydrophobic surface*, Journal of Nano Research, Trans Tech Publ: 2008; pp 129-136.

(14) Mao, C.; Liang, C.; Luo, W.; Bao, J.; Shen, J.; Hou, X.; Zhao, W. Preparation of lotus-leaf-like polystyrene micro-and nanostructure films and its blood compatibility. *Journal of Materials Chemistry* **2009,** *19*, 9025-9029.

(15) Bark Jr, D. L.; Vahabi, H.; Bui, H.; Movafaghi, S.; Moore, B.; Kota, A. K.; Popat, K.; Dasi, L. P. Hemodynamic Performance and Thrombogenic Properties of a Superhydrophobic Bileaflet Mechanical Heart Valve. *Annals of biomedical engineering* **2016**, 1-12.

(16) Lafuma, A.; Quéré, D. Superhydrophobic states. *Nature materials* **2003,** *2*, 457-460.

(17) Nosonovsky, M.; Bhushan, B. Superhydrophobic surfaces and emerging applications: non-adhesion, energy, green engineering. *Current Opinion in Colloid & Interface Science* **2009,** *14*, 270-280.

(18) Hrncir, E.; Rosina, J. Surface tension of blood. *Physiological research/Academia Scientiarum Bohemoslovaca* **1996,** *46*, 319-321.

(19) Huang, Q.; Yang, Y.; Hu, R.; Lin, C.; Sun, L.; Vogler, E. A. Reduced platelet adhesion and improved corrosion resistance of superhydrophobic TiO 2-nanotube-coated 316L stainless steel. *Colloids and Surfaces B: Biointerfaces* **2015,** *125*, 134-141.

(20) Jiang, J.; Xu, J.; Liu, Z.; Deng, L.; Sun, B.; Liu, S.; Wang, L.; Liu, H. Preparation, corrosion resistance and hemocompatibility of the superhydrophobic TiO 2 coatings on biomedical Ti-6Al-4V alloys. *Applied Surface Science* **2015,** *347*, 591-595.

(21) Yang, Y.; Lai, Y.; Zhang, Q.; Wu, K.; Zhang, L.; Lin, C.; Tang, P. A novel electrochemical strategy for improving blood compatibility of titanium-based biomaterials. *Colloids and Surfaces B: Biointerfaces* **2010,** *79*, 309-313.

(22) Cassie, A.; Baxter, S. Wettability of porous surfaces. *Transactions of the Faraday Society* **1944,** *40*, 546-551.

(23) Kota, A. K.; Kwon, G.; Tuteja, A. The design and applications of superomniphobic surfaces. *NPG Asia Materials* **2014,** *6*, e109.

(24) Nakajima, A.; Hashimoto, K.; Watanabe, T. Recent studies on super-hydrophobic films. *Monatshefte für Chemie/Chemical Monthly* **2001,** *132*, 31-41.

(25) Patankar, N. A. On the modeling of hydrophobic contact angles on rough surfaces. *Langmuir* **2003,** *19*, 1249-1253.

(26) Gao, L.; McCarthy, T. J. The "lotus effect" explained: two reasons why two length scales of topography are important. *Langmuir* **2006,** *22*, 2966-2967.

(27) Erbil, H. Y.; Demirel, A. L.; Avci, Y.; Mert, O. Transformation of a simple plastic into a superhydrophobic surface. *Science* **2003,** *299*, 1377-1380, DOI: 10.1126/science.1078365.

(28) Choi, W.; Tuteja, A.; Mabry, J. M.; Cohen, R. E.; McKinley, G. H. A modified Cassie–Baxter relationship to explain contact angle hysteresis and anisotropy on non-wetting textured surfaces. *Journal of colloid and interface science* **2009,** *339*, 208-216.

(29) Kota, A. K.; Mabry, J. M.; Tuteja, A. Superoleophobic surfaces: design criteria and recent studies. *Surface Innovations* **2013,** *1*, 71-83.

(30) Giacomello, A.; Meloni, S.; Chinappi, M.; Casciola, C. M. Cassie–Baxter and Wenzel states on a nanostructured surface: phase diagram, metastabilities, and transition mechanism by atomistic free energy calculations. *Langmuir* **2012,** *28*, 10764-10772.

(31) Murakami, D.; Jinnai, H.; Takahara, A. Wetting transition from the Cassie–Baxter state to the Wenzel state on textured polymer surfaces. *Langmuir* **2014,** *30*, 2061-2067.

(32) Kota, A. K.; Li, Y.; Mabry, J. M.; Tuteja, A. Hierarchically structured superoleophobic surfaces with ultralow contact angle hysteresis. *Advanced Materials* **2012,** *24*, 5838-5843.

(33) Tuteja, A.; Choi, W.; Mabry, J. M.; McKinley, G. H.; Cohen, R. E. Robust omniphobic surfaces. *Proceedings of the National Academy of Sciences* **2008,** *105*, 18200-18205.

(34) Zhang, Y.; Wang, C. Micropatterning of Proteins on 3D Porous Polymer Film Fabricated by Using the Breath-Figure Method. *Advanced Materials* **2007,** *19*, 913-916.

(35) Gao, L.; McCarthy, T. J. How Wenzel and Cassie were wrong. *Langmuir* **2007,** *23*, 3762-3765.

(36) Williams, K. R.; Muller, R. S. Etch rates for micromachining processing. *Journal of microelectromechanical systems* **1996,** *5*, 256-269.

(37) Wu, G.; Wang, J.; Thomas, D. F.; Chen, A. Synthesis of F-doped flower-like TiO2 nanostructures with high photoelectrochemical activity. *Langmuir* **2008,** *24*, 3503-3509.

(38) Amiji, M.; Park, K. Surface modification of polymeric biomaterials with poly (ethylene oxide), albumin, and heparin for reduced thrombogenicity. *Journal of Biomaterials Science, Polymer Edition* **1993,** *4*, 217-234.

(39) Zhang, M.; Ferrari, M. Hemocompatible polyethylene glycol films on silicon. *Biomedical Microdevices* **1998,** *1*, 81-89.

(40) Lin, J.-C.; Tiong, S.-L.; Chen, C.-Y. Surface characterization and platelet adhesion studies on fluorocarbons prepared by plasma-induced graft polymerization. *Journal of Biomaterials Science, Polymer Edition* **2000,** *11*, 701-714.

(41) Wang, S.; Gupta, A. S.; Sagnella, S.; Barendt, P. M.; Kottke-Marchant, K.; Marchant, R. E. Biomimetic fluorocarbon surfactant polymers reduce platelet adhesion on PTFE/ePTFE surfaces. *Journal of Biomaterials Science, Polymer Edition* **2009,** *20*, 619-635.

(42) Jahangir, A.; McClung, W.; Cornelius, R.; McCloskey, C.; Brash, J.; Santerre, J. Fluorinated surface-modifying macromolecules: Modulating adhesive protein and platelet interactions on a polyether-urethane. *J. of Bbiomedical Materials Research* **2002,** *60*, 135-147.

(43) Sharma, S.; Johnson, R. W.; Desai, T. A. XPS and AFM analysis of antifouling PEG interfaces for microfabricated silicon biosensors. *Biosensors and Bioelectronics* **2004,** *20*, 227-239.

(44) Kassis, C. M.; Steehler, J. K.; Betts, D. E.; Guan, Z.; Romack, T. J.; DeSimone, J. M.; Linton, R. W. XPS studies of fluorinated acrylate polymers and block copolymers with polystyrene. *Macromolecules* **1996,** *29*, 3247-3254.

(45) Yip, J.; Shen, Y.; Berndt, M. C.; Andrews, R. K. Primary platelet adhesion receptors. *IUBMB life* **2005,** *57*, 103-108.

(46) Ashby, B.; Daniel, J.; Smith, J. Mechanisms of platelet activation and inhibition. *Hematology/oncology clinics of North America* **1990,** *4*, 1-26.

(47) Davì, G.; Patrono, C. Platelet activation and atherothrombosis. *New England Journal of Medicine* **2007,** *357*, 2482-2494.

(48) Neofytou, P. Comparison of blood rheological models for physiological flow simulation. *Biorheology* **2004,** *41*, 693-714.

(49) Bartlet, K.; Movafaghi, S.; Kota, A.; Popat, K. C. Superhemophobic titania nanotube array surfaces for blood contacting medical devices. *RSC Advances* **2017,** *7*, 35466-35476.

(50) Bartlet, K.; Movafaghi, S.; Dasi, L. P.; Kota, A. K.; Popat, K. C. Antibacterial activity on superhydrophobic titania nanotube arrays. *Colloids and Surfaces B: Biointerfaces* **2018,** *166*, 179-186.

(51) Zhang, X.; Wang, L.; Levänen, E. Superhydrophobic surfaces for the reduction of bacterial adhesion. *Rsc Advances* **2013,** *3*, 12003-12020.

(52) Tang, P.; Zhang, W.; Wang, Y.; Zhang, B.; Wang, H.; Lin, C.; Zhang, L. Effect of superhydrophobic surface of titanium on staphylococcus aureus adhesion. *Journal of Nanomaterials* **2011,** *2011*, 2.

(53) Zhu, H.; Guo, Z.; Liu, W. Adhesion behaviors on superhydrophobic surfaces. *Chemical Communications* **2014,** *50*, 3900-3913.

CHAPTER 6 – INFLUENCE OF SUPERHYDROPHOBIC RIDGE GEOMETRY ON THE CRITICAL SPLITTING HEIGHTS OF WATER DROPLETS

Summary: In this work, we demonstrated that for each ridge angle, as the ridge height increases the critical splitting height decreases. However, this reduction turns into a plateau beyond a certain ridge height which is a function of droplet volume, because the two lobes of droplet do not touch the flat surfaces anymore. Further, our results indicate that a water droplet impacting a superhydrophobic ridge splits when $We_c \sim O(1)$, regardless of the ridge geometry (**manuscript under preparation for Journal of Fluid Mechanics**).

6.1. Introduction

In recent years, several studies have investigated the impingement of liquid droplets on superhydrophobic surfaces and the dynamic behavior of droplets upon interaction with such surfaces.[1-8] The interaction of superhydrophobic surfaces with impinging droplets is governed by physics and chemistry of the surface (e.g., surface wettability, surface topography, surface modulus, surface charge, surface temperature etc.), the properties of impinging liquid (e.g., surface tension, density, viscosity, volume etc.) as well as the impinging velocity of the droplet.[4, 9-11] It has been shown that tuning the interaction of superhydrophobic surfaces with impinging droplets can lead to different dynamic behavior of droplets such as droplet bouncing off the surface,[5, 12-13] pancake bouncing,[14-15] droplet breaking,[16] droplet splitting,[17-19] droplet splashing[20] or even sticking[12, 20] to the surface. Based on the dynamic behavior of the droplet upon impinging the superhydrophobic surfaces, various potential applications such as self-cleaning, anti-icing, microfluidics etc. have been suggested.[12, 21]

One of the dynamic behaviors of impinging droplets is droplet splitting upon impinging a superhydrophobic ridge like structures (nano- or micro-texture) or wires on a flat surface,[17-18, 22-23] or superhydrophobic/hydrophilic patterned stripes.[19, 24] Among the prior work on droplet splitting, a few reports have shown that a water droplet can split into two smaller droplets after hitting the superhydrophobic ridge and reported that such splitting leads to reduced water-solid contact time by about 40%.[17-18] Such reduction in droplet-solid contact time is important because it can prevent droplets from freezing when contacting cold surfaces (e.g., preventing the formation of ice from rain droplets). However, to the best of our knowledge, there are no scaling analyses to predict the critical splitting height (i.e., the height above which splitting occurs) for liquid droplets on superhydrophobic surfaces. Further, the influence of the ridge geometry (i.e., ridge height and ridge angle) on the splitting height of liquid droplets hitting a macroscopic ridge has not been investigated. In this work, we have studied the critical splitting height of water droplets impacting a superhydrophobic macroscopic ridge on a flat surface. We demonstrated that for each ridge angle, as the ridge height increases the critical splitting height decreases. However, this reduction turns into a plateau beyond a certain ridge height which is a function of droplet volume, because the two lobes of droplet do not touch the flat surfaces anymore. Further, our results indicate that a water droplet impacting a superhydrophobic ridge splits when $We_c \sim$ O(1), regardless of the ridge geometry.

6.2. Droplet Splitting – Theory

When a liquid droplet impacts a superhydrophobic ridge, the droplet splits if the inertial forces (or kinetic energy) of the impacting droplet can overcome the surface tension forces (or surface energy expended in deforming a droplet) and the viscous forces (or viscous dissipation). The energy balance can be represented as follows:

$$\rho R^3 V_c^2 \sim \gamma R^2 + \mu V_c R^2 \tag{6-1}$$

Here, ρ, γ and μ are density, surface tension and viscosity of the liquid, respectively. R is the radius of liquid droplet. V_c is the critical initial velocity of the liquid droplet at which splitting occurs and will be calculated using $V_c = \sqrt{2gH_c}$, g and H_c being the acceleration due to gravity and critical splitting height, respectively. The term on the left-hand side represents the kinetic energy. The first term on the right-hand side represents the surface energy and the second term represents the viscous dissipation. Equation 6-1 can be rewritten in a non-dimension form, as follows:

$$\frac{\rho R V_c^2}{\gamma} \sim 1 + \frac{\mu V_c}{\gamma} \tag{6-2}$$

$$We_c \sim 1 + Ca_c \tag{6-3}$$

Here, We_c, is the critical Weber number at which splitting occurs, $We_c = \dfrac{\rho R V_c^2}{\gamma}$ and Ca_c is the critical capillary number at which splitting occurs, $Ca_c = \dfrac{\mu V_c}{\gamma}$. In all the experiments we have conducted with water impacting a superhydrophobic ridge, the capillary number is negligible, Ca < 0.01. Consequently, the energy balance shown in equation 6-3 simplifies as:

$$We_c \sim 1 \tag{6-4}$$

Therefore, based on equation 6-4, droplet splitting is anticipated to occur when $We_c \sim O(1)$.

6.3. Fabrication of Superhydrophobic Ridges

In this work, we fabricated superhydrophobic surfaces by spray coating the substrates with fluorinated SiO_2 particles. 300 mg of fumed silica particles (diameter ~7 nm; Sigma Aldrich) were functionalized in a solution consisting of 10 mL n-Hexane (Fisher) and 0.3 mL heptadecafluoro-1,1,2,2-tetrahydrodecyl trichlorosilane (Gelest) for three days to form a suspension of fluorinated silica (F-SiO_2) particles. To fabricate the superhydrophobic surface, first, a glue layer (Gorilla glue; polyurethane adhesives) was spin coated on the ridge at 5000 rpm for 120 s to make sure a very thin layer of adhesive was distributed on the ridge (Figure 6.1a). Immediately after spin coating of the adhesive layer (i.e., before adhesive layer was dried), the suspension of F-SiO_2 particles was spray coated on the adhesive layer (Figure 6.1b). Spray coating was done at a pressure of 30 psi using an air brush (Paasche) held 10 cm from the surface (Figure 6.1b). The surface was then allowed to dry at room temperature. The resulting surfaces was superhydrophobic to water droplets (Figure 6.1c). Further, we used SEM to assess the surface morphology and uniformity of the coating (Figure 6.1d).

In order to investigate the influence of ridge geometry on critical splitting height, we fabricated ridges with different angles on aluminum bars (6061 aluminum alloy) using a belt grinder. We chose aluminum as our substrate due to the ease of machining.[25] In order to systematically investigate the influence of ridge angle α_r on critical splitting height H_c, we fabricated ridges with angles of 35°, 70°, 90°, 115° and 140°. For each ridge angle α_r, different ridge heights h_r were achieved using a simple set-up shown in figure 6.2. In this set-up, the ridge was placed on a micrometer jack, and two sharp angles flat aluminum sheets (fabricated with a CNC machine and an angled cutter) were placed on two stands on the either sides of the ridge, in

contact with the ridge (Figure 6.2). We ensured that there is no gap between the ridge and the flat sheets.
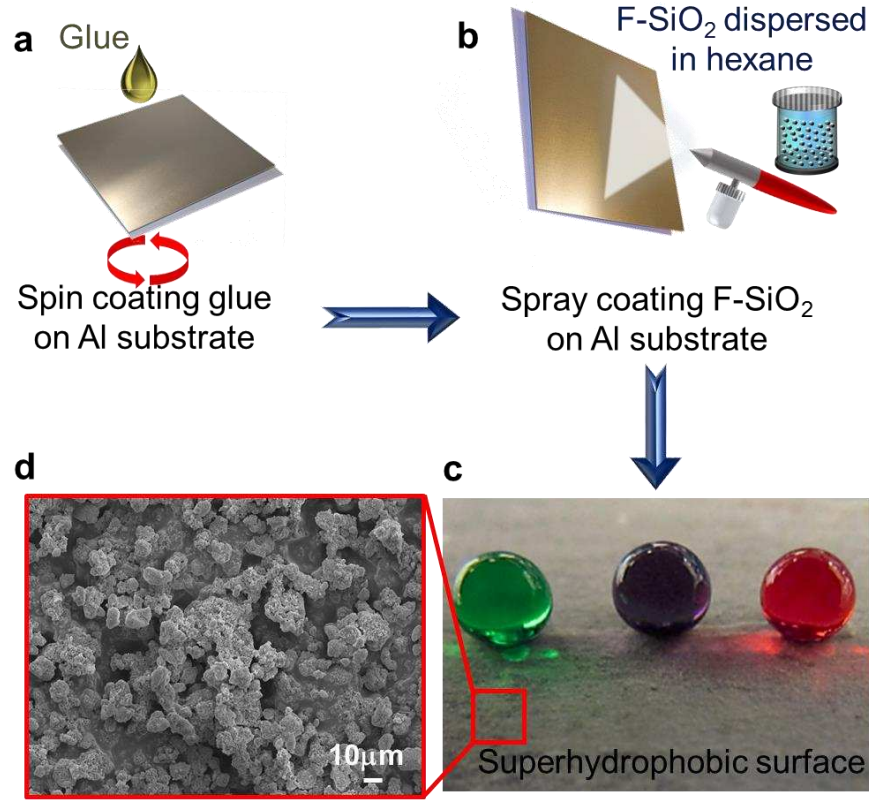
Figure 6.1. Schematic illustrating the fabrication of a superhydrophobic surface. The superhydrophobic surface was fabricated by first, a) spin coating of a glue layer on substrate, followed by b) spray coating F-SiO$_2$ particles on the substrate with a glue layer. c) Colored water droplets can easily bead up on superhydrophobic surface. d) SEM image indicates the surface morphology of the superhydrophobic surface.

In our set-up, the micrometer jack enables the moving of the ridge vertically and precise control over the ridge height. In order to systematically investigate the influence of ridge height h_r on the critical splitting height H_c of a droplet, we conducted experiments at 0.5, 1, 1.5, 2, 2.5, and 3 mm ridge heights. Based on the droplet volume (10 μl), the effect of ridge heights h_r higher than 3 mm on critical splitting height H_c is anticipated to be negligible because the droplet lobes cannot reach the flat sheets anymore. We utilized a syringe pump to dispense liquid droplets with consistent volume to minimize the influence of volume variation on the results

(Figure 6.2). The volume of liquid droplets was kept constant at 10 μl. Also, the syringe pump was placed on an adjustable stage to enable controlling the initial droplet height H. Each ridge and flat substrates were then spray coated with F-SiO$_2$ particles to become superhydrophobic.
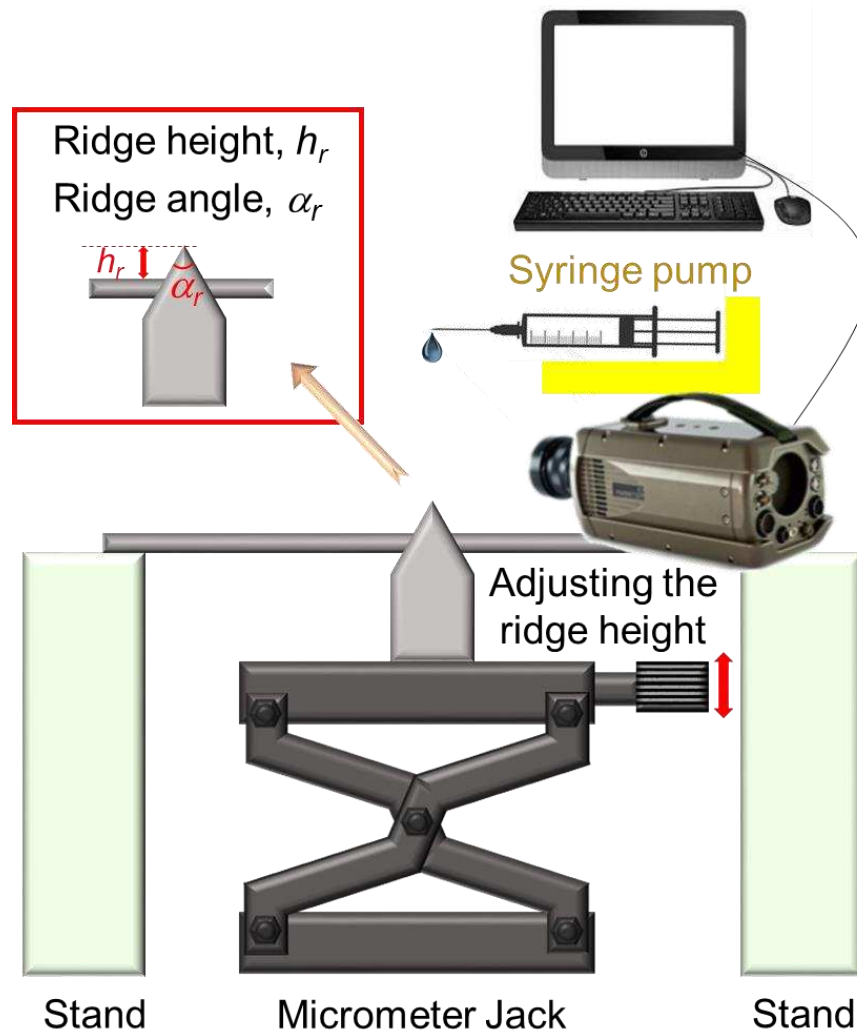
Figure 6.2. Schematic illustrating the experimental set-up. The triangular prism-like ridge and flat substrates enable controlling the ridge height.

6.4. Droplet Splitting - Experiments

After fabricating the superhydrophobic ridges and flat sheets and establishing the experimental set-up, we utilized a high-speed camera (Photron FASTCAM SA3) to capture the liquid droplets hitting on the ridge (Figure 6.2.). The videos were recorded at 2000 frames per

second and 640x640 resolution to ensure that the droplet impact dynamics are captured with sufficient time and spatial resolution for further analysis. Two light sources were used to provide the movies with proper light and prevent any possible shadows. The high-speed camera was placed at the same level and perpendicular to the ridge set-up to eliminate any possible errors resulting from the camera angle. The calibration of videos was conducted by capturing pictures of a ruler held at the same place that the experiments occur. The movies were analyzed using PFV Ver.3641 software to measure precise splitting heights H.
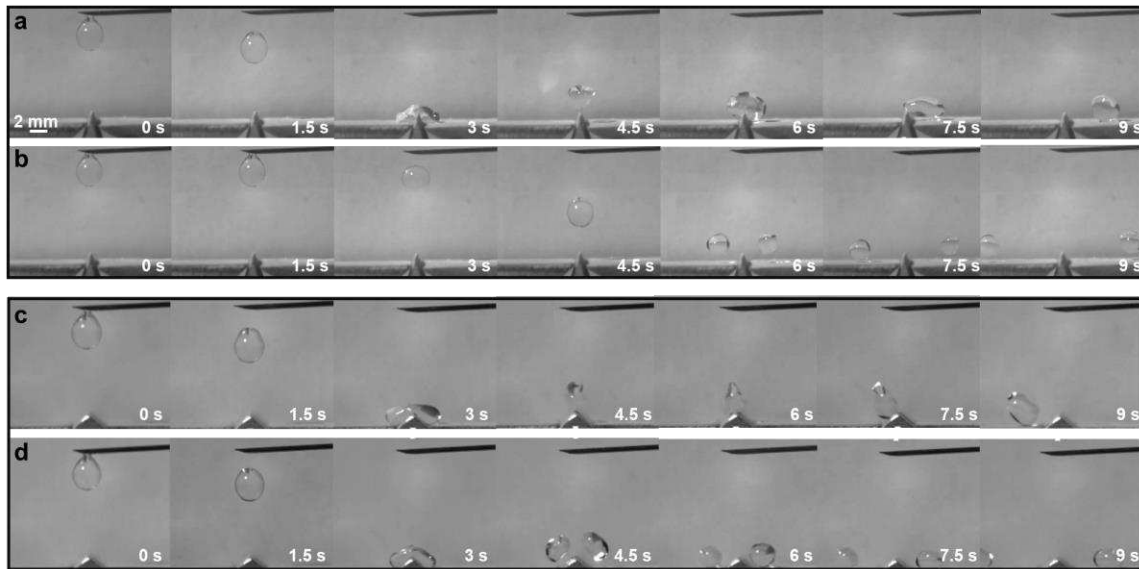

Figure 6.3. 10 µl water droplets hitting a macroscopic ridge on a superhydrophobic surface. Water droplet a) bouncing back as a single droplet after hitting the ridge with $H = 6.24$ mm, $We = 2.3$ and b) splitting into two droplets after hitting the ridge with $H_c = 6.58$ mm, $We_c = 2.4$, on the same ridge with $\alpha_r = 35°$, $h_r = 1$ mm. Water droplet c) bouncing back as a single droplet after hitting the ridge with $H = 5.64$ mm, $We = 2.1$ and d) splitting into two droplets after hitting the ridge with $H_c = 5.97$ mm, $We_c = 2.2$, on the same ridge with $\alpha_r = 90°$, $h_r = 1$ mm.

Utilizing superhydrophobic macroscopic ridges on flat surfaces, we systematically investigated the critical splitting heights H_c of 10 µl water droplets on ridges with different geometries. First, the splitting of water droplets on superhydrophobic macroscopic ridges on flat surfaces with same ridge height h_r, but different ridge angle α_r is demonstrated in figure 6.3. For

example, on the superhydrophobic macroscopic ridge on flat surface with $\alpha_r = 35°$ and $h_r = 1$ mm, for a releasing height of $H = 6.24$ mm above the ridge (corresponding to $We = 2.3$), the water droplet bounces back as a single droplet after hitting the ridge (Figure 6.3a), while on the same ridge but for a higher releasing height (critical releasing height) $H_c = 6.58$ mm above the ridge (corresponding to $We_c = 2.4$), water droplet splits into two smaller droplets after hitting the ridge (Figure 6.3b). As another example, on the superhydrophobic macroscopic ridge on flat surface with $\alpha_r = 90°$ and $h_r = 1$ mm, for a releasing height of $H = 5.64$ mm above the ridge (corresponding to $We = 2.1$), the water droplet bounces back as a single droplet after hitting the ridge (Figure 6.3c), while on the same ridge but for a higher releasing height (critical releasing height) $H_c = 5.97$ mm above the ridge (corresponding to $We_c = 2.2$), water droplet splits into two smaller droplets after hitting the ridge (Figure 6.3d). In this manner, the critical splitting height H_c and critical Weber number We_c were determined for different ridge heights h_r of each ridge angle α_r.

Second, we demonstrated the splitting of water droplets on superhydrophobic macroscopic ridges on flat surfaces with same ridge angle α_r, but different ridge height h_r, in figure 6.4. For example, on the superhydrophobic macroscopic ridge on flat surface with $\alpha_r = 70°$ and $h_r = 0.5$ mm, for a releasing height of $H = 9.74$ mm above the ridge (corresponding to $We = 3.6$), the water droplet bounces back as a single droplet after hitting the ridge (Figure 6.4a), while on the same ridge but for a higher releasing height (critical releasing height) $H_c = 9.88$ mm above the ridge (corresponding to $We_c = 3.7$), water droplet splits into two smaller droplets after hitting the ridge (Figure 6.4b). As another example, on the superhydrophobic macroscopic ridge on flat surface with $\alpha_r = 70°$ and $h_r = 1$ mm, for a releasing height of $H = 5.69$ mm above the ridge (corresponding to $We = 2.1$), the water droplet bounces back as a single droplet after hitting the

ridge (Figure 6.4c), while on the same ridge but for a higher releasing height (critical releasing height) $H_c = 5.92$ mm above the ridge (corresponding to $We_c = 2.2$), water droplet splits into two smaller droplets after hitting the ridge (Figure 6.4d). As previously mentioned, the critical splitting height H_c and critical Weber number We_c were determined for different ridge heights h_r and different ridge angles α_r.
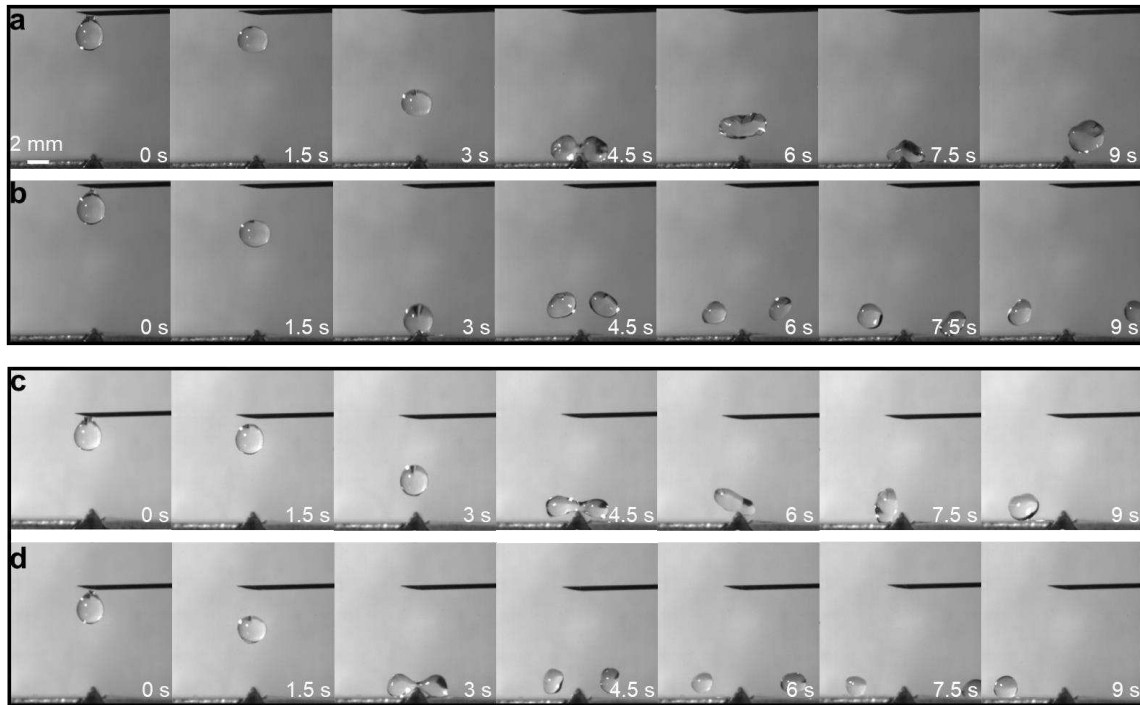
Figure 6.4. 10 μl water droplets hitting a macroscopic ridge on a superhydrophobic surface. Water droplet a) bouncing back as a single droplet after hitting the ridge with $H = 9.74$ mm, $We = 3.6$ and b) splitting into two droplets after hitting the ridge with $H_c = 9.88$ mm, $We_c = 3.7$, on the same ridge with $\alpha_r = 70°$, $h_r = 0.5$ mm. Water droplet c) bouncing back as a single droplet after hitting the ridge with $H = 5.69$ mm, $We = 2.1$ and d) splitting into two droplets after hitting the ridge with $H_c = 5.92$ mm, $We_c = 2.2$, on the same ridge with $\alpha_r = 70°$, $h_r = 1$ mm.

6.5. Droplet Splitting - Results

To further investigate the influence of ridge geometry on critical splitting height H_c, we plotted H_c as a function of ridge height h_r, for different ridge angles α_r (Figure 6.5). Our results indicate that for each ridge angle α_r, as the ridge height h_r increases the critical splitting height H_c decreases. However, this reduction turns into a plateau beyond a certain ridge height h_r. For

example, on the superhydrophobic macroscopic ridge on flat surface with $\alpha_r = 70°$, but different ridge heights $h_r = 2$ mm, $h_r = 2.5$ mm and $h_r = 3$ mm for a certain critical releasing height of $H_c = 4.3$ mm above the ridge, water droplet splits into two smaller droplets after hitting the ridge (Figures 6.6a – 6.6c). This happens because beyond a certain ridge height h_r, which is a function of the droplet volume, the two lobes of droplet do not touch the flat surfaces anymore. Therefore, the droplet interacts only with the ridge and not the flat surfaces. Consequently, beyond a certain ridge height h_r, by increasing the ridge height h_r, there is no change in critical splitting height H_c. Further, beyond ridge height of $h_r = 1$ mm for $\alpha_r = 115°$ and $\alpha_r = 90°$ and beyond ridge height of $h_r = 1.5$ mm for $\alpha_r = 70°$ and $\alpha_r = 35°$, no statistically significant difference was observed between the critical splitting height of water droplets.
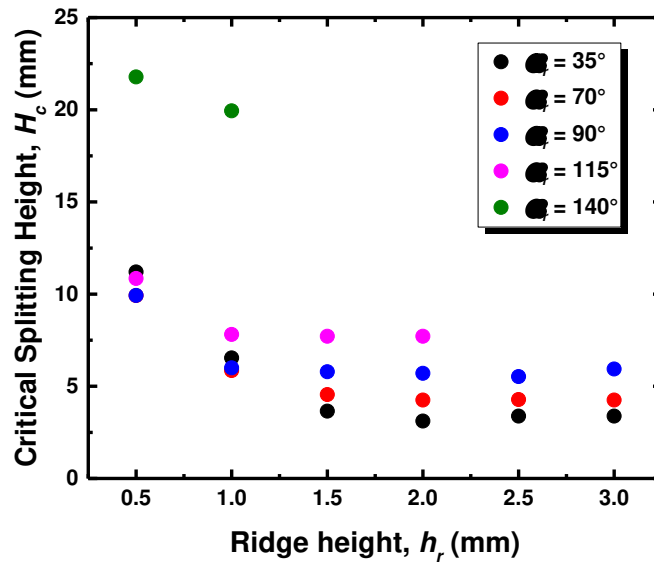
Figure 6.5. Critical splitting height H_c as a function of Ridge geometry.
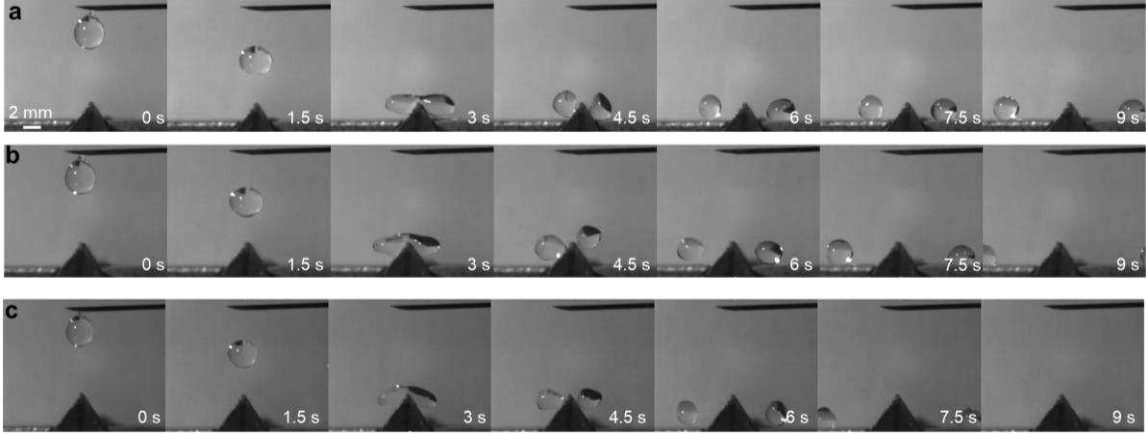
Figure 6.6. Water droplet splitting into two droplets after hitting the ridge with $H_c = 4.3$ mm, on the same ridge with $\alpha_r = 70°$ but different ridge heights a) $h_r = 2$ mm, b) $h_r = 2.5$ mm and c) $h_r = 3$ mm. As the ridge height increases, there is no change in the critical splitting height H_c because the two lobes of the droplet cannot touch the flat surfaces.
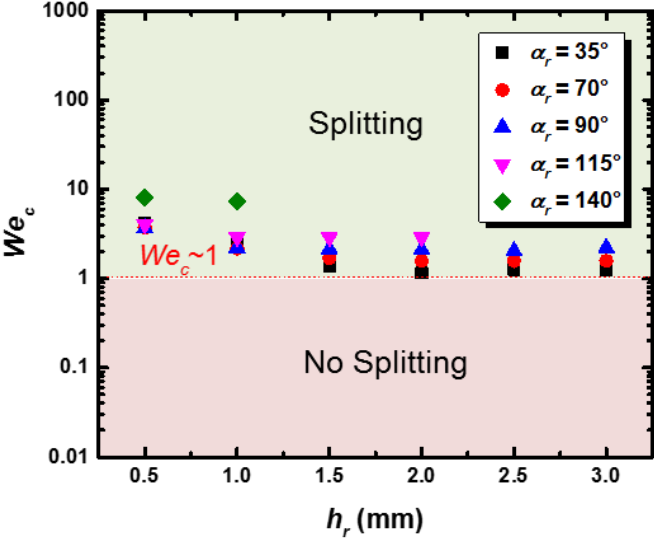
Figure 6.7. The variation of critical We_c as a function of ridge heights h_r for different ridge angles α_r.

As previously mentioned (in section 6.2), we have discussed that a droplet impacting a superhydrophobic ridge splits when the inertial forces overcome the capillary forces. In other words, the droplet splits when $We_c \sim O(1)$ (see equation 6-4). In order to verify whether our experimental results agree with this theoretical prediction, we have plotted the critical We_c as a function of ridge heights h_r for different ridge angles α_r (Figure 6.7). Our results indicate that

experimental results indeed agree with theoretical prediction of $We_c \sim O(1)$, regardless of the ridge geometry.

6.6. Conclusions

In summary, in this work, we studied the splitting of water droplets on superhydrophobic macroscopic ridge on flat surfaces. We demonstrated that for each ridge angle, as the ridge height increases the critical splitting height decreases. However, this reduction turns into a plateau beyond a certain ridge height which is a function of droplet volume, because the two lobes of droplet do not touch the flat surfaces anymore. Further, our results indicate that a water droplet impacting a superhydrophobic ridge splits when $We_c \sim O(1)$, regardless of the ridge geometry.

REFERENCES

(1) Jung, Y. C.; Bhushan, B. Dynamic effects of bouncing water droplets on superhydrophobic surfaces. *Langmuir* **2008,** *24*, 6262-6269.

(2) Deng, T.; Varanasi, K. K.; Hsu, M.; Bhate, N.; Keimel, C.; Stein, J.; Blohm, M. Nonwetting of impinging droplets on textured surfaces. *Applied Physics Letters* **2009,** *94*, 133109.

(3) Pearson, J. T.; Maynes, D.; Webb, B. W. Droplet impact dynamics for two liquids impinging on anisotropic superhydrophobic surfaces. *Experiments in fluids* **2012,** *53*, 603-618.

(4) Wang, Z.; Lopez, C.; Hirsa, A.; Koratkar, N. Impact dynamics and rebound of water droplets on superhydrophobic carbon nanotube arrays. *Applied physics letters* **2007,** *91*, 023105.

(5) Richard, D.; Clanet, C.; Quéré, D. Surface phenomena: Contact time of a bouncing drop. *Nature* **2002,** *417*, 811.

(6) Tsai, P.; Pacheco, S.; Pirat, C.; Lefferts, L.; Lohse, D. Drop impact upon micro-and nanostructured superhydrophobic surfaces. *Langmuir* **2009,** *25*, 12293-12298.

(7) Richard, D.; Quéré, D. Bouncing water drops. *EPL (Europhysics Letters)* **2000,** *50*, 769.

(8) Hyväluoma, J.; Timonen, J. Impact states and energy dissipation in bouncing and non-bouncing droplets. *Journal of Statistical Mechanics: Theory and Experiment* **2009,** *2009*, P06010.

(9) Yonemoto, Y.; Kunugi, T. Analytical consideration of liquid droplet impingement on solid surfaces. *Scientific reports* **2017,** *7*, 2362.

(10) Chen, L.; Xiao, Z.; Chan, P. C.; Lee, Y.-K.; Li, Z. A comparative study of droplet impact dynamics on a dual-scaled superhydrophobic surface and lotus leaf. *Applied surface science* **2011,** *257*, 8857-8863.

(11) Alizadeh, A.; Bahadur, V.; Zhong, S.; Shang, W.; Li, R.; Ruud, J.; Yamada, M.; Ge, L.; Dhinojwala, A.; Sohal, M. Temperature dependent droplet impact dynamics on flat and textured surfaces. *Applied physics letters* **2012,** *100*, 111601.

(12) Bartolo, D.; Bouamrirene, F.; Verneuil, E.; Buguin, A.; Silberzan, P.; Moulinet, S. Bouncing or sticky droplets: Impalement transitions on superhydrophobic micropatterned surfaces. *EPL (Europhysics Letters)* **2006,** *74*, 299.

(13) Callies, M.; Quéré, D. On water repellency. *Soft matter* **2005,** *1*, 55-61.

(14) Liu, Y.; Whyman, G.; Bormashenko, E.; Hao, C.; Wang, Z. Controlling drop bouncing using surfaces with gradient features. *Appl. Phys. Lett.* **2015,** *107*, 051604.

(15) Liu, Y.; Moevius, L.; Xu, X.; Qian, T.; Yeomans, J. M.; Wang, Z. Pancake bouncing on superhydrophobic surfaces. *Nature physics* **2014,** *10*, 515.

(16) Liu, Y.; Andrew, M.; Li, J.; Yeomans, J. M.; Wang, Z. Symmetry breaking in drop bouncing on curved surfaces. *Nature communications* **2015,** *6*, 10034.

(17) Bird, J. C.; Dhiman, R.; Kwon, H.-M.; Varanasi, K. K. Reducing the contact time of a bouncing drop. *Nature* **2013,** *503*, 385.

(18) Gauthier, A.; Symon, S.; Clanet, C.; Quéré, D. Water impacting on superhydrophobic macrotextures. *Nature communications* **2015,** *6*, 8001.

(19) Song, D.; Song, B.; Hu, H.; Du, X.; Zhou, F. Selectively splitting a droplet using superhydrophobic stripes on hydrophilic surfaces. *Physical Chemistry Chemical Physics* **2015,** *17*, 13800-13803.

(20) Yokoi, K. Numerical studies of droplet splashing on a dry surface: triggering a splash with the dynamic contact angle. *Soft Matter* **2011,** *7*, 5120-5123.

(21) Mishchenko, L.; Hatton, B.; Bahadur, V.; Taylor, J. A.; Krupenkin, T.; Aizenberg, J. Design of ice-free nanostructured surfaces based on repulsion of impacting water droplets. *ACS nano* **2010,** *4*, 7699-7707.

(22) Li, T.; Zhang, L.; Duan, Y.; Li, J.; Wang, Z.; Wang, J.; Li, H. Bouncing dynamics of liquid drops impact on ridge structure: An effective approach to reduce the contact time. *Physical Chemistry Chemical Physics* **2018**.

(23) Regulagadda, K.; Bakshi, S.; Das, S. K. Morphology of drop impact on a superhydrophobic surface with macro-structures. *Physics of Fluids* **2017,** *29*, 082104.

(24) Zou, L.; Wang, H.; Zhu, X.; Ding, Y.; Chen, R.; Liao, Q. Droplet splitting on chemically striped surface. *Colloids and Surfaces A: Physicochemical and Engineering Aspects* **2018,** *537*, 139-148.

(25) Songmene, V.; Khettabi, R.; Zaghbani, I.; Kouam, J.; Djebara, A. Machining and machinability of aluminum alloys. In *aluminium alloys, theory and applications*; InTech: 2011.

CHAPTER 7 – CONCLUSIONS AND FUTURE WORK

The tailored surface wettability, achieved by tuning the surface chemistry and surface texture, results in tunable interaction between the surface and the contacting liquid droplets. Thus far, the tailored wettability of liquid-repellent surfaces has been employed for various novel applications such as patterned surfaces for enhanced heat transfer, oil-water separation membranes, droplet manipulation and controllable adhesion and more applications yet to come. The research presented herein summarizes the fundamentals of tuning the interaction of droplets with liquid-repellent surfaces and provides some of its subsequent applications. In this chapter, the contributions of this work to fundamental science and applied science is highlighted and the potential aspects of this work for future investigation is presented.

7.1. Contributions to Fundamental and Applied Sciences

Through this research effort, the following contributions to fundamental science and applied science were made:

(i) **New methodology to sort liquid droplets based on their surface tension:**

Contributions to fundamental science: We have demonstrated that in systems with no specific solid–liquid interactions, liquids with lower surface tension adhere more to a super-repellent surface (i.e., display less mobility) and liquids with higher surface tension adhere less (i.e., display higher mobility). This is because liquids with lower surface tension spread more on the surface, which results in higher width of solid–liquid–vapor contact line and higher contact angle hysteresis.

Contributions to applied science: We fabricated a simple device with precisely tailored solid surface energy domains that, for the first time, can sort droplets by surface tension. Further, we envision that our methodology for droplet sorting will enable inexpensive and energy-efficient analytical devices for personalized point-of-care diagnostic platforms, lab-on-a-chip systems, biochemical assays and biosensors.

(ii)   New approach to detect the quality of fuel blends:

Contributions to fundamental science: We demonstrated that increasing the stiffness of the non-polar functional groups, increasing the surface roughness and decreasing the droplet volume can enhance the differences in contact angle hystereses and droplet mobilities of liquid droplets with different surface tensions on non-textured, non-polar liquid-repellent surfaces.

Contributions to applied science: We employed liquid repellent (e.g., non-textured, non-polar slippery) surfaces to fabricate a simple, field-deployable, low-cost device to rapidly detect the quality of fuel blends (e.g., diesel-kerosene blends with different compositions) by sensing their surface tension with significantly improved resolution.

(iii)   Novel materials with improved hemocompatibility:

Contributions to fundamental science: We demonstrated that only those superhemophobic surfaces with high breakthrough pressure and a robust Cassie-Baxter state have the potential to enhance hemocompatibility.

Contributions to applied science: We fabricated materials (i.e., superhemophobic titania surfaces) on which blood protein adhesion and platelet adhesion and activation decreased significantly. We envision that the understanding gained from this work will lead to the fabrication of implants and devices with improved hemocompatibility.

(iv) **Advanced understanding of droplet splitting upon impacting a macroscopic ridge:**

Contributions to fundamental science: We demonstrated that for each ridge angle, as the ridge height increases the critical splitting height decreases. However, this reduction turns into a plateau beyond a certain ridge height, which is a function of droplet volume, because the two lobes of the droplet do not touch the flat surfaces anymore. Further, our results indicate that a water droplet impacting a superhydrophobic ridge splits when $We_c \sim O(1)$, regardless of the ridge geometry.

7.2. Future Work

During this research, some notable research issues regarding tuning the interaction of droplets with liquid-repellent surfaces were uncovered, which need further investigation. The following is a list of these issues:

Manipulation of droplets to sort droplets based on surface tension:

Benign Surface Chemistry: Many studies on super-repellent surfaces have employed long chain fluorocarbon surface chemistry due its low solid surface energy. However, long chain fluorocarbon materials are rapidly being phased out by environmental agencies across the world because of the growing concerns regarding their negative environmental impacts (e.g., non bio-degradable) and biological impacts (e.g., bioaccumulation).[1-4] Consequently, future work should be focused on employing benign surface chemistries that are non-toxic and non-bioaccumulative.

Devices to Sort Droplets by Surface Tension as Diagnostic Platforms: Prior work has demonstrated that the surface tension of biological fluids (e.g., blood, plasma, urine etc.) can be altered due to certain diseases (e.g., diabetic kidney disease) or certain health condition (e.g.,

gestation period).[5-6] Consequently, future work should investigate the functionality of devices which can sort droplets by surface tension for personalized point-of-care diagnostic platforms.

Economic analysis: We anticipate that the device which can detect the fuel quality, have substantial economic impacts in developing nations. Future work should investigate the economic analysis of this product in different developing counties (e.g., India).

Hemocompatibility of super-repellent surfaces:

Mechanical Durability: Practical applications of super-repellent surfaces for medical implants and devices require mechanical durability of the texture. While the number of reports on durable super-repellent surfaces continues to increase,[7-11] mechanical durability of super-repellent surfaces, especially against shear stresses in solid abrasion, continues to be a significant challenge. Therefore, there is a significant need for improving the mechanical durability by using monolithic textures of materials with high deformability and/or self-healing ability or proceeding towards non-textured slippery surfaces where possible.

Mechanistic Studies: To obtain a mechanistic understanding of the of hemocompatibility of super-repellent surfaces, future work should investigate the influence of different solid-liquid area fractions and different surface morphologies of the super-repellent surfaces on each single event in thrombotic and immune responses need to be investigated in detail. Clearly understanding the underlying mechanisms will allow material scientists to better tune the texture and chemistry of the super-repellent surfaces for favorable interactions with blood.

Dynamic Testing: The interaction of blood with the super-repellent surfaces under hemodynamic conditions[12-15] can be significantly different from the static conditions. Since most practical materials, implants and devices experience hemodynamic conditions, future work should be

focused on evaluating the hemocompatibility under relevant dynamic conditions (e.g., blood flow rate, wall shear stress, pulsatile flow etc.) in the context of the application.[16]

In vivo Testing: The true functionality of any surface or material in contact with blood can be revealed when implanted inside body. In order to truly design and develop effective implantable medical devices, future studies should earmark more *in vivo* tests in animal models first and eventually human clinical trials.

Longevity: Practical application of super-repellent surfaces for medical implants and devices require longevity of the Cassie-Baxter state (i.e., air pockets). In order to avoid the loss of air pockets by dissolution of air into the blood or by breakthrough of blood into the texture, one strategy is to employ textures with as small of an inter-feature spacing as possible (e.g., sub-micron inter-feature spacings). In addition to offering very high breakthrough pressures, super-repellent surfaces with extremely small inter-feature spacings have the potential to offer virtually infinite lifetimes for the air pockets.[17-19] Future study should investigate the prolonged functionalities of super-repellent surfaces in contact with blood (over weeks and months).

Splitting droplets on super-repellent microscopic ridge:

Splitting Height of Low Surface Tension Liquids: While the splitting of water droplets on superhydrophobic ridges has been studied, the behavior of low surface tension liquids hitting superomniphobic ridges has not been investigated. Future study should investigate the influence of surface tension on splitting height and predicts the scaling law that agrees with the experimental data.

Influence of Viscosity on Splitting Height: For liquid droplets with high viscosity, the capillary number is not negligible anymore. Future study should investigate the influence of viscosity on

splitting height and predicts the scaling law that agrees with the experimental data. Employing water-glycerin solutions enables systematically investigation of the influence of viscosity on the critical splitting height using super-repellent surfaces.

Numerical Simulations: Future study should implement 3D numerical simulations to model the splitting of the droplets and verify the obtained experimental results.

REFERENCES

(1) Risk Management for Per- and Polyfluoroalkyl Substances (PFASs) under TSCA. *U.S. Environmental Protection Agency* **2006**.

(2) PFOA Stewardship Program Baseline Year Summary Report. *U.S. Environmental Protection Agency* **2017**.

(3) Benford, D.; Boer, d. J.; Carere, A.; Domenico, d. A.; Johansson, N.; Schrenk, D.; Schoeters, G.; Voogt, P.; Dellatte, E. Opinion of the scientific panel on contaminants in the food chain on perfluorooctane sulfonate (PFOS), perfluorooctanoic acid (PFOA) and their salts. *EFSA Journal* **2008**, 1-131.

(4) Perfluorooctane sulfonate and its salts and certain other compounds regulations. *Government of Canada* **2008**.

(5) Kazakov, V. N.; Sinyachenko, O. V.; Fainerman, V. B.; Pison, U.; Miller, R. *Dynamic surface tensiometry in medicine*, Elsevier: 2000; Vol. 8.

(6) Fathi-Azarbayjani, A.; Jouyban, A. Surface tension in human pathophysiology and its application as a medical diagnostic tool. *BioImpacts: BI* **2015,** *5*, 29.

(7) Cohen, N.; Dotan, A.; Dodiuk, H.; Kenig, S. Superhydrophobic coatings and their durability. *Materials and Manufacturing Processes* **2016,** *31*, 1143-1155.

(8) Golovin, K.; Boban, M.; Mabry, J. M.; Tuteja, A. Designing Self-Healing Superhydrophobic Surfaces with Exceptional Mechanical Durability. *ACS Applied Materials & Interfaces* **2017,** *9*, 11212-11223.

(9) Verho, T.; Bower, C.; Andrew, P.; Franssila, S.; Ikkala, O.; Ras, R. H. Mechanically durable superhydrophobic surfaces. *Advanced Materials* **2011,** *23*, 673-678.

(10) Jung, Y. C.; Bhushan, B. Mechanically durable carbon nanotube− composite hierarchical structures with superhydrophobicity, self-cleaning, and low-drag. *ACS nano* **2009,** *3*, 4155-4163.

(11) Xiu, Y.; Liu, Y.; Hess, D. W.; Wong, C. Mechanically robust superhydrophobicity on hierarchically structured Si surfaces. *Nanotechnology* **2010,** *21*, 155705.

(12) Bark, D. L.; Para, A. N.; Ku, D. N. Correlation of thrombosis growth rate to pathological wall shear rate during platelet accumulation. *Biotechnology and bioengineering* **2012,** *109*, 2642-2650.

(13) Bark Jr, D. L.; Ku, D. N. Platelet transport rates and binding kinetics at high shear over a thrombus. *Biophysical journal* **2013,** *105*, 502-511.

(14) Einav, S.; Bluestein, D. Dynamics of blood flow and platelet transport in pathological vessels. *Annals of the New York Academy of Sciences* **2004,** *1015*, 351-366.

(15) Nesbitt, W. S.; Westein, E.; Tovar-Lopez, F. J.; Tolouei, E.; Mitchell, A.; Fu, J.; Carberry, J.; Fouras, A.; Jackson, S. P. A shear gradient–dependent platelet aggregation mechanism drives thrombus formation. *Nature medicine* **2009,** *15*, 665.

(16) Fogelson, A. L.; Neeves, K. B. Fluid mechanics of blood clot formation. *Annual review of fluid mechanics* **2015,** *47*, 377-403.

(17) Jones, P. R.; Hao, X.; Cruz-Chu, E. R.; Rykaczewski, K.; Nandy, K.; Schutzius, T. M.; Varanasi, K. K.; Megaridis, C. M.; Walther, J. H.; Koumoutsakos, P. Sustaining dry surfaces under water. *Scientific reports* **2015,** *5*.

(18) Xu, M.; Sun, G.; Kim, C.-J. Infinite lifetime of underwater superhydrophobic states. *Physical review letters* **2014,** *113*, 136103.

(19) Patankar, N. A. Thermodynamics of trapping gases for underwater superhydrophobicity. *Langmuir* **2016,** *32*, 7023-7028.

APPENDIX A- MATERIALS AND METHODS

1. **Statistical Analysis:**

    1.1. For the statistical analysis, one-way analysis of variance (ANOVA) followed by Tukey's test is conducted using Minitab Software.

    1.2. In order to determine whether there is a statistically significance difference between the means, p-value was compared to the significance level to assess the null hypothesis. The null hypothesis states that the population means are all equal. Here, the significance level of 0.05 is used (5% risk of concluding that a difference exists when there is no actual difference).

    1.3. P-value $\leq \alpha$: The differences between some of the means are statistically significant. The null hypothesis is rejected, and we conclude that not all of population means are equal.

    1.4. P-value $> \alpha$: The differences between the means are not statistically significant. There is no enough evidence to reject the null hypothesis. (In this case, we need to verify the test has enough power to detect a difference that is practically significant).

    1.5. If there is no statistically significant difference, using power analysis it needs to be verified that the test has enough power.

    1.6. Note that with higher number of comparison, the likelihood that at least one of them indicates the significant differences is higher and it may increase the type 1 error rate.

    1.7. P-value $\leq \alpha$ states that some of the group means are different, but it doesn't identify the pairs of groups which are different. The grouping information table can provide further information about significant differences between specific pairs of groups.

2. Growing Titania Nanoflowers (Hydrothermal Synthesis):

2.1. First, clean titanium sheet (Titanium Joe Inc.) with dimension of 6 cm long × 2 cm wide × 0.8 mm thick using sonication in acetone for 10 min and sonication in isopropanol for 10 min.

2.2. Wash cleaned titanium sample thoroughly with water and dry it with nitrogen.

2.3. With extreme caution, make 20 mM hydrofluoric acid (47% Alfa Aesar) solution in DI water in the PTFE-lined stainless-steel autoclave.

2.4. Use stir bars to for 2 min at 200 rpm to make sure the solution is well mixed.

2.5. Place the titanium sheet in the autoclave horizontally.

2.6. Sealed the autoclave to etch the titanium sheet under hydrothermal conditions at 100 °C for different times. The autoclave should be properly sealed in order to keep the vapor inside the autoclave. Note: Instead of an autoclave, the nanoflowers can be grown using Teflon beakers placed on hot plate. In this case, the hot plate should be adjusted to 300 °C.

2.7. After the time for the experiment was over, let the autoclave to be cooled down for 30 min before opening the lid.

2.8. After that, wash the sample with water thoroughly and dry it on hot plate at 50 °C for 1 hour.

3. Vapor Phase Silanization:

3.1. Expose the cleaned surfaces to oxygen plasma (Plasma etch) for 15 minutes to form hydroxyl groups on the surfaces for silanization.

3.2. After oxygen plasma is completed, place the samples on the hot plate.

3.3. Use a glass slide which is large enough to hold 200 µL of target silane on the glass slide which is placed next to the oxidized sample.

3.4. Use glass bowl to cover the sample and silane and create a closed chamber.

3.5. Silanization takes one hour at 120 °C. After that, wash the sample with DI water and ethanol to remove any excess silane and dry the sample using nitrogen.

4. Sorting Droplet Device:

4.1. Use a 254 nm UV bench lamp (UVP XX-40S) for tuning the surface chemistry of titanium dioxide surfaces.

4.2. The UV light was covered completely with cardboard except a 2x2 cm square hole.

4.3. Place the samples approximately 2 cm away from the UV lamp.

4.4. Expose discrete domains of the titanium dioxide sample to UV irradiation for the desired time while masking the other areas with a PTFE tape.

5. Fabrication of Non-polar Slippery Surfaces with Fluorocarbon or Hydrocarbon Silanes.

5.1. For fabrication of non-textured, non-polar slippery OTS-and FDTS-treated surface, the silicon wafer/glass substrate, first sonicate the sample in ethanol-DI water (1:1, v/v) solution for 10 min and then rinsed with copious amounts of DI water to remove any impurity on the surface.

5.2. Then, place the cleaned sample in plasma chamber (Plasma etch) for 15 minutes to deposit hydroxyl groups over the surface which reacts readily with silane.

5.3. After that the place the sample in a reactive solution which was prepared at scales ranging from 10 to 50 ml in a polypropylene screw-cap tube (Falcon) for 2 hours.

5.4. For example, 15 ml of toluene (Fisher Chemical), 12 μl of hydrochloric acid (Fisher Scientific) and 16 μl of either octadecyltrichlorosilane (to fabricate OTS-treated surface; Gelest) or heptadecafluoro-1,1,2,2-tetrahydrodecyl trichlorosilane (to fabricate FDTS-treated surface; Gelest).

5.5. The sample was then dried by blowing nitrogen.

6. **Fabrication of Superomniphobic Surfaces using Spray Coating:**

6.1. Put 300 mg of fumed silica particles (diameter ~7 nm; Sigma Aldrich) in a 20 ml vial.

6.2. After that make a solution consisting of 10 mL n-Hexane (Fisher) and 0.3 mL heptadecafluoro-1,1,2,2-tetrahydrodecyl trichlorosilane (Gelest) and add it to the silica particles.

6.3. Keep the solution on a vortexer for three days to form a suspension of fluorinated silica ($F-SiO_2$) particles.

6.4. To fabricate the superhydrophobic surface, first, spin coat a glue layer (Gorilla glue) on the target surface at 5000 rpm for 120 s to make sure a very thin layer of adhesive was distributed on the ridge.

6.5. Immediately after spin coating of the adhesive layer (i.e., before adhesive layer was dried), spray coat the suspension of $F-SiO_2$ particles on the adhesive layer.

6.6. Spray coating should be done at a pressure of 30 psi using an air brush (Paasche) held 10 cm from the surface. Then, allow the surface to be dried at room temperature.